Trond Varslot

Wavefront aberration correction in medical ultrasound imaging

Doktor Ingeniør thesis

Department of Mathematical Sciences
Norwegian University of Science and Technology
Trondheim
Norway

Sammendrag

Medisinsk ultralydavbildning er et relativt rimelig verktøy som er i utstrakte bruk på dagens sykehus og tildels også legekontor.
En underliggende antakelse ved dagens avbildningsteknikker er at vevet som skal avbildes i grove trekk er homogent. Det vil i praksis si at de akustiske egenskapene varierer lite. I tilfeller der denne forutsetningen ikke holder vil resultatet bli betraktlig reduksjon av bildekvaliteten.
Prosjektet har fokusert på hvordan man best mulig kan korrigere for denne kvalitetsforringelsen. Arbeidet har resultert i et styrket teoretisk rammeverk for modellering, programvare for numerisk simulering. Rammeverket gir en felles forankring for tidligere publiserte metoder som "time-reversal mirror", "beamsum-correlation" og "speckle brightness", og gir derfor en utvidet forståelse av disse metodene. Videre har en ny metode blitt utviklet basert på egenfunksjonsanalyse av et stokastisk tilbakespredt lydfelt. Denne metoden vil potensielt kunne håndtere sterk spredning fra områder utenfor hovedaksen til ultralydstrålen på en bedre måte enn tidligere metoder.
Arbeidet er utført ved Institutt for matematiske fag, NTNU, med professor Harald Krogstad, Institutt for matematiske fag, som hovedveileder og professor Bjørn Angelsen, Institutt for sirkulasjon og bildediagnostikk, som medveileder.

Preface

This thesis is submitted in partial fulfilment of the requirements for the degree "Doktor Ingeniør" at the Norwegian University of Science and Technology (NTNU). The research was funded by the Research Council of Norway (NFR), and was carried out at the Department of Mathematical Sciences, NTNU.

I would like to use this opportunity to thank my two supervisors Professor Harald Krogstad and Professor Bjørn Angelsen. Their help and guidance has been instrumental in my progress towards this thesis work. Professor Robert Waag has also played an important role. Although he has not undertaken any formal supervision, has been my mentor at the University of Rochester (UoR).

Even with such a strong support team at NTNU and UoR, I would not have gotten this far without an understanding wife. Thank you Fionna. Not only for patiently reading through the thesis more carefully than anyone else ever will – without the prerequisite knowledge to understand most of it –, but also for taking on large parts of my responsibilities at home.

Trondheim, September 2004
Trond Varslot.

Table of Contents

Chapter 1

Introduction

As technology advances, terminology and techniques become so specialised as to make it increasingly difficult for the layperson to understand what is taking place. It is, therefore, beneficial to provide a simple, less technical explanation of the work presented in order to explain the motivation behind the research. The first chapter of this thesis is an attempt at doing so. A brief description of ultrasound imaging is provided in Sec. I. Following this, in Sec. I.A, is a discussion of wavefront aberration. This is a problem associated with most current medical ultrasound imaging applications, and is also the topic of this thesis. Some terminology is introduced and examples offered in Secs. I.B and I.C, while the introduction concludes with an outline of the presented thesis work in Sec. II.

I Ultrasound

Sound may be defined as pressure waves being propagated by local vibrations in a medium. The human ear is constructed to detect pressure waves with frequencies ranging roughly between 20 Hz and 20 kHz. The term *ultrasound* is used to denote sound with frequencies above the audible range; that is, 20 kHz.

Ultrasound is used in a wide range of applications. High-precision ink printers,[1] land mine detection,[2] and personal identification systems[3] are all areas where ultrasound is utilised. The best known application of ultrasound is still medical ultrasound imaging.[4] This is mostly due to the routine ultrasound checks which women in many countries undergo during pregnancy. Less well-known, perhaps, is the use of ultrasound imaging in other clinical situations, for example diagnosis of heart disorders and tumour detection, where it offers an attractive alternative to other diagnostic tools.

The main advantages of ultrasound imaging compared to other imaging techniques, are the absence of harmful side-effects, *e.g.* radiation damage associated with X-rays, and the fact that the equipment is relatively inexpensive compared to other alternatives such as magnetic resonance imaging (MRI).

The image resolution is fundamentally limited by the length of the applied ultrasound pulse; higher frequency means that a shorter pulse may be employed. This again implies better image resolution. However, the absorption of acoustic energy increases with frequency. Therefore, a high-frequency pulse is not able to penetrate as deep as a low-frequency pulse with the same energy. Safety regulations prohibit the use of high-energy transmit pulses in acoustic imaging systems. Thus, in order to image organs which lie deep within the human body, for example the liver, there is an upper limit to the frequency which may be applied. For medical ultrasound imaging, frequencies mostly in the range of 1-10 MHz are employed. This is the result of a trade-off between image resolution and imaging depth.

An ultrasound image is formed by transmitting a focused ultrasound pulse from a device denoted the *transducer*, through the medium to be imaged. Spatial variations in the acoustic properties of tissue (mass density and compressibility) then cause parts of the transmitted pulse to be reflected back to the transducer. These echoes, often referred to as *acoustic backscatter*, are then recorded and processed to form the image. The time between transmitting and receiving a pulse is related to the depth from which the echo emerged. This may be used to identify the location of an interface between regions with different acoustic properties.

Since the inception of ultrasound imaging in the early 1950s,[5] the range of applications for medical ultrasound imaging has expanded rapidly, and it has become a widely-used diagnostics tool in many areas of medicine. With the advent of increased processing power and new display techniques, there is the potential for ultrasound imaging to expand even further. However, there are still some fundamental problems which have not yet been resolved. One of these problems is how to efficiently filter out acoustic noise. An effective solution to this problem will improve the quality of the ultrasound images acquired, and facilitate the utility of ultrasound in new areas.

I.A Imaging and acoustic noise

At a theoretical level, the resolution of an ultrasound image is fundamentally limited by the wavelength of the transmitted pulse. However, even this limit is often not achieved in clinical applications.[6,7,8,9] This is because the transmitted pulse has to pass through tissue with large variations of acoustic properties. In combination with relatively complex structures of tissue, large variations of acoustic properties induce:

- **Reverberation:** At interfaces between materials with large differences in acoustic properties the transmitted pulse may be reflected back and forth

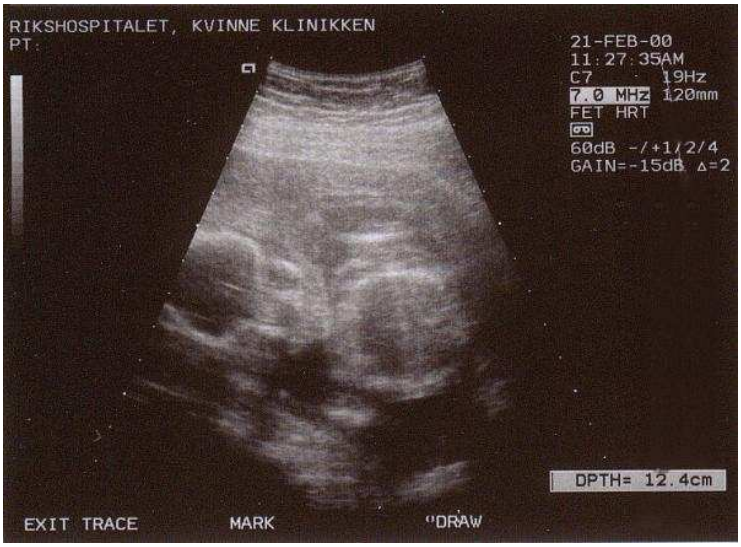

Figure 1.1: A typical ultrasound image of a baby taken at 17 weeks.

several times before it is registered at the transducer. Several reflections originating from the same interface will therefore be registered. This produces the impression of interfaces also at greater depth; so-called ghost images of the interface.

- **Wavefront aberration:** Variations of the speed of sound will cause some parts of the propagating wavefront to travel at larger velocities than others. As a result, each part of the transmitted wavefront will reach the focal point at different times. This implies a degraded focus of the transmitted beam.

The reduced focusing caused by wavefront aberration, in turn, reduces the *spatial resolution* in the ultrasound imaging system. Spatial resolution may be defined as the minimum distance between point reflectors which can be separated in the image. Reverberation and wavefront aberration introduce to the image additive noise, which in turn reduces the *contrast resolution*. This is defined as the ratio between the scattering strength of the strongest and the weakest scatterer that can be detected in the vicinity of each other.

Reverberations and wavefront aberrations are denoted *acoustic noise* because they are produced by the transmitted ultrasound pulse itself. Increasing the power of the transmitted pulse will not improve the signal-to-noise ratio (SNR). The challenge is thus to reduce the image-degrading effect of pulse reverberations and wavefront aberrations in applications of ultrasound imaging.

This thesis presents a theoretical framework in which wavefront aberration may be described, and methods by which wavefront aberration may be estimated and corrected. The aim is to improve ultrasound imaging by reducing the impact of wavefront aberration. The work is conducted in the setting of ultrasound imaging, where aberrations are introduced in a layer close to the transducer; the *body wall*. This is a situation found in many applications in medicine. However, the methodology and results may have applications in other similar situations, *e.g.* sonar and seismic imaging.

I.B Characterising wavefront aberration

Consider the idealised situation where the transmitted ultrasound pulse is scattered by a single point reflector located in the focal point of the transmit-beam. In a medium where the acoustic properties are constant, a so-called *homogeneous medium*, the echo is a spherical wave propagating outwards. The curvature and amplitude of this wave may be determined from pure geometric considerations based on the speed of sound and the depth from which the echo emerged. It is therefore possible to remove the curvature and amplitude variations from the recorded signal. The result is a signal which is identical at each receiving element on the transducer. Adding the signals measured at N different receiving elements will result in a single signal which is amplified by a factor of N relative to the element signals. The process of removing the geometric curvature and adding the signals received on each location on the transducer is denoted *beam-forming*, and is an essential part of ultrasound imaging. The sum signal is here referred to as the *beamformer output*. The envelope of the beamformer output is used to represent the reflection strength of the medium in the corresponding image point.

As only echoes from the focal point will be identical at all locations on the transducer, this is the only echo which is amplified by a factor of N. Furthermore, electronic noise will be Gaussian, uncorrelated for measurements at different transducer elements. Therefore, the SNR will be increased by a factor of $\sqrt{N}$ for this type of noise.

When trying to determine the reflection strength at a particular image point, backscatter from other locations in the medium is considered noise. This noise is highly correlated between the elements, and thus amplified in the beam-forming process. Beam-forming will therefore not increase the SNR for this type of noise by a factor of $\sqrt{N}$. However, the amplification is not as strong as for the reflection from the focal point. This noise is therefore also suppressed relative to the signal from the focal point.

By transmitting beams in different directions, and processing them by removing the curvature according to various depths, the reflection intensities are obtained from each point in the image.

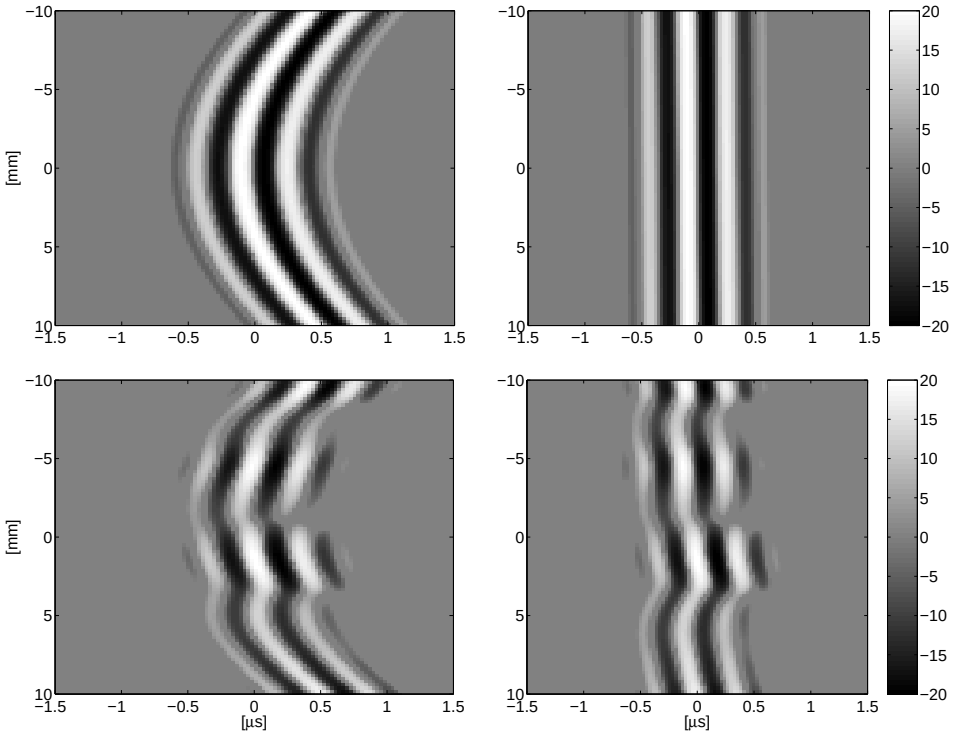

Figure 1.2: Simulated acoustic backscatter from a point reflector. Top left: measured signal without aberration. Top right: signal without aberration after the geometric curvature has been removed. Bottom left: measured signal in the presence of phase aberration. Bottom right: signal with aberration after the geometric curvature has been removed. A ±20 dB grey scale is used in the display.

Now, consider the situation where the acoustic properties of the medium are spatially variable; a so-called *heterogeneous medium*. Even after removing the geometric curvature, the signal from the focal point is not the same at each location on the transducer; the echo has undergone wavefront aberration. Therefore, the beam-forming will not amplify the echo from the focal point to the same degree. The suppression of echoes from other locations is thus not as efficient. In addition, wavefront aberration of the transmitted beam produces a larger insonified area from which echoes may emerge. Thus, the problem of echoes from outside the focal position is increased, while the ability to suppress these echoes is reduced. This results in the aforementioned reduced contrast resolution.

A simulated echo from a single point reflector is shown in Fig. 1.2. In the ideal

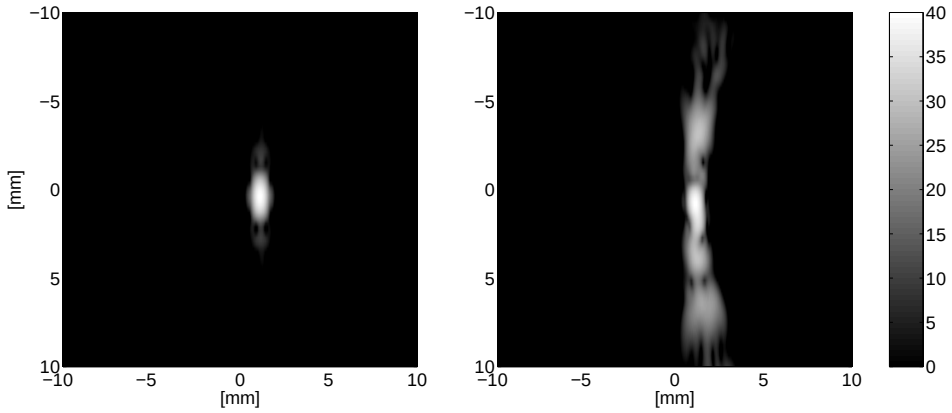

Figure 1.3: Simulated ultrasound image of a point reflector. Left: imaging without aberration. Right: imaging in the presence of phase aberration. The images are displayed using a grey scale with 40 dB dynamic range.

case, the wavefront is that of a spherical wave. The effect of aberration is clearly demonstrated by the jaggered wavefront. In addition, the amplitude of the wavefront is variable in the aberrated case, instead of a constant amplitude generated in an ideal situation. Simulated ultrasound images of a point reflector in both the ideal situation and the aberrated situation are shown in Fig. 1.3. It is not easy to see that the two images are, in fact, trying to capture the same object.

The width of the transmit-beam impacts on the size of the region from which the measured echo is generated. The *beam profile* is therefore of interest as a means of analysing the aberration. The beam profile is calculated as the root-mean-square (RMS) value of the transmitted pulse in a given plane parallel to the transducer surface; the *focal plane*. It is customary to plot the beam profile on a decibel (dB) scale, normalised to 0 dB at the peak value.

Figure 1.4 shows the transmit-beam profile for the unaberrated and aberrated situation from Figs. 1.2 and 1.3. It is not difficult to see how the resulting image must be severely degraded when the effect of the aberration has such an impact on the width of the transmitted beam. Additional simulated ultrasound images with the same aberration are displayed in Fig. 1.5.

I.C Aberration correction

There are currently no wavefront aberration correction solutions commercially available. Major obstacles have been related both to hardware and a limited understanding of the wavefront aberration process.

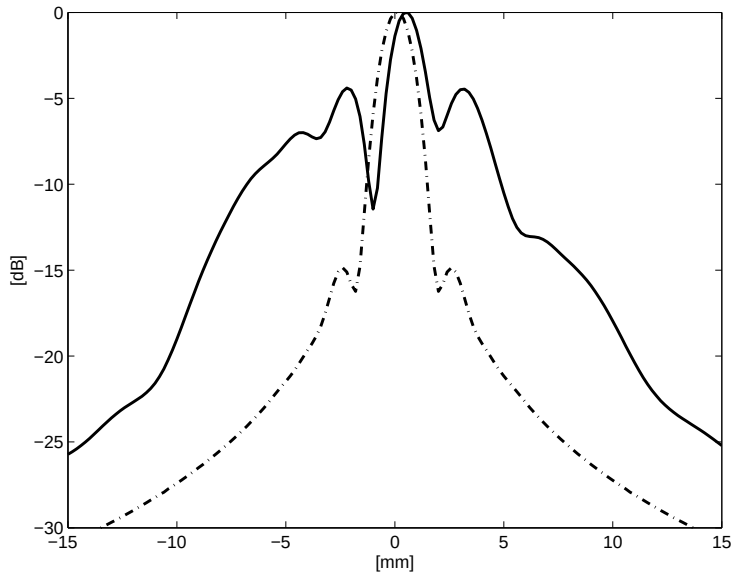

Figure 1.4: Beam profiles in the focal plane of the transmitted pulse. Dash-dot: unaberrated transmit-beam. Solid: aberrated transmit-beam.

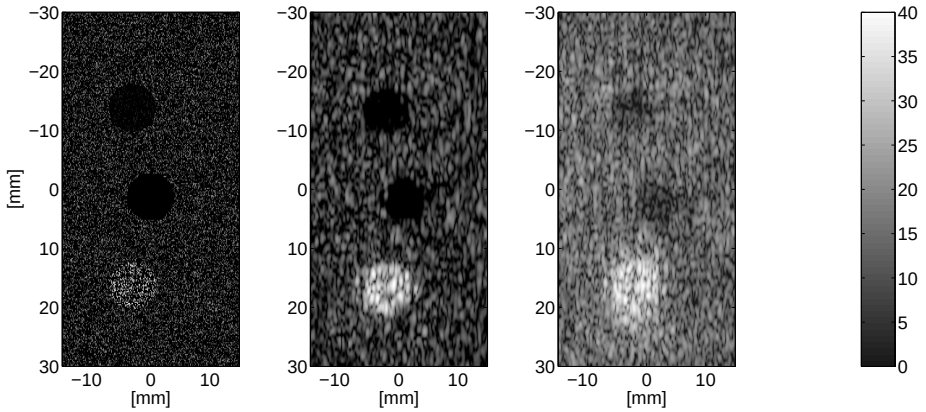

Figure 1.5: Simulated ultrasound image. Left: scattering region containing one sphere with high-intensity scatterers, one sphere with low-intensity scatterers and one sphere without scatterers. Middle: simulated image of the scattering region without aberration. Right: simulated image of the scattering region with aberration.

In the literature, the term *wavefront aberration* is often substituted by *phase aberration* or *phase and amplitude aberration*, or simply *aberration*. The term *phase aberration* usually refers to a pure time-delay of the wavefront, although a different delay for each frequency could be allowed, thus accounting for some pulse shape deformation. However, amplitude fluctuations in general are not allowed. The term *phase and amplitude aberration* signifies the option of additional amplitude fluctuations, and is thus synonymous with wavefront aberration. For the sake of simplicity, the term *aberration* is usually preferred here.

Early contributions to aberration correction in ultrasonic imaging include works by O'Donnell and Flax who applied time-delays to the transmitted and received signals in order to improve image quality.[10,11] Much work has followed their lead, generalising this to a time-delay and amplitude correction. However, most of the work has studied unrealistically simple aberrations, as pointed out by Mast *et al.*[12]

An alternative approach to time-delay filtering was proposed by Fink.[13] The basic idea is that the linear wave equation is invariant under the transformation which reverses time. Taking the echo from a known point reflector or a point source, and retransmitting a time-reversed version of this, will produce a propagating signal which focuses at the point location. An important limitation of this method is that known point reflectors are rare in a clinical situation. The use of artificially-inserted point targets or microcalcifications in human tissue as point reflectors has been suggested.

Research at NTNU has created a theoretical framework for aberration correction.[14] The framework unifies the two approaches in the sense that it is consistent with the time-reversal for a point reflector, and has the time-delay and amplitude screen as a first-order approximation. The research indicates that time-delay and amplitude filters produce close-to-ideal aberration correction, also in the case of severe aberration, even if a simple time-delay and amplitude screen does not accurately model the complexity of the aberration itself.

II Summary of the presented work

The main body of the thesis is composed of a collection of articles, either published or submitted for publication. As such, each chapter contains a summary and introduction with the appropriate references to previous works. It is for this reason that only a brief description is offered here, rather than a more comprehensive review of the research.

Minor alterations have been made to the published articles in order to make the chapters more uniform in appearance and easier to read. No changes have been made to the content.

A description of the basic problem, as well as the underlying models and notation, is repeated in several of the chapters. This means that the chapters may be read

independently of each other, although the order of the chapters suggests a logical progression in the understanding of wavefront aberration correction.

There are two main parts to this work. The first two chapters deal with modelling and simulation of sound propagation. Chapters 4 to 7 contain material on modelling of aberration, and aberration correction.

Ch 2: Sound propagation in soft tissue

T. Varslot
Private note.

In order to perform effective aberration correction it is important to understand how the aberration in produced. One step in this direction is to formulate a mathematical model which describes sound propagation in the body. In this chapter a nonlinear wave equation governing the propagation of sound through soft tissue is developed. The discussion is brief, but includes appropriate references for further study of nonlinear acoustics in general, and ultrasound in particular. It is not essential for the rest of the thesis work, but included for the sake of completeness.

Ch 3: Computer simulation of forward wave propagation in soft tissue

T. Varslot, G. Taraldsen
Submitted for publication in *IEEE Trans. Ultrason. Ferroelectr. Freq. Control.*
Short version was presented as "Computer simulation of forward wave propagation in non-linear, heterogeneous, absorbing tissue," in *Proc. 2001 IEEE-UFFC Ultrasonics Symposium*, 2001, pp. 1193–1196.

Computer simulations are well suited to the study of phase aberration in a controlled environment. A method for performing such simulations in tissue is presented in this chapter. By a parabolic approximation, a "one-way" wave equation is obtained. This approximation is justified because of the directive nature of the propagating wave forms. The numerical solution method is based on operator splitting, and is one of the standard approaches for the study of nonlinear ultrasonic effects in homogeneous tissue. The presented implementation deviates from previously presented solutions in ultrasonics in that it is valid for heterogeneous medium, *i.e.* tissue with spatially-variable characteristics such as mass-density, compressibility, nonlinearity and absorption. As such, it closely resembles that which is used in geophysical and oceanographic applications. A solution based on parabolic approximations does not, for obvious reasons, preserve reverberations of the ultrasonic pulse. This type of solution is thus well suited for isolating the effects of aberration; reverberation noise is effectively removed from the solution.

Ch 4: Spectral estimation for characterisation of acoustic aberration

T. Varslot, B. Angelsen, R. Waag
"Spectral estimation for characterization of acoustic aberration,"
J. Acoust. Soc. Am., vol. 116, no. 1, pp. 97–108, July 2004.

In situations where the region which is to be imaged is filled with point-like scatterers which are randomly distributed in space, the received echo will be a stochastic process. In order to perform aberration correction, the correct parameters need to be extracted from this stochastic process. If the number of scatterers is large, a reasonable assumption is that the echo resembles a Gaussian process. In this case, all information is resident in the mean value and the correlation function, or equivalently in the cross-spectrum. The estimation of the cross-spectrum is therefore important. This chapter deals with estimation of the cross-spectrum when the scatterers are "δ-correlated". In practise this is realised when the correlation length is much shorter than the wavelength of the transmitted pulse. Measurements obtained using a two-dimensional transducer array were used as input data for the cross-spectrum estimation. An aberration correction filter is then recovered from the spectrum. In particular, a method for utilising smooth frequency-dependence of the aberration is also proposed.

Ch 5: Eigenfunction analysis of acoustic aberration correction

T. Varslot, E. Mo, B. Angelsen, H. Krogstad
"Eigenfunction analysis of stochastic backscatter for characterization of acoustic aberration in medical ultrasound imaging,"
J. Acoust. Soc. Am., vol. 115, no. 6, pp. 3068–3076, June 2004.

An intuitive approach for correcting aberration in scattering from a point source is to align the signal received on each transducer element such that the energy of the beamformer output is maximised. In this chapter it is shown that a similar approach also is reasonable for scattering from stochastic scatterers. This leads to the construction of an aberration correction filter. The correction filter is shown to focus the energy of the aberration-corrected transmit-beam onto areas of high insonification intensity of the aberrated transmit-beam. As such, the corrected focus depends on the initial aberration. This filter is optimal in the sense of maximising the *speckle brightness*[15] in the image, and extends the work of Prada *et al.*[16] to stochastic scattering.

Ch 6: An approximate maximum likelihood estimator

T. Varslot, S.-E. Måsøy
Private note.

A natural approach to estimation for obtaining wavefront aberration correction parameters is to develop a maximum likelihood estimator (MLE). If the *generalised frequency-dependent screen* is used to model the aberration, a particular structure to the cross-power spectrum matrix is implied. Combining this structure with *a priori* knowledge of the unaberrated acoustic backscatter signal, an MLE may be found following classical theory due to Burg *et al.*[17] Of interest is the general form for a whole family of weighted average estimates as approximations to the MLE.

Ch 7: Iteration of transmit-beam aberration correction

T. Varslot and S.-E Måsøy, B. Angelsen
"Iteration of transmit-beam aberration correction in medical ultrasound imaging,"
J. Acoust. Soc. Am., 117(1), 2005. (Accepted for publication.)

The fact that the transmit-beam is aberrated impacts on the ability to determine the aberration. Severe aberration of the transmit-beam may therefore degrade the estimated correction sufficiently to limit its utility in image improvement. However, if some correction may be obtained, then the corrected transmit-beam will facilitate better estimation of the correction filter. This suggests an iterative approach to aberration correction. In this chapter two different estimation techniques[18,19] are employed to estimate aberration correction filters from simulated ultrasound scattering. The transmitted signal is iteratively improved until almost ideal aberration correction is obtained for both methods. Measures which quantify the aberration are shown to be good indicators for when the iterative correction has converged.

References

[1] H. P. Le, "Progress and trends in ink-jet printing technology," *J. Imaging Sci. Tech.*, vol. 42, no. 1, 1998.

[2] D. Donskoy, A. Ekimov, N. Sedunov, and M. Tsionskiy, "Nonlinear seismo-acoustic land mine detection and discrimination," *J. Acoust. Soc. Am.*, vol. 111, no. 6, pp. 2705–2714, 2002.

[3] J. K. Schneider and S. M. Gojevic, "Ultrasonic imaging systems for personal identification," in *Proc. 2001 IEEE-UFFC Ultrasonics Symposium*, 2001, pp. 595–601.

[4] S. L. Hagen-Ansert, *Textbook of Diagnostic Ultrasonography*, 5th ed. St. Louis: C. V. Mosby, 2000.

[5] D. H. Howry and W. R. Bliss, "Ultrasonic visualisation of soft tissue structures of the body," *J. Lab. Clin. Med.*, vol. 40, p. 579, 1952.

[6] U. Haberkorn, G. Layer, V. Rudat, I. Zuna, A. Lorenz, and G. van Kaick, "Ultrasound image properties influenced by abdominal wall thickness and composition," *J. Clin. Ultrasound*, vol. 21, pp. 423–429, 1993.

[7] L. Hinkelman, T. D. Mast, L. Metlay, and R. C. Waag, "The effect of abdominal wall morphology on ultrasonic pulse distortion. part I. measurements," *J. Acoust. Soc. Am.*, vol. 104, no. 6, pp. 3635–3649, December 1998.

[8] L. Hinkelman, D.-L. Liu, L. A. Metlay, and R. C. Waag, "Measurements of ultrasonic pulse arrival time and energy level variations produced by propagation through abdominal wall," *J. Acoust. Soc. Am.*, vol. 95, no. 1, pp. 530–541, January 1994.

[9] G. E. Trahey, P. D. Freiburger, L. F. Nock, and D. C. Sullivan, "In-vivo measurements of ultrasonic beam distortion in the breast," *Ultrason. Imaging*, vol. 13, no. 1, pp. 71–90, 1991.

[10] S. W. Flax and M. O'Donnell, "Phase-aberration correction using signals from point reflectors and diffuce scatterers: Basic prinsiples," *IEEE Trans. Ultrason. Ferroelectr. Freq. Control*, vol. 35, no. 6, pp. 758–767, 1988.

[11] M. O'Donnell and S. W. Flax, "Phase-aberration correction using signals from point reflectors and diffuce scatterers: Measurements," *IEEE Trans. Ultrason. Ferroelectr. Freq. Control*, vol. 35, no. 6, pp. 768–774, 1988.

[12] T. D. Mast, L. Hinkelman, M. O, V. Sparrow, and R. C. Waag, "Simulation of ultrasonic pulse propagation through the abdominal wall," *J. Acoust. Soc. Am.*, vol. 102, no. 2, pp. 1177–1190, August 1997.

[13] M. Fink, "Time reversal of ultrasonic fields - part I: Basic prinsiples," *IEEE Trans. Ultrason. Ferroelectr. Freq. Control*, vol. 39, pp. 555–567, 1992.

[14] S. E. Måsøy, T. F. Johansen, and B. Angelsen, "Correction of ultrasonic wave aberration with a time delay and amplitude filter," *J. Acoust. Soc. Am.*, vol. 113, no. 4, pp. 2009–2020, April 2003.

[15] D. Zhao and G. E. Trahey, "A statistical analysis of phase aberration correction using image quality factors in coherent imaging systems," *IEEE Trans. Med. Imaging*, vol. 11, no. 3, pp. 446–452, 1992.

[16] C. Prada, J. L. Thomas, and M. Fink, "The iterative time reversal process: analysis of convergence," *J. Acoust. Soc. Am.*, vol. 97, no. 1, pp. 62–71, January 1995.

[17] J. P. Burg, D. Luenberger, and D. L. Wenger, "Estimation of structured covarianve matrices," *IEEE Proc.*, vol. 70, no. 9, pp. 963–974, 1982.

[18] S.-E. Måsøy, T. Varslot, and B. Angelsen, "Estimation of ultrasonic wave aberration with signals from random scatterers," *J. Acoust. Soc. Am.*, vol. 115, no. 6, pp. 2998–3009, June 2004.

[19] T. Varslot, E. Mo, H. Krogstad, and B. Angelsen, "Eigenfunction analysis of stochastic backscatter for characterization of acoustic aberration in medical ultrasound imaging," *J. Acoust. Soc. Am.*, vol. 115, no. 6, pp. 3068–3076, June 2004.

Chapter 2

Sound propagation in soft tissue

T. Varslot
Dept. Mathematical Sciences, NTNU

Ultrasound imaging is based on the transmission of sound through a medium. It is therefore of importance to be able to model sound propagation properly. A thorough understanding of the physical processes in play provides insight into which parts of the imaging process need to be improved in order to achieve better images. In this chapter, a wave equation is derived which describes the propagation of sound through soft tissue. To this end Lagrangian coordinates are used. The two major assumptions are that shear forces are negligible in comparison to acoustic pressure forces, and that the curvature of the wavefront is small compared to the wavelength. The model has been derived previously by others, [1,2] but is included here in order to provide a more complete picture. For a more comprehensive treatment of nonlinear acoustics, the reader should consult general textbooks [3,4,5] or ultrasound-specific textbooks. [1,6]

I Lagrangian coordinates

Let r be the equilibrium position in space of a point-particle, and r_{E} the position of that same particle at time t. Define a function $\Psi(r,t)$ as

$$r_{\mathrm{E}}(r,t) = r + \Psi(r,t). \tag{2.1}$$

This function describes the movement in space of the point-particle. A point-particle is referred to as a *material point*, and r is the *Lagrange coordinate* or *material coordinate* of the material point. The function Ψ thus relates the Lagrange coordinate to the *Euler coordinate* r_{E}. For the deformations considered here, the function Ψ is invertible and differentiable with respect to both t and r.

The velocity of the material point is now naturally defined as

$$v(r,t) = \frac{\partial r_{\mathrm{E}}(r,t)}{\partial t} = \frac{\partial \Psi(r,t)}{\partial t}. \tag{2.2}$$

Equation (2.1) specifies a transformation from Euler coordinates to Lagrangian coordinates. Associated with this coordinate transformation is the *deformation gradient tensor*

$$F = I + \frac{\partial \Psi}{\partial r} = \begin{pmatrix} 1+\frac{\partial \Psi_1}{\partial r_1} & \frac{\partial \Psi_1}{\partial r_2} & \frac{\partial \Psi_1}{\partial r_3} \\ \frac{\partial \Psi_2}{\partial r_1} & 1+\frac{\partial \Psi_2}{\partial r_2} & \frac{\partial \Psi_2}{\partial r_3} \\ \frac{\partial \Psi_3}{\partial r_1} & \frac{\partial \Psi_3}{\partial r_2} & 1+\frac{\partial \Psi_3}{\partial r_3} \end{pmatrix}$$

and the Jacobian of the transformation

$$|F| \equiv \det F.$$

The *acoustic Mach number M* is defined as

$$M = \frac{1}{c}\left|\frac{\partial \Psi}{\partial t}\right|.$$

It may be shown[6] (pp. 12.9) that in an imaging situation, $M < 10^{-3}$. Furthermore, since $|\nabla \cdot \Psi| \sim M$, a good approximation for $|F|$ is

$$|F| \approx 1 + \nabla \cdot \Psi. \tag{2.3}$$

II Conservation of mass

Of interest here is the situation where particle movement is confined to small vibrations about the equilibrium position as a result of stretching and compression. The mass density, ρ, will consequently be time-dependent. However, conservation of mass may be used to obtain a simple expression for this time-dependence. Let V_0 be a region in space. Let $V(t)$ be a region in space such that

$$[r \in V_0] \Leftrightarrow [r + \Psi(r,t) \in V(t)].$$

In this case, V_0 is denoted a *control volume*, and $V(t)$ a *material region*. Let the mass density at equilibrium be $\rho_0(r)$. Since the same particles are contained in V_0 and $V(t)$, conservation of mass implies that

$$\int_{V_0} \rho_0(r)\mathrm{d}r = \int_{V(t)} \rho(r_{\mathrm{E}},t)\mathrm{d}r_{\mathrm{E}} = \int_{V_0} \rho(r,t)|F|\mathrm{d}r.$$

Therefore, the following relation holds almost everywhere:

$$\rho_0(r) = \rho(r,t)|F|.$$

If $\rho_0(r)$ is not permitted to be discontinuous, the relation holds everywhere. For practical purposes, this is assumed to be the case.

III Conservation of momentum

A natural assumption is that all external ambient forces cancel each other out in the equilibrium state. Furthermore, shear forces give rise to shear waves that travel at only 1/10 of the speed of pressure waves in soft tissue. These are therefore negligible, and only the acoustic pressure contributes as a net force acting on the medium. If p is the acoustic pressure and ∇_{E} denotes the gradient with respect to Euler coordinate r_{E}, then the acoustic pressure forces in Lagrangian coordinates are given by a change of variables

$$-\int_{V_t} \nabla_{\mathrm{E}} p \mathrm{d}r_{\mathrm{E}} = -\int_{V_0} \left(F^{-1}\right)^T \nabla p |F| \mathrm{d}r. \tag{2.4}$$

Using Eq. (2.2), the momentum for a given control volume V_0 is

$$\mathrm{p}\,(V_0) = \int_{V_0} \rho \frac{\partial \Psi}{\partial t} |F| \mathrm{d}r = \int_{V_0} \rho_0 \frac{\partial \Psi}{\partial t} \mathrm{d}r.$$

Combining this with Eq. (2.4), conservation of momentum implies that

$$\int_{V_0} \rho_0 \frac{\partial^2 \Psi}{\partial t^2} \mathrm{d}r = -\int_{V_0} \left(F^{-1}\right)^T \nabla p |F| \mathrm{d}r.$$

Since this holds for all control volumes V_0, the following must also hold:

$$\rho_0 \frac{\partial^2 \Psi}{\partial t^2} = -|F| \left(F^{-1}\right)^T \nabla p. \tag{2.5}$$

IV Nonlinear elasticity

Conservation of momentum provides three equations, Eqns. (2.5). However, there are four unknown quantities: p, Ψ_1, Ψ_2, and Ψ_3. Thus another equation is needed for the problem to be *well-posed*. The fourth equation will in this instance be specified as a relation between the pressure and the density.

The sound propagates nonlinearly through soft tissue. Indeed, the nonlinearity of sound propagation is utilised explicitly in some ultrasonic imaging modes; *harmonic imaging*.[7] A good model should therefore encompass this effect. The nonlinearity of propagation is factored into the equation through a nonlinear relationship between the pressure and the mass-density. A second-order Taylor expansion of the pressure-density relation is commonly used,

$$p(\rho) = A\left(\frac{\rho - \rho_0}{\rho_0}\right) + \frac{B}{2}\left(\frac{\rho - \rho_0}{\rho_0}\right)^2.$$

Note that this expansion is performed for constant entropy, that is, no effects related to temperature changes or viscosity are taken into account. Conservation of mass is now used to remove the density in favour of $|F|$

$$p(F) = A\left(\frac{1-|F|}{|F|}\right) + \frac{B}{2}\left(\frac{1-|F|}{|F|}\right)^2. \tag{2.6}$$

Solving for $1-|F|$ and retaining terms up to p^2 yields

$$1-|F| = \kappa p - \beta_n(\kappa p)^2,$$

where $\kappa = 1/A$ is the *compressibility* at constant temperature and $\beta_n = 1 + B/2A$ is the *coefficient of nonlinearity*.[3] Attenuation caused by heat conduction and viscosity is modelled by adding a term to the equation

$$1-|F| = \kappa p - \beta_n(\kappa p)^2 - \nu\kappa^2\frac{\partial p}{\partial t}. \tag{2.7}$$

The parameter ν is the *thermo viscosity*. This is a good model for acoustic propagation in water and air. However, it does not account for the relaxation processes that take place when compressing soft tissue. The result is that the frequency-dependence of the attenuation is inaccurately modelled. A more general attenuation term, represented by a linear operator $\mathscr{L}$, is therefore needed

$$1-|F| = \kappa p - \beta_n(\kappa p)^2 - \kappa\mathscr{L}p. \tag{2.8}$$

If the approximation in Eq. (2.3) is applied, the resulting equation is a nonlinear elasticity relation

$$-\nabla\cdot\Psi = \kappa p - \beta_n(\kappa p)^2 - \kappa\mathscr{L}p. \tag{2.9}$$

Equation (2.9) is derived from thermodynamical considerations by Angelsen[1] (Sec. 4.5), where it is shown that the attenuation may be modelled using a temporal convolution

$$\mathscr{L}p = h_\infty \underset{t}{*} p,$$

where h_∞ is a suitable function. The shape of this function depends on the medium.

V A second-order wave equation

For any reasonable spatial variation of the tissue characteristics ρ_0, κ, β_n and $\mathscr{L}$, Eqns. (2.5) and (2.8), combined with the appropriate initial conditions, determine the temporal evolution of the pressure, p, and displacement, Ψ. As such, the model is complete. However, in a simplified situation, a single scalar wave equation for the pressure is also attainable.

For plane waves the simplification $-|F|\left(F^{-1}\right)^T \nabla p = \nabla p$ is possible. This is also a good approximation when the radius of curvature of the wave front is large compared to the displacement, as is often the case in medical ultrasound imaging. [6] Combined with the approximation from Eq. (2.3), the following model is derived:

$$\begin{aligned} \frac{\partial^2 \Psi}{\partial t^2} &= -\frac{1}{\rho_0}\nabla p, \\ -\nabla \cdot \Psi &= \kappa p - \beta_n (\kappa p)^2 - \kappa \mathscr{L} p. \end{aligned}$$

Applying the divergence operator of the first equation, differentiating the second equation twice with respect to time, and adding the resulting equations, yields a scalar wave equation for the acoustic pressure

$$\nabla \cdot \left(\frac{1}{\rho_0}\nabla p\right) \frac{\partial^2 \kappa p}{\partial t^2} = -\frac{\partial^2}{\partial t^2}\left(\beta_n (\kappa p)^2 + \kappa \mathscr{L} p\right). \tag{2.10}$$

If the medium is homogeneous, *i.e.*, the parameters are independent of the spatial variable, then

$$\nabla^2 p - \frac{1}{c^2}\frac{\partial^2 p}{\partial t^2} = -\frac{\partial^2}{\partial t^2}\left(\frac{\beta_n \kappa}{c^2} p^2 + \frac{1}{c^2}\mathscr{L} p\right)$$

where $1/c^2 = \rho_0 \kappa$.

It is also possible to eliminate the pressure and obtain a wave equation for the displacement. Combining Eqns. (2.5) and (2.6), and applying the same approximations, results in the following wave equation:

$$\rho_0 \frac{\partial^2 \Psi}{\partial t^2} = \nabla\left(\frac{\nabla \cdot \Psi - \beta_n (\nabla \cdot \Psi)^2}{\kappa}\right).$$

Provided that curl$\Psi = 0$, then $\nabla(\nabla \cdot \Psi) = \nabla^2 \Psi$. In a homogeneous medium the equation is therefore simplified as

$$\nabla^2 \Psi - \frac{1}{c^2}\frac{\partial^2 \Psi}{\partial t^2} = 2\beta_n (\nabla \cdot \Psi)\left(\nabla^2 \Psi\right).$$

Attenuation may be added in a similar fashion as previously, but this is not pursued here.

References

[1] B. A. Angelsen, *Ultrasound imaging. Waves, signals and signal processing*. Trondheim, Norway: Emantec, 2000, vol. 1, http://www.ultrasoundbook.com.

[2] G. Taraldsen, "Derivation of a generalized Westervelt equation for nonlinear medical ultrasound," *J. Acoust. Soc. Am.*, vol. 109, no. 4, pp. 1329–1333, April 2001.

[3] M. F. Hamilton and D. T. Blackstock, *Nonlinear Acoustics*. San Diego: Academic Press, 1997.

[4] K. Naugolnykh and L. Ostorovsky, *Nonlinear Wave Processes in Acoustics*. New York: Cambridge University Press, 1998.

[5] J. Engelbrecht, *Nonlinear Wave Dynamics*. Dordrecht, The Netherlands: Kluwer Academic Press, 1997.

[6] B. A. Angelsen, *Ultrasound imaging. Waves, signals and signal processing*. Trondheim, Norway: Emantec, 2000, vol. 2, http://www.ultrasoundbook.com.

[7] P. T. Christopher, "Finite amplitude distortion-based inhomogeneous pulse echo ultrasound imaging," *IEEE Trans. Ultrason. Ferroelectr. Freq. Control*, vol. 44, no. 1, pp. 125–139, January 1997.

Chapter 3

Computer simulation of forward wave propagation in soft tissue

T. Varslot*, G. Taraldsen†
*) Dept. Mathematical Sciences, NTNU
†) Acoustic Research Center, Dept. Electronics and Telecommunications, NTNU

A method for simulating forward wavefront propagation in heterogeneous tissue is discussed. The intended application of this method is for the study of aberration produced when performing ultrasound imaging through a layer of soft tissue. A one-way wave equation which permits smooth variation in all acoustically-important variables is derived. This equation also describes tissue exhibiting nonlinear elasticity and arbitrary frequency-dependent relaxation. A numerical solution to this equation is found by means of operator splitting and propagation along the spatial depth coordinate. The numerical solution is accurate when compared to analytical solutions for special cases, and when compared to numerical solutions of the full wave equation by other methods.

I Introduction

The quality of an ultrasound image is limited by the distortions of the signal transmitted through the body. Ideally the ultrasonic pulse would pass undistorted through the body until it reaches the organ to be imaged. The beam should be reflected by this organ, and then pass undistorted back through the body to the transducer. Unfortunately this is not possible.

The signal received at the transducer is distorted by multiple reflections, as well as arrival time and amplitude fluctuations caused by variable tissue parameters. The former is known as *reverberation*, and the latter *phase and amplitude aberration*. The

resolution of an ultrasound image is limited by these factors. Experimental studies of abdominal wall[1,2] and breast tissue[3,4,5] as well as simulations[6,7] indicate that this aberration can significantly reduce the image resolution. In an effort to gain greater insight into the mechanisms which dominate phase and amplitude aberrations, a simulation model has been developed.

Simulation of ultrasound wave propagation has been performed by several authors previously.[6,7,8,9,10,11] These range from solving a full wave equation in a heterogeneous medium, to solving an approximate wave equation in a homogeneous medium. The aim for the model presented here is to perform simulations of the forward wave propagation in a heterogeneous medium in order to study aberrations.

There are several wave equations available for modelling acoustic wave propagation.[12,13,14] The wave equations are most conveniently solved by propagation in time. By this approach, the numerical solution to the wave equation describes both aberration and reverberation.[6,8,11] However, when propagating over large distances, such a method is expensive, both in terms of memory and computational costs. Related to the computational cost is the accumulation of numerical error which also limits this direct approach.

For directional sound beams a *parabolic approximation* ("the 15° approximation") of the wave equation is often used,[15] resulting in a one-way wave equation. There are also *wide-angle parabolic approximations* available. These lead to higher-order partial differential equations,[16] and are frequently used in underwater acoustics and geophysical applications. They do not, however, appear that frequently in ultrasonic imaging. The use of a focused beam and high frequency implies that the diffraction effect is less significant for ultrasound. The 15° approximation is therefore thought to be adequate. This leads to the Khokhlov-Zabotskaya-Kuznetsov (KZK) equation[17,18] or variations of it.

The KZK equation is conveniently solved using operator splitting and propagation in space. The one-way nature of the KZK equation, combined with reasonable boundary conditions such as a *perfectly matched layer* (PML),[19,20] has the effect that the computational complexity of solving this equation is much lower than that of solving the full wave equation. Fast numerical solutions may therefore be implemented.[14] Measurements have also been published which verify that the KZK equation accurately describes the propagation of an ultrasound beam in a homogeneous medium.[21] In a heterogeneous medium, however, where reflections are important, the KZK equation will not provide an accurate description. This is the case for a medium containing bone structures surrounded by muscle and fat.

In order to study aberration, the medium may be replaced by a small number of planes in space, at which the propagating wave is modified. These planes are usually referred to as *phase screens*. The pulse is then propagated in a homogeneous medium between these screens.[7,10] This approach has the advantage of retaining only a forward propagating wave, and thus does not mix the acoustic noise caused

by aberration with that caused by reverberation. Presented here is an alternative approach, where a one-way wave equation is derived for propagation of ultrasound in heterogeneous soft tissue. A numerical solution of this equation is then found by means of operator splitting. The work is based on an extension of the parabolic approximation to heterogeneous media.[22]

The paper is organised as follows: a governing wave equation is presented in Sec. II.A. Section II.B describes the approximations leading to a one-way wave equation, before the power-law absorption model is introduced in Sec. II.C. In Sec. II.D operator splitting is then presented as a means to solve this equation. The numerical implementation of the solution is described in Sec. III. The simulation method is validated in Sec. IV by comparing it to analytic solutions in special cases; numerical solutions of the full wave equation obtained by other methods; and to measurements using an annular array in a water tank. Concluding remarks are given in Sec. V.

II Theory

II.A Governing wave equation

Sound is propagated through a medium as a pressure wave, inducing local vibrations, *i.e.* small deviations from an equilibrium position for each material point. Furthermore, in ultrasound imaging, the transducer induces these vibrations on the tissue surface. Therefore, the governing equations take a convenient form when expressed in material coordinates, as opposed to the conventional use of spatial coordinates in fluid mechanics.

Let $\rho(r)$ and $\kappa(r)$ be the tissue density and compressibility at equilibrium position r, respectively. Furthermore, let $\Psi(r,t)$ be the displacement of tissue at time t. A constitutive material relation which accounts for nonlinear elasticity and linear relaxation loss is[12]

$$-\nabla\cdot\Psi = \kappa p - \beta_n(\kappa p)^2 - \kappa\mathscr{L}p. \tag{3.1}$$

Here, $\mathscr{L}$ is a linear operator accounting for loss, and $\beta_n = 1 + B/2A$ is the *coefficient of nonlinearity*. Combined with conservation of momentum, $\rho\ddot{\psi} = -\nabla p$, this leads to a generalised Westervelt equation[12]

$$\kappa\ddot{p} - \nabla\cdot\left(\frac{1}{\rho}\nabla p\right) = \frac{d^2}{dt^2}\left(\beta_n\kappa^2p^2 + \kappa\mathscr{L}p\right).$$

Introducing a *normalised pressure*, $p = p_*/\sqrt{\rho}$, the following simplification is possible:[23]

$$\nabla\cdot\left(\frac{1}{\rho}\nabla p_*\right) = \frac{1}{\sqrt{\rho}}\nabla^2 p - p\nabla^2\frac{1}{\sqrt{\rho}}.$$

Table 3.1: Values for some physical parameters in medical ultrasound imaging at 1 MHz and 37°C. (See Duck.[24])

tissue	c [mm/µs]	ρ [mg/mm^3]	β_n	α [dB/mm]	b
fat	1.436	0.928	5.8	0.50	0.9
muscle	1.550	1.060	3.9	0.05	1.1
blood	1.584	1.060	4.0	0.01	1.2
water	1.524	0.993	3.7	0.00014	2.0

Table 3.2: Scales relating dimensional variables to dimensionless variables.

speed of sound	$c = c_* / c_s$	$c_s = 1.54\,\text{mm/µs}$
density	$\rho = \rho_* / \rho_s$	$\rho_s = 1\,\text{mg/mm}^3$
acoustic pressure	$p = p_* / p_s$	$p_s = 1\,\text{MPa}$
time	$t = t_* / t_s$	$t_s = 1\,\mu\text{s}$
space	$x = x_* / c_s t_s$	
normalised pressure	$p = p_* \sqrt{\rho}_s / p_s$	
density fluctuation	$g = g_* x_s^2$	

Using this identity together with $\kappa\rho = 1/c^2$, a wave equation for the normalised pressure p is obtained,

$$\nabla^2 p - \frac{1}{c^2}\ddot{p} = g\,p - \frac{\beta_n}{\sqrt{\rho}c^4}\frac{\partial^2 p^2}{\partial t^2} - \frac{1}{c^2}\frac{\partial^2 \mathscr{L} p}{\partial t^2},$$

where $g = \sqrt{\rho}\nabla^2\left(1/\sqrt{\rho}\right)$ describes density fluctuations.

Typical values for tissue parameters are listed in Table 3.1. Furthermore, considering ultrasound pulses with frequency in the MHz range and acoustic pressures around 1 MPa, a set of natural scales for the equation may be inferred. These scales are listed in Table 3.2.

The wave equation in dimensionless form is therefore

$$\nabla^2 p - \frac{1}{c^2}\ddot{p} = g\,p - \frac{p_s}{\rho_s c_s^2}\frac{\beta_n}{\sqrt{\rho}c^4}\frac{\partial^2 p^2}{\partial t^2} - \frac{1}{c^2}\frac{\partial^2 \mathscr{L} p}{\partial t^2}. \tag{3.2}$$

The acoustic pressure, p_*, may be recovered from the scaled normalised pressure, p, through the relation

$$p_* = p_s\sqrt{\rho_s}\,p\sqrt{\rho}.$$

Table 3.3: Typical values for the coefficients in Eq. (3.4) at 37°C

tissue	$\epsilon_t\,[10^{-1}]$	$\epsilon_n\,[10^{-3}]$	$\epsilon\,[10^{-3}]$
fat	-0.75	3.36	11.0
muscle	0.06	1.55	0.79
blood	0.27	1.46	0.15
water	-0.11	1.63	0.0004

II.B Approximations

With an appropriate choice of scale for the speed of sound, the average speed of sound may be assumed to be 1. Let the deviation from this average be described using $c_1(r)$ through

$$\frac{1}{c^2} = 1 - 2\gamma c_1.$$

A suitable value for the dimensionless scaling factor γ is 0.1 for soft tissue.

If the main direction of propagation is the z-direction, then a change of variables $\tau = t - z$ yields the equation

$$\frac{\partial^2 p}{\partial\tau\partial z} = \frac{1}{2}\left(\nabla^2 - g\right)p - \epsilon_t\ddot{p} + \frac{\epsilon_n}{2}\frac{\partial^2 p^2}{\partial\tau^2} + \epsilon\frac{\partial^2 Lp}{\partial\tau^2}.$$

This change of variables is known as *retarded time*. The coefficients $\epsilon_t = \gamma c_1$, $\epsilon_n = p_s\beta_n/\rho_s c_s^2\sqrt{\rho}c^4$ and ϵ are spatially variable. With the introduction of ϵ, a convenient change from $\mathscr{L}$ to L has also been made as $\epsilon L = \mathscr{L}/2c^2$.

For directional sound beams the *parabolic approximation* $\partial^2 p/\partial z^2 = 0$ is valid due to the introduction of retarded time. Letting $\nabla^2 = \nabla_\perp^2 + \partial^2/\partial z^2$ leads to

$$\frac{\partial^2 p}{\partial\tau\partial z} = \frac{1}{2}\left(\nabla_\perp^2 - g\right)p - \epsilon_t\ddot{p} + \frac{\epsilon_n}{2}\frac{\partial^2 p^2}{\partial\tau^2} + \epsilon\frac{\partial^2 Lp}{\partial\tau^2}. \tag{3.3}$$

With $g = 0$ and classical loss $\epsilon L = \delta\dot{p}/c^2$, where δ is the diffusivity, this is the well-known KZK equation.[14]

Integrating Eq. (3.3) with respect to time produces the final dimensionless equation

$$\frac{\partial p}{\partial z} = \frac{1}{2}\int_{-\infty}^{\tau}\left(\nabla_\perp^2 - g\right)p\mathrm{d}\tau + \left(\epsilon_n p - \epsilon_t\right)\dot{p} + \epsilon\frac{\partial Lp}{\partial\tau}. \tag{3.4}$$

Values for the coefficients ϵ_t, ϵ_n and ϵ for different tissue types are given in Table 3.3.

The parabolic approximation modifies the equation in such a way that it is no longer able to describe travelling waves in both directions, and thus does not model

reverberations in a heterogeneous medium. Since reverberations have been reported to produce only minor distortions in soft tissue,[13,25] this should not reduce the accuracy of the simulation significantly.

II.C Power-law absorption model

Amplitude damping for a narrow-band signal which propagates a distance h is commonly defined as

$$\alpha = \frac{20}{h} \log_{10} \frac{|p(0)|}{|p(h)|}. \tag{3.5}$$

Furthermore, relaxation is modelled as a frequency-dependent loss through $\alpha(f) = af^b$, where a and b are constants and f is frequency. This is the commonly used *power-law absorption model*. It is a phenomenologic model for frequency-dependent absorption in tissue, and is valid for a wide range of media. In particular it provides a good description of soft tissue.[24]

Equation (3.5) may be used to represent $\epsilon \partial Lp/\partial\tau$ in Eq. (3.4) through its temporal Fourier transform

$$\begin{aligned} \mathscr{F}\{\partial Lp/\partial\tau\} &= -|\omega|^b \mathscr{F}\{p\}, \\ \epsilon &= \frac{\ln 10}{20} \frac{a}{(2\pi)^b}. \end{aligned} \tag{3.6}$$

This model is not physically correct since the operator L as defined by Eq. (3.6) violates the principle of causality. The model may be amended by letting

$$\mathscr{F}\{\partial Lp/\partial\tau\} = \left[-|\omega|^b + i\beta(\omega)\right] \mathscr{F}\{p\},$$

where $\beta(\omega)$ is found using Kramers-Kronig relations.[26,27] However, as this does not have any significant impact on the presented results, and introduces only minor modifications to the implementation, it is not discussed further.

II.D Operator splitting approach

A phenomenological reasoning behind applying operator splitting to solve Eq. (3.4) is that the physical effects are local in space, and that for small steps they may be considered independent of each other. A mathematical foundation is found by combining the Lie-Trotter product formula[28] (Thm. 10.17) with the *product integral*.[29] The Lie-Trotter product formula states conditions under which the solution of an abstract Cauchy problem

$$\frac{\partial u}{\partial t} = (A + B)\, u,$$

where A and B are operators, may be obtained as a limit

$$\begin{aligned} u(t) &= \exp\left(t\left[A+B\right]\right) u(0) \\ &= \lim_{n\to\infty}\left[\exp\left(\frac{t}{n}A\right)\exp\left(\frac{t}{n}B\right)\right]^n u(0). \end{aligned}$$

A product integral, on the other hand, defines the integral of an operator $A(t)$, such that

$$\begin{aligned} u(t) &= \left(\prod_0^t e^{hA(\tau)\mathrm{d}\tau}\right) u(0) \\ &\equiv \lim_{n\to\infty}\exp\left(\frac{t}{n}A_{n-1}\right)\ldots\exp\left(\frac{t}{n}A_1\right)\exp\left(\frac{t}{n}A_0\right) u(0) \end{aligned}$$

is the solution of $\partial u/\partial t = A(t)u$ when $A_k = A(\frac{t}{n}k)$. In both cases the exponential function $\exp(hA)$ is used to formally denote the operator which sends the initial condition $u(0)$ onto the solution $u(h)$ of the differential equation $\partial u/\partial t = Au$.

Equation (3.4) is of the form

$$\frac{\partial p}{\partial z} = (A_d + A_n + A_l)\, p,$$

where the operators A_d, A_n and A_l account for diffraction and scattering, nonlinear elasticity, and energy loss, respectively

$$A_d(z)\, p = \frac{1}{2}\int_{-\infty}^{\tau}\left[\nabla_\perp^2 - g(z)\right] p\mathrm{d}\tau, \tag{3.7}$$

$$A_n(z)\, p = \left[\epsilon_n(z)\, p - \epsilon_t(z)\right]\dot{p}, \tag{3.8}$$

$$A_l(z)\, p = \epsilon(z)\frac{\partial L(z)\, p}{\partial \tau}. \tag{3.9}$$

Formally, the solution of Eq. (3.4) is denoted $p(z+h) = \exp(h[A_d + A_n + A_l])\, p(z)$. Furthermore, if the operators are bounded, *i.e.* a smooth solution with bounded derivatives, the error of the approximation

$$p(z+h) \approx e^{hA_d}\, e^{hA_l}\, e^{hA_n}\, p(z)$$

is $O(h^2)$. It is therefore referred to as a first-order approximation, often denoted as *Gudonov splitting*. *Strang splitting*[30] may be used as an alternative method for combining the solution operators in order to increase the formal order of the approximation, *e.g.*

$$p(z+h) \approx e^{\frac{h}{2}A_d}\, e^{\frac{h}{2}A_n}\, e^{hA_l}\, e^{\frac{h}{2}A_n}\, e^{\frac{h}{2}A_d}\, p(z).$$

The order of convergence, however, will depend heavily on the solution, and not necessarily adhere to this formal order. This is described as *order reduction* in the literature.

III Implementation

Equation (3.4) is valid in both two dimensions (2D) and three dimensions (3D). The only thing that is different is the term A_d. The implementation presented is in 2D. The extension to full 3D is straightforward, and only limited by computational power, although care should be taken in order to achieve the same accuracy in all directions. This problem is addressed in Ref. 31.

The computation starts at the plane $z = 0$ with an initial condition $p(x,0,t) = f(x,t)$. The propagation is performed in steps of length h in the direction of z, such that $z_k = kh$.

For the operator splitting to work well, an efficient solution for each individual equation is needed. The numerical approximation of the exact solution operator, $\exp(hA)$, is denoted $\mathscr{U}_A^h$. In this notation an approximate solution to the equation as a whole is given by

$$p(z_{k+1},t) = \mathscr{U}_{A_d}^h(z_k)\mathscr{U}_{A_n}^h(z_k)\mathscr{U}_{A_l}^h(z_k)\,p(z_k,t).$$

For the exact solution operators, an arbitrarily accurate approximation may be obtained by choosing a small enough step size to eliminate the splitting error. For the numerical solution, the step size should not be chosen in an arbitrary manner. When the splitting error is of the same order of magnitude as the numerical error in each of the numerical solution operators, decreasing the step size further may, in fact, amplify the error. A simple application of the triangle inequality illustrates this. The step size should be selected such that the splitting error is of the same order of magnitude as the accuracy of each of the numerical solution operators. This may be viewed as a form of *Morzov's discrepancy principle* known from the theory of regularisation and inverse problems.[32]

III.A Absorption

The absorption is defined in the frequency domain by Eq. (3.6). The Fourier transform is therefore well suited as a solution operator for the absorption term. Letting $\mathscr{F}$ and $\mathscr{F}^{-1}$ be the temporal Fourier transform and its inverse transform, respectively,

$$\begin{aligned} p(z_{k+1},\tau) &= e^{hA_l(z_k)}\,p(z_k,\tau) \\ &= \mathscr{F}^{-1}[\mathscr{F}(p)(z_k,\omega)\exp(-\epsilon(z_k)\omega H(z_k,\omega)\,h)], \end{aligned}$$

with

$$H(z_k,\omega) = \operatorname{sign}(\omega)|\omega|^{b(z_k)-1}.$$

Using the Fast Fourier Transform (FFT) in the implementation, a solution operator $\mathscr{U}_{A_l}^h(z_k)$ is obtained.

The main limitation for the accuracy of this solution operator is in applying the FFT over discontinuities at the edges of the signal. The computation domain is therefore large enough in the temporal direction to make the pulse taper to zero at both ends.

In order to apply the FFT to find the numerical solution, the grid points must be uniformly spaced in the temporal direction. An alternative to using the FFT is to implement the solution in the time domain.[33,34] This is not pursued here.

III.B Nonlinearity

When the step size h is short, *i.e.* $h < 1/|\partial p/\partial z(z_k,\tau)|$, the nonlinear term is solved by the method of characteristics

$$\begin{aligned} p(z_{k+1},\tau) &= p\big(z_k, \tau_k - h\Delta\big[z_k, p(z_k,\tau_k)\big]\big), \\ \Delta\big[z_k, p(z_k,\tau_k)\big] &= \frac{\epsilon_n(z_k)+\epsilon_n(z_{k+1})}{2} p(z_k,\tau_k) \\ &\quad - \frac{\epsilon_t(z_k)+\epsilon_t(z_{k+1})}{2}. \end{aligned}$$

This returns the solution at grid points which are not equally spaced in the temporal direction. In order to preserve equally-spaced grid points, the function $p(z_{k+1},t)$ is therefore re-sampled. This introduces an interpolation error. As long as the pulse is sampled with a sufficiently high sampling frequency, the interpolation error is negligible. The solution operator including the re-sampling is $\mathscr{U}^h_{A_n}(z_k)$.

III.C Diffraction and scattering: finite difference model

In order to find a numerical solution for the diffraction and scattering effects defined in Eq. (3.7), an implicit Euler scheme was implemented

$$\begin{aligned} p(z_{k+1},\tau_k) &= p(z_k,\tau_k) + h\frac{\partial p}{\partial z}(z_{k+1},\tau_k) \\ &= p(z_k,\tau_k) + p(z_{k+1},\tau_{k-1}) - p(z_k,\tau_{k-1}) \\ &\quad + h\frac{1}{2}\int_{\tau_{k-1}}^{\tau_k}\left[\frac{\partial^2}{\partial x^2} - g(z_{k+1})\right] p(z_{k+1},\tau)\mathrm{d}\tau. \end{aligned}$$

The second derivative of p with respect to x was approximated by a standard fourth-order central differencing scheme which may be represented by a banded matrix D. Furthermore, the integral was evaluated using a trapezoidal approximation. Let I denote the identity matrix and $B_k = D - \mathrm{diag}\big[g(z_{k+1})\big]$, where $\mathrm{diag}\big[g(z_k)\big]$ is the diagonal matrix with entries from $g(z_k)$. Let $h_\Delta = h\Delta t/4$. Then

$$\begin{aligned} (I - h_\Delta B_k)\,p(z_{k+1},\tau_k) = &\, p(z,\tau_k) - p(z_k,\tau_{k-1}) \\ &+ (I + h_\Delta B_k)\,p(z_{k+1},\tau_{k-1}). \end{aligned}$$

This set of equations may be solved inductively by assuming the solution to be zero for some time τ_0.

In a limited computational domain, appropriate boundary conditions must be applied in order to avoid reflection artifacts. This was achieved by adding a PML at the boundary of the domain.[19,20]

III.D Diffraction and scattering: pseudo-differential model

Equation (3.4) was derived using the parabolic approximation. This is exact for simple waves, and a good approximation for directive sound beams when the curvature of the wave front is small. In a heterogeneous medium the wave front may undergo deformations which cause the curvature to be too large for this approximation to be adequate. Higher-order parabolic approximations may be used to improve the results in such cases.[35] Implementation of these is also discussed in Ref. 31. Alternatively, the diffraction operator resulting from the full wave equation may be solved in the forward direction using the *angular spectrum method*. This leads to the pseudo-differential model presented here.

Comparing Eq. (3.4) and Eq. (3.2), the operator A_d is a one-way approximation of the full wave equation

$$\frac{\partial^2 p}{\partial z^2} = \frac{\partial^2 p}{\partial t^2} - \frac{\partial^2 p}{\partial x^2} + g\,p, \tag{3.10}$$

only expressed in retarded coordinates (z,τ). Define the functions ϕ and U as

$$\phi(x,z,\tau,h) = e^{hg}\,p(x,z,\tau)$$

$$U(k,\omega,h) = \begin{cases} e^{-ih\omega\left(1+\sqrt{1-(k/\omega)^2}\right)} & ,\omega^2 > |k|^2 \\ e^{-ih\omega\left(1-i\sqrt{(k/\omega)^2-1}\right)} & ,\text{otherwise.} \end{cases}$$

Furthermore, let $\hat{\phi}(k,z,\omega,h)$ be the Fourier transform of ϕ with respect to x and τ. An approximate solution to Eq. (3.10) is then given by

$$p(x,z+h,\tau) = \mathscr{F}^{-1}\left\{U(k,\omega,h)\hat{\phi}(k,z,\omega,h)\right\},$$

where $\mathscr{F}^{-1}$ represents inverse Fourier transform with respect to k and ω. For $g = 0$ the solution is exact and is what Bamberg *et al.* refer to as approximating the wave equation by a *pseudo-differential equation*.[22] The resulting one-way wave equation will therefore be referred to as the *pseudo-differential model*.

IV Validation

In order to verify the simulation method presented, the numerical results were compared to various references, including known analytic solutions, a numerical

solution to the full wave equation, and to measurements in a water tank.

IV.A Homogeneous tissue

Burgers equation - analytic

If the transmitted pulse is a plane wave propagating in water, Eq. (3.4) reduces to

$$p_z = \epsilon_n p\dot{p} + \epsilon\ddot{p}.$$

A simple change of variables $t = z$ and $x = -\epsilon_n\tau$ transforms this into a viscous Burgers' equation on standard form with viscosity $\nu = \epsilon/\epsilon_n^2$. The numerical solution may therefore be compared to analytic solutions in this case.

An analytic solution based on a δ-pulse initial condition[36] is used here. To avoid the difficulties of representing a δ-pulse numerically, the analytic solution after propagating a distance of 20 mm was used as the initial condition for the numerical solution. (See Fig. 3.1.) The initial condition was then propagated one step forward and compared to the analytic solution.

Figure 3.2 shows a very good match between the reference solution and the numerical solution. The plot indicates that the Gudonov splitting scheme has a local error of order slightly less than h^2, almost matching the formal order of the scheme. The Strang splitting has a local error of order somewhere between two and three for this initial condition, and does not, therefore, obtain its formal order of two. The local error of both schemes has a kink where the accuracy changes. When the step size is decreased beyond this point, the local error seems to be of order h. From here on the errors of the two schemes are identical. The point at which the kink occurs is moved down by using a denser grid in the temporal direction, *i.e.* increasing the accuracy of each of the numerical solution operators sufficiently. The kink indicates the point at which the splitting error becomes insignificant compared to the error of each solution operator.

Hydrophone measurements

The experimental measurements used in this study were recorded in a water-tank using a hydrophone (SEA PVDF-Z44-0400). A pulse with centre frequency of 2.9 MHz was transmitted from an annular array probe (Vingmed Sound APAT 3.25) with a diameter of 14.7 mm and 78.0 mm radius of curvature. This results in an approximate f-number of 5.2. In order to obtain an initial condition for the numerical solution to the wave propagation, measurements of the near-field were recorded 8.5 mm away from the centre of the probe, perpendicular to the focal axis (see Fig. 3.3). By doing so, the problem of modelling the physical characteristics of the transducer, for example the curved surface and element sizes, was avoided. However, the near-field measurements contain errors. They are not, therefore, axis-symmetric. Thus, the

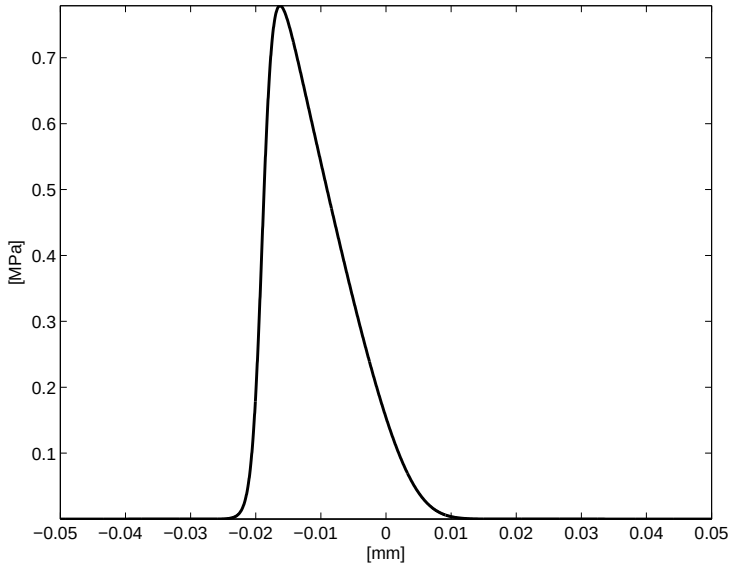

Figure 3.1: Initial condition for comparisons with analytic solution of Burgers' equation.

near-field measurements were modified slightly. Any tilt in the measurements due to the hydrophone scanning not being perpendicular to the focal axis was removed. A representative half-axis of the measurement was then selected and rotated around the focal axis to produce the desired axis-symmetric initial condition. (See Fig. 3.4.)

The rectified near-field was then numerically propagated to a depth of 69.5 mm using the model in Eq. (3.4). Figures 3.5 and 3.6 display a high degree of consistency between the numerical solution of the model and the measurements. Any discrepancies are just as likely to be caused by the calibration of the hydrophone and imperfections in the transmitted beam as they are by numerical and model errors.

IV.B Heterogeneous tissue

In order to evaluate how accurately the one-way wave equation approximates the propagation through a heterogeneous medium, the numerical solution of Eq. (3.4) was compared to a numerical solution of the full wave equation. A numerical solution of a wave equation based on a constitutive relation which is inverted compared to Eq. (3.1), was presented by Wojcik *et al.*.[37] Their solution used a pseudo-spectral method to solve a system of equations for p and $\dot{\Psi}$, instead of eliminating Ψ to obtain a scalar equation for p. It is, however, still comparable to the equation presented here. Therefore, a publicly-available implementation of this pseudo-spectral method

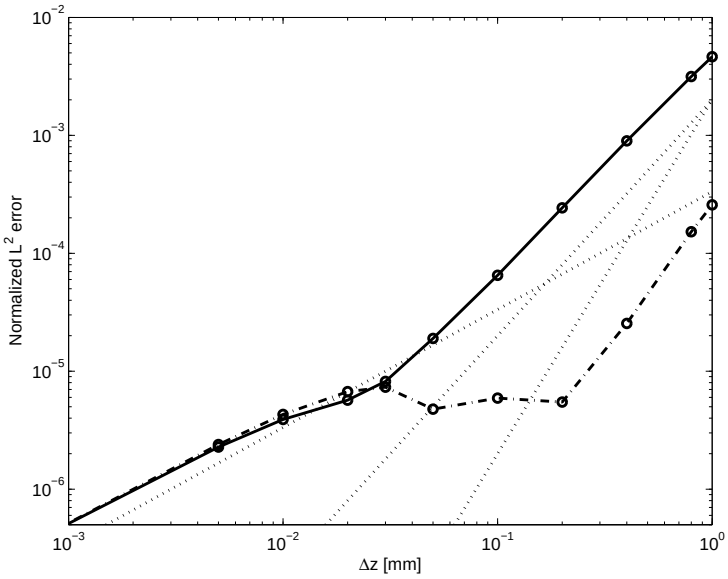

Figure 3.2: Relative local L^2 error for the numerical solution when compared to an analytic solution to Burgers' equation. Solid line: Gudonov splitting. Dash-dot line: Strang splitting. Dotted lines: slopes for local first-, second- and third-order schemes.

was used to obtain a numerical solution of the full wave equation.[38]

A plane wave propagating in the z-direction was used as an initial condition for the full wave equation. The propagating wave was recorded in two planes parallel to the wave front, one at each side of the heterogeneity in the tissue. The recorded incoming wave was then used as initial condition for the numerical solution of both the one-way wave equation and the pseudo-differential model. The solutions were then compared with the recorded wave front obtained from the solution of the full wave equation.

Figure 3.7 shows the sound speed variations in the heterogeneous tissue used for the simulation comparison.

Figure 3.8 displays consistency between the numerical solution of the full wave equation and the numerical solution of the one-way wave equation. However, it is clear that the parabolic model has problems representing parts of the propagating pulse which travel at a wide angle out from the propagation axis.

Figure 3.9 shows that the pseudo-differential model is much more consistent with the solution of the full wave equation than the parabolic model was. To illustrate this further, a cross-section of the solutions is plotted in Fig. 3.10. Not surprisingly, the pseudo-differential model is also able to resolve propagation at a wide angle out from

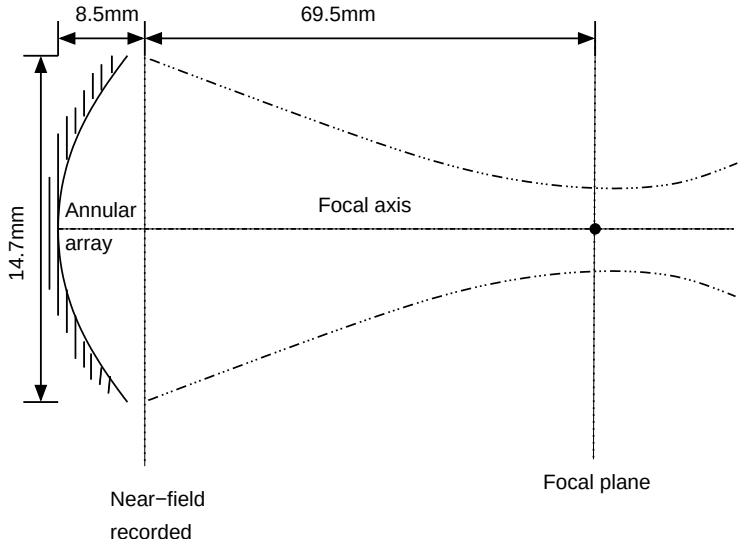

Figure 3.3: Experimental setup for comparing the KZK-based simulation to hydrophone measurements.

the propagation axis. The discrepancy is most likely caused by wave reflections of the propagating wave not being accurately modelled by the pseudo-differential model.

A major benefit from using a one-way approximation to the wave equation, instead of the full wave equation, is in the reduced computational complexity of finding a numerical solution. Although only a crude optimisation of the implementations was performed, the computational time for propagating a 5 MHz pulse through the 9×9 mm computational domain in Fig. 3.7 using 256×256 spatial grid points was almost four times longer for the full wave equation compared to the pseudo-differential method (26.5 min vs. 6.8 min on the available hardware; a 500 MHz PIII running MATLAB 6.5 under Linux). Solution methods based on one-way wave equations, such as the pseudo-differential approximation or the parabolic approximation, by nature scale linearly as a function of propagation distance. Their advantage therefore increases for larger propagation distances.

V Concluding remarks

A one-way wave equation, Eq. (3.4), for modelling the forward wave propagation of an ultrasound pressure field, along with a numerical solution method, has been presented. The equation was derived from a parabolic approximation to the full wave

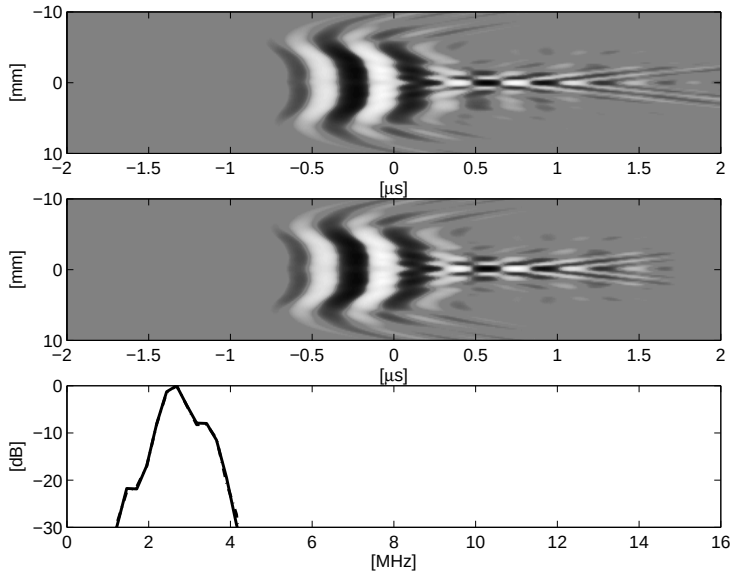

Figure 3.4: Initial conditions used for the numerical solution. Top: recorded near-field. Middle: near-field adjusted to be axis-symmetric. Bottom: frequency content of the initial condition at the centre axis.

equation. The solution concurs with analytic reference solutions and experimental measurements in a homogeneous medium. The basic features of the numerical solution are also the same as those of a numerical reference, obtained as a solution to the full wave equation. However, for a deformed wave front, the propagation at large angles out from the axis of propagation is not accurately represented using the parabolic model.

In order to represent propagation in an aberrating medium, an approximation based on the angular spectrum method was applied. The resulting pseudo-differential model, while still being a one-way model, significantly improves the results over the parabolic model for the heterogeneous medium. This suggests that a higher-order (wide-angle) parabolic approximation may be of interest when modelling ultrasonic aberration.

Since the problem has been broken down into simple one-dimensional problems, connected only by the so-called diffraction operator, this model is well suited for implementation on a parallel computer. Only an implementation of the 2D version has been demonstrated here. There is, however, nothing 2D-specific in the model. It should work equally well in 3D.

A higher-order parabolic approximation, which is local in space, will most likely

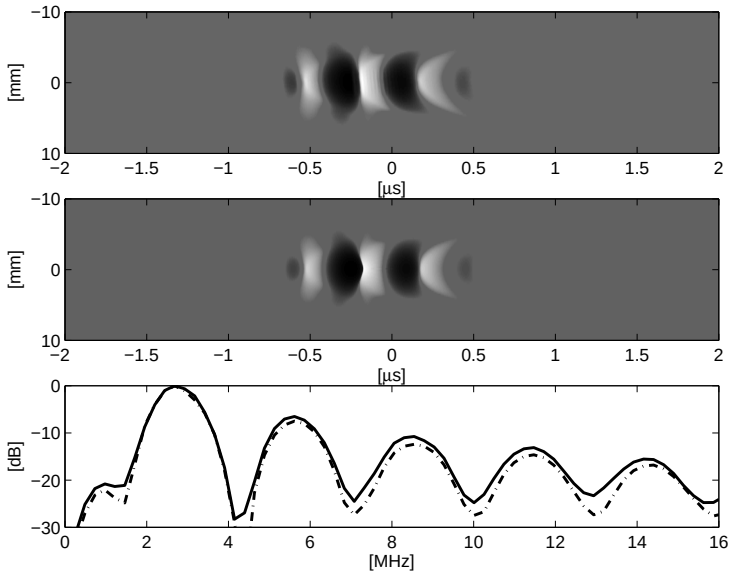

Figure 3.5: Comparison between measurement and numerical propagation in the focal plane, 69.5 mm away from the initial plane. Top: measured pulse. Middle: numerically propagated pulse. Bottom: spectrum of measured and numerically propagated pulses at the centre axis.

be better suited for parallel implementation than the use of a non-local method such as the angular spectrum approach presented here. This is because a non-local solution method will require much more communication between each processor than a local method.

Acknowledgments

The authors thank Safiye Dursun and Dr. Tonni Johansen for collection of the data used to validate the simulation. Dr. Cathrine Tegnander, Professor Bjørn Angelsen and Professor Harald Krogstad at NTNU are thanked for useful discussions. Support for this work was provided by The Research Council of Norway.

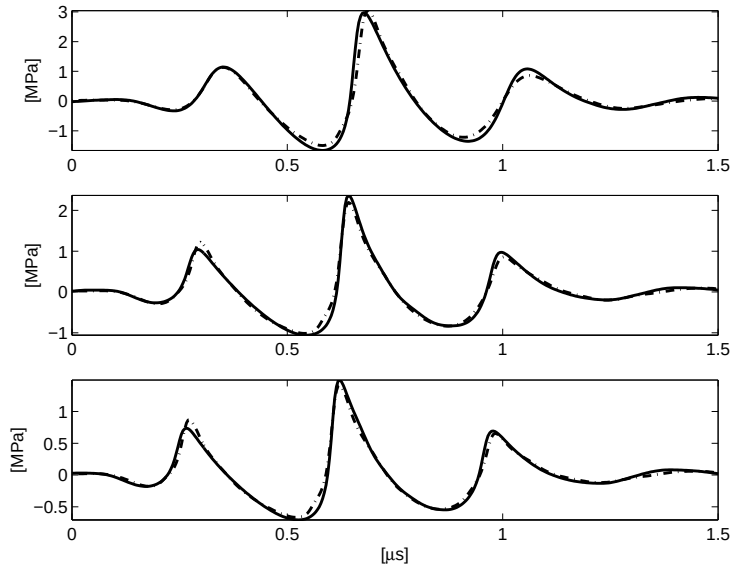

Figure 3.6: Comparison between centre axis of measurement and numerical centre axis of numerical propagation at various depths. Top: 39.5 mm propagation. Middle: 69.5 mm propagation. Bottom: 99.5 mm propagation.

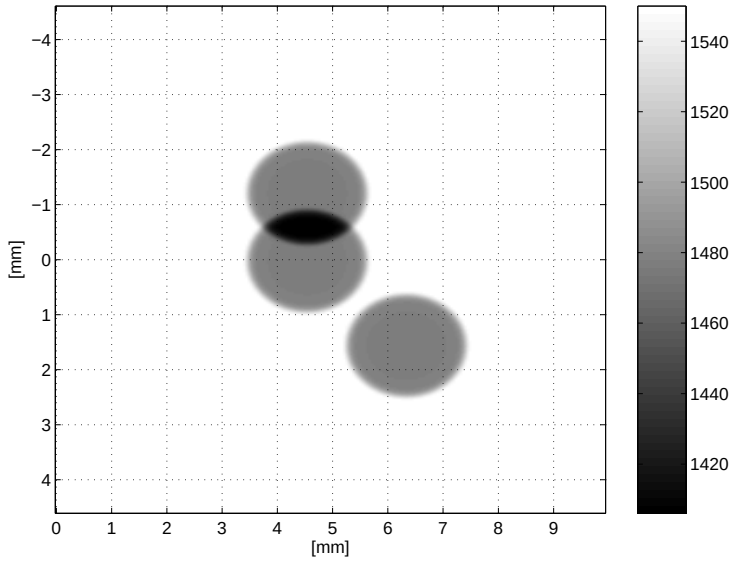

Figure 3.7: Sound speed variations used for the simulation comparison.

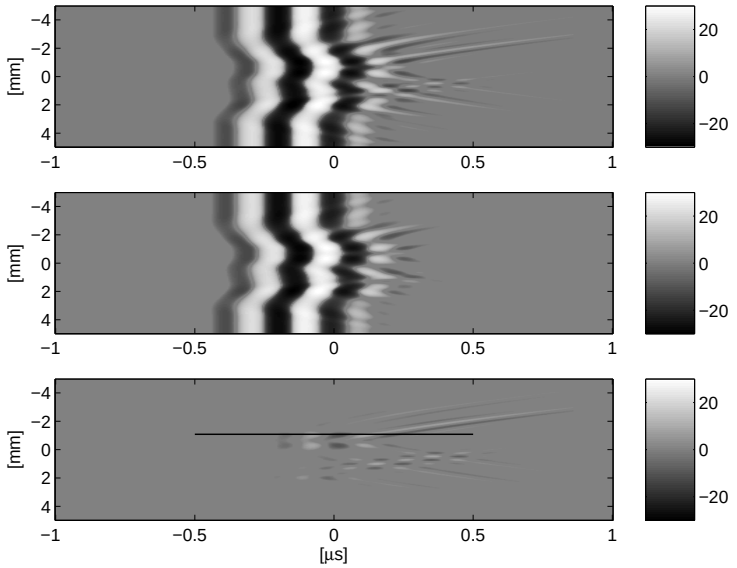

Figure 3.8: Comparison of the forward propagating wave fronts for the one-way wave equation using the parabolic approximation and the full wave equation. The wave fronts were recorded at a depth of 8.9 mm. Top: solution of the full wave equation. Middle: solution of the one-way wave equation. Bottom: difference between the two solutions. The line in the bottom picture indicates the location where the cross-section shown in Fig. 3.10 is made. A ± 30 dB logarithmic grey scale is used in the display.

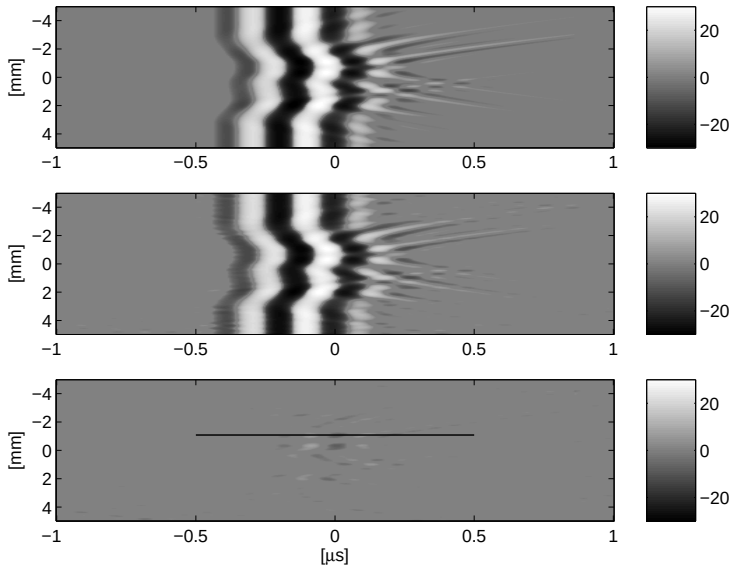

Figure 3.9: Comparison of the forward propagating wave fronts for the pseudo-differential model and the full wave equation recorded at 8.9 mm. Top: solution of the full wave equation. Middle: solution of the one-way wave equation. Bottom: difference between the two solutions. The line in the bottom picture indicates the location where the cross-section shown in Fig. 3.10 is made. A ± 30 dB logarithmic grey scale is used in the display.

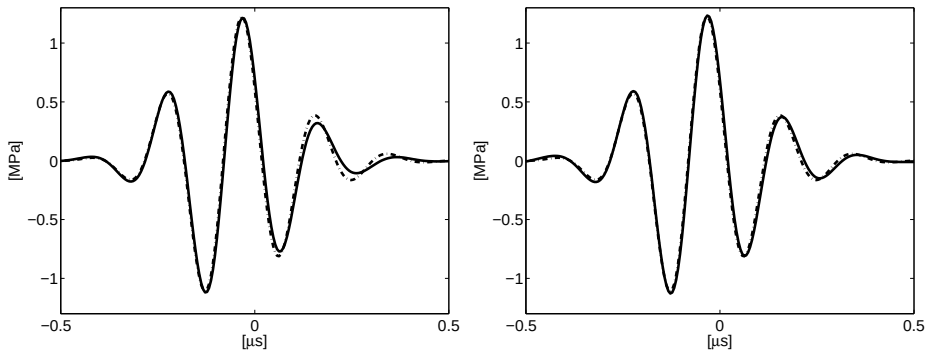

Figure 3.10: Cross-section comparing a numerical solution to the full wave equation (dash-dot line) to a numerical solution of the one-way models (solid line). The cross-section is made along the line indicated in Figs. 3.8 and 3.9. Left: parabolic model. Right: pseudo-differential model.

References

[1] U. Haberkorn, G. Layer, V. Rudat, I. Zuna, A. Lorenz, and G. van Kaick, "Ultrasound image properties influenced by abdominal wall thickness and composition," *J. Clin. Ultrasound*, vol. 21, pp. 423–429, 1993.

[2] L. Hinkelman, D.-L. Liu, L. A. Metlay, and R. C. Waag, "Measurements of ultrasonic pulse arrival time and energy level variations produced by propagation through abdominal wall," *J. Acoust. Soc. Am.*, vol. 95, no. 1, pp. 530–541, January 1994.

[3] G. E. Trahey, P. D. Freiburger, L. F. Nock, and D. C. Sullivan, "In-vivo measurements of ultrasonic beam distortion in the breast," *Ultrason. Imaging*, vol. 13, no. 1, pp. 71–90, 1991.

[4] P. D. Freiburger, D. Sullivan, B. H. LeBlanc, and G. E. Trahey, "Two-dimensional ultrasonic beam distortion in the breast: in-vivo measurements and effects," *Ultrason. Imaging*, vol. 14, pp. 398–414, 1992.

[5] Q. Zhu and B. D. Steinberg, "Wavefront amplitude distribution in the female breast," *J. Acoust. Soc. Am.*, vol. 96, no. 1, pp. 1–9, April 1994.

[6] M. Tabei, T. D. Mast, and R. C. Waag, "Simulation of ultrasonic focus aberration and correction through human tissue," *J. Acoust. Soc. Am.*, vol. 113, no. 2, pp. 1166–1176, February 2003.

[7] S. E. Måsøy, T. F. Johansen, and B. Angelsen, "Correction of ultrasonic wave aberration with a time delay and amplitude filter," *J. Acoust. Soc. Am.*, vol. 113, no. 4, pp. 2009–2020, April 2003.

[8] A. I. Nachman, J. F. Smith, and R. C. Waag, "An equation for acoustic propagation in inhomogeneous media with relaxation losses," *J. Acoust. Soc. Am.*, vol. 88, pp. 1584–1595, 1990.

[9] P. T. Christopher and K. J. Parker, "New approaches to nonlinear diffractive fields propagation," *J. Acoust. Soc. Am.*, vol. 90, no. 1, pp. 488–499, July 1991.

[10] A. P. Berkhoff and J. M. Thijssen, "Correction of concentrated and distributed aberrations in medical ultrasound imaging," in *Proc. 1996 IEEE-UFFC Ultrasonics Symposium*, 1996, pp. 1405–1410.

[11] G. Wojcik, J. Mould, F. Ayter, and L. Carcione, "A study of second harmonic generation by focused medical transducer pulses," in *Proc. 1998 IEEE-UFFC Ultrasonics Symposium*, 1998, pp. 1583–1588.

[12] G. Taraldsen, "Derivation of a generalized Westervelt equation for nonlinear medical ultrasound," *J. Acoust. Soc. Am.*, vol. 109, no. 4, pp. 1329–1333, April 2001.

[13] B. A. Angelsen, *Ultrasound imaging. Waves, signals and signal processing*. Trondheim, Norway: Emantec, 2000, vol. 2, http://www.ultrasoundbook.com.

[14] M. F. Hamilton and D. T. Blackstock, *Nonlinear Acoustics*. San Diego: Academic Press, 1997.

[15] F. Tappert, "The parabolic approximation method in wave propagation and underwater acoustics," in *Lectures in Physics*, J. B. Keller and J. S. Papadakis, Eds. New York: Springer, 1977, pp. 224–287.

[16] J. F. Claerbout, *Fundamentals of Geophysical Data Processing*. New York: McGraw-Hill, 1976.

[17] E. A. Zabotskaya and R. V. Khoklov, "Quasi-plane waves in the non-linear acoustics of confined beams," *Sov. Phys. Acoust.*, vol. 15, pp. 35–40, 1969.

[18] V. P. Kuznetsov, "Equations of nonlinear acoustics," *Sov. Phys. Acoust.*, vol. 16, pp. 467–470, 1971.

[19] J.-P. Berenger, "A perfectly matched layer for the absorption of electromagnetic waves," *J. Comp. Phys.*, vol. 114, no. 2, pp. 185–200, 1994.

[20] F. Collino, "Perfectly matched absorbing layers for the paraxial equations," *J. Comp. Phys.*, vol. 131, no. 1, pp. 164–180, 1997.

[21] A. Bouakaz, C. Lancée, and N. de Jong, "Harmonic ultrasonic field of medical phased arrays: Simulations and measurements," *IEEE Trans. Ultrason. Ferroelectr. Freq. Control*, vol. 50, no. 6, pp. 730–735, June 2003.

[22] A. Bamberg, B. Engqvist, L. Halpern, and P. Joly, "Parabolic wave equation approximations in heterogeneous media," *SIAM J. Appl. Math.*, vol. 48, no. 1, pp. 99–128, 1988.

[23] L. Brekhovskikh and O. Godin, *Acoustics of Layered Media I-II*, 2nd ed. Springer, 1999.

[24] F. A. Duck, *Physical properties of tissue*. London: Academic Press, 1990.

[25] T. D. Mast, L. Hinkelman, M. Orr, and R. C. Waag, "The effect of abdominal wall morphology on ultrasonic pulse distortion. part II. simulations," *J. Acoust. Soc. Am.*, vol. 104, no. 6, pp. 3651–3664, December 1998.

[26] R. D. L. Krönig, "On the theory of dispersion of x-rays," *J. Opt. Soc. Am.*, vol. 12, pp. 547–557, 1926.

[27] C. W. Horton, "Dispersion relationships in sediments and sea water," *J. Acoust. Soc. Am.*, vol. 55, pp. 547–549, 1974.

[28] I. Kappel, *Evolution equations and Approximations*. San Diego: Academic Press, 1997.

[29] J. Dollard and C. Friedman, *Product Integration with Applications to Differential Equations*, ser. Encyclopædia of mathematics and its applications, G.-C. Rota, Ed. Reading, Massachusetts: Addison-Wesley, 1979.

[30] G. Strang, "On the construction and comparison of difference schemes," *Numer. Anal.*, vol. 5, pp. 506–517, 1968.

[31] E. Bécache, F. Collino, and P. Joly, "Higher-order numerical schemes and operator splitting for solving 3D paraxial wave equations in heterogeneous media," INRIA, Rapport de recherche 3497, 1998.

[32] H. Engl, M. Hanke, and A. Neubauer, *Regularization of inverse problems*. Netherlands: Kluwer Academic Publishers, 2000.

[33] T. L. Szabo, "Time domain wave equations for lossy media obeying a frequency power law," *J. Acoust. Soc. Am.*, vol. 96, pp. 491–500, 1994.

[34] G. V. Norton and J. C. Norini, "Including dispersion and attenuation directly in the time domain for wave propagation in isotropic media," *J. Acoust. Soc. Am.*, vol. 113, no. 6, pp. 3024–3031, 2003.

[35] A. Bamberg, B. Engqvist, L. Halpern, and P. Joly, "Higher order paraxial wave equation a approximations in heterogeneous media," *SIAM J. Appl. Math.*, vol. 48, no. 1, pp. 99–128, 1988.

[36] G. B. Whitham, *Linear and Nonlinear Waves*. Wiley, 1974.

[37] G. L. Wojcik, B. Fornberg, R. C. Waag, L. Carcione, J. Mould, L. Nikodym, and T. Driscoll, "Pseudospectral methods for large-scale bioacoustic models," in *Proc. 1997 IEEE-UFFC Ultrasonics Symposium*, 1997, pp. 1501–1506.

[38] M. E. Anderson, "A 2D nonlinear wave propagation solver written in open-source matlab code," in *Proc. 2000 IEEE-UFFC Ultrasonics Symposium*, 2000. [Online]. Available: http://www.seas.rochester.edu/~maanders/sps2d.html

Chapter 4

Spectral estimation for characterisation of acoustic aberration

T. Varslot*, B. Angelsen†, R. C. Waag‡
*) Dept. Mathematical Sciences, NTNU
†) Dept. Circulation and Imaging, NTNU
‡) Ultrason. Reserch Lab, University of Rochester, New York 14627, USA

Spectral estimation based on acoustic backscatter from a motionless stochastic medium is described in order to characterise aberration in ultrasonic imaging. The underlying assumptions for the estimation are: the correlation length of the medium is short compared to the length of the transmitted acoustic pulse; an isoplanatic region of sufficient size exists around the focal point; and the backscatter can be modelled as an ergodic stochastic process. The goal for this work is to improve ultrasonic imaging by the use of aberration correction. Measurements were performed using a two-dimensional (2D) array system with 80×80 transducer elements and an element pitch of 0.6 mm. The f-number for the measurements was 1.2 and the centre frequency was 3.0 MHz with a 53% bandwidth. Relative phase of aberration was extracted from estimated cross-spectra using a robust least-mean-square-error method based on an orthogonal expansion of the phase differences of neighbouring wave forms as a function of frequency. Estimates of cross-spectrum phase from measurements of random scattering through a tissue-mimicking aberrator have confidence bands approximately $\pm 5^\circ$ wide. Both phase and magnitude are concordant with a reference characterisation obtained from a point scatterer.

I Introduction

An ultrasound image is a map of reflected sound intensity from different spatial locations. By focusing the transmitted sound pulse at a specific location, the intensity of the transmitted field is highest around the focal point. The reflected intensity then largely originates from this region. A limitation is therefore imposed on the image resolution by the size of the focal zone. The smallest obtainable size is limited by diffraction.

In medical ultrasonic imaging, the transmitted pulse typically travels through the body wall before arriving at the intended focal point. The body wall consists of a heterogeneous configuration of muscular, fatty, and connective tissue. As a result of propagation through a medium with variable speed of sound, the the focal zone of the geometrically-focused transmit-beam is widened, thus producing a degraded focus. The transmitted pulse is then said to be *aberrated*. Experimental studies of the abdominal wall [1,2] and breast tissue, [3,4,5] as well as simulations, [6,7] indicate that this aberration can significantly reduce the image resolution. The need to consider aberration in ultrasonic imaging is also shown in experimental studies that illustrate image degradation caused by aberration and image improvement resulting from aberration correction. [8,9]

Several different approaches have been suggested to counter the aberration. These are mostly based on either the time-reversal mirror [10] or a time-delay model for the aberration. [11,12] The need for a strong point scatterer in the time-reversal mirror limits its applicability in clinical applications. Furthermore, a time-delay screen may not be adequate for describing the aberration. This model does not describe the distortion of the pulse shape observed in medical ultrasound. [13] Moving the screen away from the transducer surface has been suggested as a way to characterise the pulse-shape distortion and amplitude fluctuation introduced by interference between different parts of the pulse, [14] but this too is an oversimplification that may not model aberration satisfactorily.

This paper uses an aberration model called a *generalised screen* by Angelsen [15] and a *filter bank* by Lin and Waag. [16] Using the time-reversal argument, the generalised screen will correspond to an ideal aberration correction filter. Finding the screen is therefore an important step on the way to perform aberration correction. For scattering from a spatially-stationary random distribution of scatterers, the generalised screen may be estimated from the cross-spectra of the measured signal at the transducer.

The aim of this paper is to determine the generalised screen using a set of scattering measurements from a motionless random medium with very short correlation length compared to the wavelength. Relatively independent measurement samples are obtained by focusing at different locations within the random medium for which the aberration is essentially the same. This limits the possible focal points to a region

in which essentially the same aberration path exists between the transmit-receive aperture and the focal point.

The paper is organised in the following way: after a brief review of classical spectral estimation in Sec. II.A, a characterisation of the aberration using the cross-spectrum of backscatter measurements is given in Sec. II.B. In Sec. II.C, a least-mean-square-error method for extracting the relative phase of the aberration from the spectral estimates is described. Implementation issues, signal processing, and metrics to evaluate the estimates are discussed in Sec. III. The experimental configuration and the measurement procedure are described in Sec. IV, and estimation[3] of aberration as frequency domain magnitude and phase are presented in Sec. V. Discussion and concluding remarks are given in Secs. VI and VII, respectively.

II Theory

II.A Spectral estimation

The subject of spectral estimation is described exhaustively in the literature.[17,18,19,20] Therefore, only important relations relevant to this article are offered here for the convenience of the reader and the introduction of notation.

The cross-covariance between two stationary second-order stochastic processes $X(t)$ and $Y(t)$ with zero mean is defined as

$$R_{XY}(s) = \mathrm{E}\left[X(0)\overline{Y(s)}\right],$$

where $\mathrm{E}[\cdot]$ is the expectation operator. The corresponding cross-spectrum $P_{XY}(\omega)$ is the Fourier transform of the covariance function.

Suppose the stochastic processes $X(t)$ and $Y(t)$ are ergodic, and the function $k(t)$ is a window function that satisfies the appropriate conditions[19] (Ch. 6).

Let $\lambda_M(t) = k(t/M)$, where M is a positive scaling parameter. An asymptotically unbiased, consistent estimator of $P_{XY}(\omega)$ is given by

$$P_{XY}^{(N)}(\omega) = \frac{1}{2\pi} \sum_{t=-(N-1)}^{N-1} \lambda_M(t) R_{XY}^{(N)}(t)\, e^{i\omega t},$$

where

$$R_{XY}^{(N)}(s) = \frac{1}{N} \sum_{t=0}^{N-|s|} X(t)\overline{Y(t+s)}.$$

This is known as the Blackman-Tukey estimator for the cross-spectrum, with window function λ_M. The implementation of this estimator will be based on the cross-periodogram of the processes, and therefore computed efficiently using the Fast Fourier Transform (FFT)[20] [Ch. 2].

The magnitude $r(\omega)$ and the phase $\theta(\omega)$ of the cross-spectrum can now be estimated as

$$\hat{\theta}(\omega) = \arg\left[P_{XY}^{(N)}(\omega)\right]$$
$$\hat{r}(\omega) = |P_{XY}^{(N)}(\omega)|.$$

Letting $I = \int |k(t)|^2 dt$, approximate expressions for the variance of these estimators are given by

$$\mathrm{Var}\left[\hat{\theta}(\omega)\right] \approx \frac{IM}{2N}\left(\frac{1}{|w_{XY}(\omega)|^2} - 1\right) \tag{4.1}$$
$$\mathrm{Var}\left[\hat{r}(\omega)\right] \approx \frac{IM}{2N}|P_{XY}(\omega)|^2\left(\frac{1}{|w_{XY}(\omega)|^2} + 1\right), \tag{4.2}$$

where

$$w_{XY}(\omega) = P_{XY}(\omega)/\sqrt{P_X(\omega)P_Y(\omega)}$$

is the coherence between the processes $X(t)$ and $Y(t)$. The variance is assumed to be small for these approximations to be valid [19] [Sec. 9.5.2].

II.B Characterisation of aberration

Let $p_0(\omega)$ be the temporal Fourier transform of a point source located at the position r_0. Assuming linear wave propagation in a homogeneous non-absorbing medium, the received signal at a position r on the transducer is

$$p_{r_0}^{(h)}(r,\omega) = p_0(\omega)\frac{e^{-i\omega|r-r_0|/c}}{4\pi|r-r_0|}$$

in the temporal-frequency domain. In this expression, c is the speed of sound. A superscript (h) is used to indicate quantities resulting from propagation through a homogeneous medium. Let $p_{r_0}(r,\omega)$ denote the temporal Fourier transform of the signal received from the same point source in the heterogeneous medium. If the wave propagation in the heterogeneous medium is linear, the relation between $p_{r_0}^{(h)}(r,\omega)$ and $p_{r_0}(r,\omega)$ may be described by a unique function $s_{r_0}(r,\omega)$ as

$$p_{r_0}(r,\omega) = s_{r_0}(r,\omega)p_{r_0}^{(h)}(r,\omega).$$

Using Huygens' principle, the temporal Fourier transform of the corresponding signal received from a general scatterer distribution $\sigma(r_0,\omega)$ is

$$p^{(h)}(r,\omega) = \int p_{r_0}^{(h)}(r,\omega)\mathrm{d}\sigma(r_0,\omega)$$

and

$$p(r,\omega) = \int p_{r_0}(r,\omega)\mathrm{d}\sigma(r_0,\omega),$$

where the integration in each expression is over the spatial support of σ. For a given r_f, let Ω be the largest neighbourhood of r_f in which $s_{r_0}(r,\omega)$ may be assumed constant as a function of r_0. If $p_{r_0}(r,\omega)$ is zero outside Ω, then the approximation

$$p(r,\omega) = s_{r_f}(r,\omega)\, p^{(h)}(r,\omega)$$

is valid. In this case, the function s_{r_f} is called the *generalised screen*, and Ω is denoted the *isoplanatic region*. Using a polar form for the complex function s_{r_f} and omitting the subscript r_f, the screen is

$$s(r,\omega) = A(r,\omega)\, e^{i\theta(r,\omega)},$$

where A and θ are real-valued functions, denoted the *magnitude of aberration*, and the *phase of aberration*, respectively. If $A(r,\omega) = a(r)$ and $\theta(r,\omega) = \omega\tau(r)/c$, this description is the commonly used time-delay and amplitude screen.

The scatterer distribution is assumed to have a correlation length which is very short compared to the wavelength of the transmitted pulse, so for all practical purposes the distribution is δ-correlated. Point-like reflectors distributed according to a spatial Poisson point process is an example. Let r_k be the coordinate of a particular transducer element k. Under this assumption, the received signal is a sample function of an approximate Gaussian stochastic process with zero mean for each r_k when the average number of point scatterers per unit area is large.[21] If, in addition, the received signal is a stationary process, a complete characterisation of $p(r_k,\omega)$ is given by the corresponding cross-power spectrum.

The cross-spectrum between the received signal at elements k and l is

$$\begin{aligned} P_{kl}(\omega) &= \mathrm{E}\left[p(r_k,\omega)\overline{p(r_l,\omega)} \right] \\ &= A(r_l,\omega)A(r_k,\omega)\, e^{-i[\theta(r_k,\omega)-\theta(r_l,\omega)]} P^{(h)}_{kl}(\omega), \end{aligned} \tag{4.3}$$

where $P^{(h)}_{kl}(\omega)$ is the cross-spectrum of the received signal without aberration. The cross-spectrum, thus, contains information about the phase and amplitude of the aberration.

Let $p_0(r,\omega)$ be the temporal Fourier transform of the transmit waveform used when imaging through a homogeneous medium. The time-reversal argument states that an optimal aberration correction for focusing at r_f may be achieved by replacing $p_0(r,\omega)$ with an aberration-corrected pulse $\overline{s(r,\omega)}p_0(r,\omega)$, *i.e.*, filtering the transmit pulse using a filter with transfer function equal to the complex conjugate of $s(r,\omega)$. Similarly, aberration correction for the receive pulse $p(r,\omega)$ is obtained by the same filter. Thus, the generalised screen corresponds to an aberration correction filter.[16]

II.C Relative phase

Relative phase

The angle of the cross-spectrum is a relative phase difference between all the pairs of transducer elements. Ideally, the relative phase across the transducer could be found by integration of these phase differences. In the presence of estimation error, however, errors accumulate and straightforward integration is unsatisfactory. Here, an estimate for the relative phase is found as a least-mean-square-error fit to the phase defined by the phase differences.

Let $\phi_i(\omega)$ be the relative phase at transducer element i. Following Liu and Waag, [13] $\phi_i(\omega)$ may be expressed as

$$\begin{aligned} \phi_{i+1}(\omega) - \phi_i(\omega) &= \theta_j(\omega), \\ \phi_{i+M+1}(\omega) - \phi_i(\omega) &= \theta_{j+1}(\omega), \\ \phi_{i+M}(\omega) - \phi_i(\omega) &= \theta_{j+2}(\omega), \\ \phi_{i+M}(\omega) - \phi_{i+1}(\omega) &= \theta_{j+3}(\omega), \end{aligned} \tag{4.4}$$

where θ_k is the phase of the appropriate cross-spectrum. In matrix notation, with the conventions in Fig. 4.1, Eq. (4.4) can be written

$$A\phi(\omega) = \theta(\omega). \tag{4.5}$$

For an $m \times n$ element transducer, the size of the matrix A is $L \times mn$, with $L = 4mn - 3(m+n) + 2$. As the rank of A is $mn-1$, this equation is solved by means of Moore-Penrose inverse $A^\dagger$ of A.

If $A = U\Sigma V^H$ is a singular value decomposition of A, then the Moore-Penrose inverse of A can be expressed

$$A^\dagger = V\Sigma^+ U^H,$$

where the diagonal matrix Σ^+ is defined

$$\Sigma^+_{ij} = \begin{cases} 1/\Sigma_{ij}, & \Sigma_{ij} \neq 0 \\ 0, & \Sigma_{ij} = 0. \end{cases}$$

Information across frequencies

The procedure described thus far produces a unique solution of the relative phase retrieval problem based on the phase of the cross-spectra, in the least-mean-square-error sense. However, as the estimate is formed for each frequency separately, the estimate does not include frequency-to-frequency information. This may introduce undesired jumps in the relative phase estimate as a function of frequency.

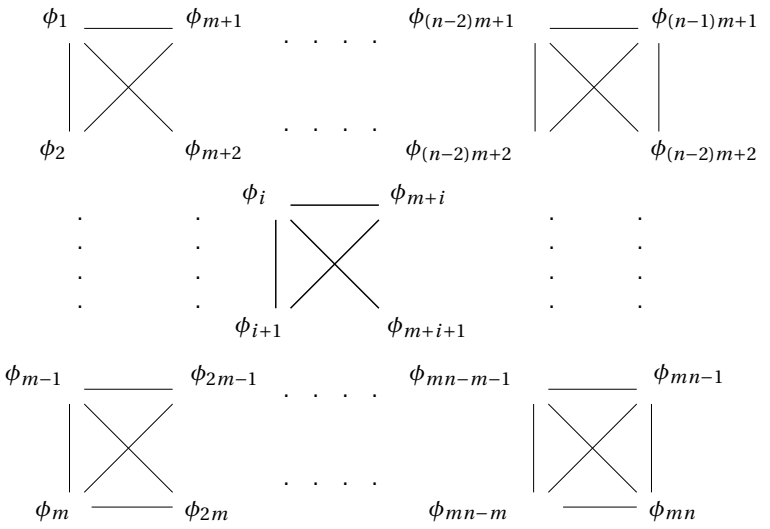

Figure 4.1: Relative phase over a two-dimensional aperture containing $m \times n$ elements. The figure represents the mapping of the relative phase ϕ_k at a particular grid point to element k in a vector ϕ. With the exception of the right and bottom edges, all available phase differences are included by repeating the same basic cell pattern. The result is therefore a matrix formulation of the relative phase retrieval problem, in which the matrix is almost banded.

Consider now the phase estimated in a frequency band (a, b). Let $\{\psi_k(\omega)\}_{k=0}^{\infty}$ be a basis for $L^2(a, b)$. In this basis, the relative phase may be written as

$$\phi(\omega) = \sum_{k=0}^{\infty} \langle \phi, \psi_k \rangle \psi_k(\omega).$$

Equation (4.5), therefore, becomes

$$\sum_{k=1}^{\infty} A\langle \phi, \psi_k \rangle \psi_k(\omega) = \theta(\omega),$$

where the matrix A is the same as in Eq. (4.5), and

$$\langle \phi, \psi_k \rangle = \left[\langle \phi_1, \psi_k \rangle, \langle \phi_1, \psi_k \rangle, ... \langle \phi_{MN}, \psi_k \rangle \right]^T.$$

Taking the inner product with ψ_n, the resulting equation

$$A\langle \phi, \psi_n \rangle = \langle \theta, \psi_n \rangle,$$

is the same as Eq. (4.5), but for each coefficient instead of for each frequency. Using a reduced set of appropriately smooth basis functions, therefore, preserves the smoothness across frequencies.

This procedure is seen to be equivalent to obtaining the least-mean-square-error solution for each frequency separately, and then projecting this onto the same reduced set of basis functions. However, from a computational point of view, doing the projection first is advantageous, because this greatly reduces the number of unknowns. It may also be of interest to use a different number of coefficients, or even a different set of basis functions, for different parts of the transducer. In this case, the equivalence between projection before and after finding the least-mean-square-error solution disappears.

Stability

Since the stability of the relative phase retrieval algorithm based on coefficients in the orthogonal expansion is the same as the stability of Eq. (4.5), only the latter is treated here.

Let $\hat{\theta}(\omega) = \theta(\omega) + \epsilon(\omega)$, where $\epsilon(\omega)$ is a zero-mean random vector representing additive noise. Assuming $\epsilon(\omega)$ has the covariance matrix

$$C_\epsilon(\omega) = \mathrm{E}\left[\epsilon\epsilon^H\right],$$

the estimate is $\hat{\phi}(\omega) = \phi(\omega) + \nu(\omega)$ in which $\nu(\omega)$ is a zero-mean random vector representing the noise. The covariance matrix of the estimation noise is

$$C_\nu(\omega) = \mathrm{E}\left[\nu\nu^H\right] = A^\dagger C(\omega)(A^\dagger)^H,$$

where $A^\dagger = V\Sigma^+ U^H$. Let the noise ϵ be white with variance σ^2. Then $C(\omega) = \sigma^2 I$, and

$$C_\nu(\omega) = \sigma^2 V|\Sigma^+|^2 V^H.$$

Consider an aperture with $m = n$, *i.e.*, a transducer with n^2 transducer elements. The maximum value of any element on the diagonal of $C_\nu(\omega)$ is a bound for the variance of the error in the estimated relative phase. As can be readily seen from Fig. 4.2, the error in the cross-spectrum phase estimate is not significantly amplified when retrieving the relative phase. However, the relative phase estimation noise is no longer white, as the covariance matrix $C_\nu(\omega)$ is not diagonal. Error in the phase estimates can, therefore, have long-range effects on the estimate of the relative phase.

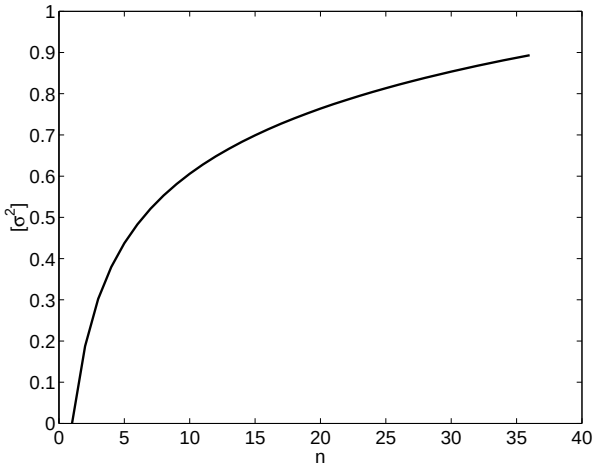

Figure 4.2: A bound for the variance for the estimated relative phase. The estimate is based on relative phase differences with additive white noise of variance σ^2.

III Method

III.A Correlation

Because the effective diameter of the beam used in this study is comparable to the separation between foci, the effective scattering volumes overlap. Hence, different measurements in each data set were correlated. This correlation was estimated using the auto-correlation between two measurements for each transducer element. The average of this auto-correlation is a measure of the correlation between the data sets.

Let $X_k(t)$ and $X_n(t)$ be two stochastic variables representing two different measurements from the same transducer element. If the processes $X_k(t)$ and $X_n(t)$ are ergodic and have zero mean, the correlation between the two measurements may be estimated as

$$\hat{C}(s) = \frac{\sum_{j=1}^{N} X_k(t_j)\overline{X_n(t_j - s)}}{\sqrt{\sum_{j=1}^{N} |X_k(t_j)|^2 \sum_{j=1}^{N} |X_n(t_j)|^2}},$$

where the realisations of the measurements are sampled at points $\{t_j\}_{j=1}^{N}$. Now, $\hat{C}(0)$ is an estimate for the correlation between the two measurements.

III.B Window selection

The choice of window function λ for the Blackman-Tukey estimator is not obvious. A rule of thumb used here is that the window function should not significantly distort the central part of the covariance function. This, in turn, implies restricting the bandwidth of the window to be less than the bandwidth of the spectrum to be estimated.

The spectrum to be estimated is smooth and continuous and does not contain spectral lines. Blurring of spectral lines is, therefore, not an issue. Since the correlation length of the random scatterers is assumed to be very short, a natural conclusion is that the correlation length of the received signal should be about the same as the pulse length. This is based on the independence of scattering from non-overlapping regions in the random medium.

Also to be considered is the implementation of the Blackman-Tukey estimator. Using a window function that is rectangular in the frequency domain gives the Daniell estimator[20] [Ch. 2], also known as a *smoothed periodogram*. This is implemented most efficiently using one FFT and a relatively short sliding average. A Parzen window[19] [Section 6.2.4] is most efficiently implemented using three FFTs; one to compute the periodogram, and two to perform the convolution with the frequency domain representation of the window function.

The Parzen window is used in this study due to its sharp cut-off of the covariance function beyond the correlation length. However, if efficiency is an issue, a window with a narrow support in the frequency domain, like the Daniell estimator, would be preferable.

III.C Construction of basis functions

An "optimal" set of basis functions for representing the true phase of aberration could be constructed by performing a singular-value decomposition of a matrix containing the true aberration over the aperture as a function of frequency. Here, *optimal* is taken to mean that only a few significant coefficients are needed to give a good representation. This basis, however, would be dependent on the particular aberration, and would not necessarily be optimal for a different aberration. To handle the variations in aberration found in ultrasonic imaging, a basis independent of the particular aberration is required.

Not much is known about the frequency-dependence of aberration found in ultrasound imaging, but physical reasoning suggests that the aberration should be smooth. The basis functions should, therefore, also be smooth. Furthermore, most of the phase aberration is accounted for by a time-delay. Since this is represented by a linear function of frequency, and a constant phase is unimportant in this context, $\psi(f) = f$ is chosen as the first basis function.

Also, the phase estimates are most reliable closer to the centre frequency f_0. This is due to a much higher signal-to-noise ratio close to f_0 than further away. A weighted inner product that emphasises this region when defining orthogonality of the basis functions is, therefore, employed. The following inner product, which uses a weightfunction to accentuate a band slightly narrower than the bandwidth of the transmit pulse was found to give good results.

$$\langle u, v\rangle = \int_0^{3f_0/2} w(f)\, u(f)\, \overline{v(f)}\, \mathrm{d}f,$$
$$w(f) = f^5 \exp\left(-\left[2/5 + f/f_0\right]\right)^6.$$

The weightfunction $w(f)$ is plotted in Fig. 4.3.

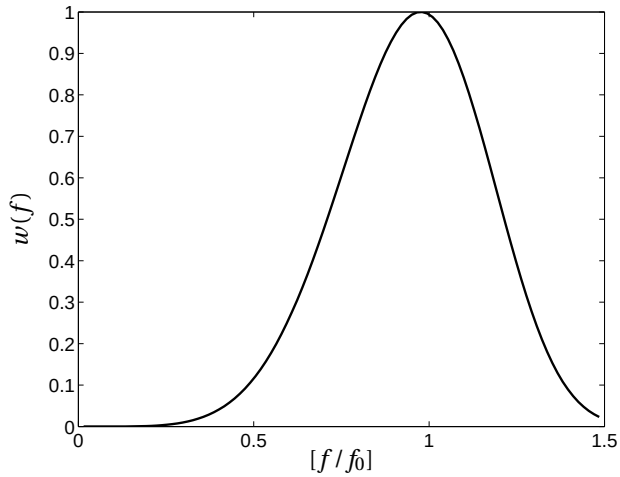

Figure 4.3: Weightfunction for the inner product which was used to construct the orthogonal basis functions.

An orthogonal set of n polynomials is constructed from this inner product using the Gram-Schmidt algorithm on the set of functions $\{f, f^2, f^3 \ldots f^{n-1}, 1\}$ in that order. By construction, the basis functions are smooth, and the first coefficient in the orthogonal expansion using this basis corresponds directly to a physical time-delay. Other coefficients correspond to higher-order polynomial corrections to the time-delay. Thus, the higher-order correction terms, give an indication of the need to consider phase variations beyond a time-delay.

III.D Inactive transducer elements

The transducer is known to have some bad elements, *i.e.*, elements that do not behave the way they should. These have a different bandpass or sensitivity than the rest of the transducer elements in the array. Since additive noise in the measurements can have long-range effects on the algorithm for finding the relative phase, bad elements are identified and removed from the processing.

The bad elements were identified during calibration of the 2D array system. Measurements from these elements were replaced by substituting the average of eight neighbouring transducer elements.

To deal with remaining outliers in the dataset, a robust implementation of the relative phase retrieval was used.[22] The procedure was as follows:

1. An initial least-mean-square-error estimate for the relative phase was calculated from

$$\phi^{(0)}(\omega) = A^{\dagger}\theta(\omega).$$

2. A weight matrix W^0 was calculated using

$$\mu = \mu(\omega) = \frac{1}{L}||A\phi(\omega) - \theta(\omega)||_1$$
$$\left(W^0\right)_{i,j} = \delta_{ij} \exp\left(-\left|\phi^{(0)}(\omega)_i - \theta(\omega)_i\right|^2 / 4\mu^2\right).$$

3. A new least-mean-square-error estimate $\phi^{(1)}(\omega)$ was obtained from the inner product

$$\langle x, y\rangle_{W^0} = y^H W^0 x.$$

   (Assuming outliers do not corrupt the initial estimate too badly, this estimate is less influenced by outliers than the first one.)

4. Steps 2 and 3 were repeated three times to get the final estimate $\phi^{(3)}(\omega)$, which is taken to be the relative phase over the transducer.

The stability of this algorithm is difficult to examine exactly due to its nonlinear nature. However, as long as the dataset does not contain too many outliers, the estimator behaves approximately in a linear fashion. Moreover, in the application of the algorithm, the estimate did not seem to change much from the second to the third iteration, indicating convergence for the measurements presented here.

III.E Validation of estimates

Accuracy of the spectral estimates can be validated by constructing confidence intervals at each frequency for the phase and amplitude of the spectral estimates. However, motivation for the estimation is the desire to perform aberration correction. It is, therefore, of greater interest to compare the characterisation based on the cross-spectral estimates to an ideal aberration correction filter.

A reference characterisation was obtained as follows: the random scatterer distribution was replaced by a point-like reflector that was the rounded tip of a rod. The reflector was, in turn, placed at each of the focal positions of the random scattering measurements in order to obtain samples of the aberrated point scattering at each location. From these signals, a reference spectrum was created. Care was taken to apply the same spectral smoothing as introduced by the window in the spectral estimation, thus ensuring the minimum bandwidth for the two spectra was the same.

The point source scattering process is deterministic. Thus, the only stochastic element present in obtaining the reference characterisation is measurement error. This is negligible for the current study. The reference may therefore be viewed as a deterministic quantity. Also, a low variation in the reference spectrum from focal point to focal point indicates that the isoplanatic hypothesis is valid.

From the reference spectrum, a reference for the relative phase of aberration and magnitude of aberration was constructed by the same method as for the estimated spectrum.

$$s_{\text{ref}}(r,\omega) = A_{\text{ref}}(r)\, e^{i\theta_{\text{ref}}(r,\omega)}.$$

The quantity s_{ref} is the generalised screen for focusing at r_f, but weighted by a system response as seen in Eq. (4.3). For a point reflector, however, the system response is merely the square of the amplitude of the transmit pulse, and hence the same across the aperture. Therefore, s_{ref} corresponds, as shown in simulations,[6] to an ideal aberration correction filter. Agreement between the estimated aberration characterisation and this reference, thus, implies aberration correction properties for the estimated characterisation.

In order to quantify the difference between the relative phase and the reference, a root-mean-square-difference (RMSD) was calculated after subtracting the mean difference. This allows the relative phase estimate to differ from the reference by an unimportant arbitrary constant phase factor.

For the estimated magnitude of aberration to be comparable to the reference, the power should be the same in both. Both the reference and the estimate were, therefore, normalised. The difference was then measured using the L^2-norm.

Table 4.1: Important quantities for this study.

Transmit pulse	
frequency	3 MHz
pulse length	1.5 µ
bandwidth	53%
Aberrator (mab)	
arrival time fluctuations	65 ns
arrival time corr. length	8.2 mm
energy level fluctuations	2.7 dB
energy level corr. length	2.7 mm
Aberrator (sab)	
arrival time fluctuations	65.3 ns
arrival time corr. length	5.4 mm
energy level fluctuations	3.1 dB
energy level corr. length	1.5 mm
Measurements	
focal zone radius	0.45 mm
sample range	3.00 mm
sampling frequency	20 MHz
focal range	~ 55 mm
f-number	~ 1.2

IV Measurements

The measurements used in this study were performed using an 80×80-element 2D transducer array with 0.6 mm pitch, centre frequency 3 MHz, and a sampling rate of 20 MHz. The relevant f-number was approximately 1.2. The length of the transmitted pulse was approximately 1.5 µs, with a 53%bandwidth.

The transducer array emitted an ultrasound pulse wavefront that focused at a spatial location corresponding to a vertex or the centre of an icosahedron of radius r. The scattering region was a tissue-mimicking phantom. The correlation length of this scattering region is known to be short relative to the wavelength. Hence, the scatterers were assumed to be δ-correlated. To obtain the reference characterisation of the aberration, the sequence of measurements was repeated after replacing the scattering phantom by the rounded tip of a rod with a diameter of 0.82 mm.

A dataset consisted of 13 measurements, one for each of the 12 vertices and one for the centre of the icosahedron, or a set of 75 measurements. In the set of 75 measurements, the focus was placed at the centre and the 12 vertices of an inner icosahedron, the 20 vertices of an enclosing dodecahedron, the 12 vertices of an outer icosahedron, and the midpoints of the 30 circular arcs that connect adjacent vertices of the outer icosahedron. The polyhedra had a common centre and were configured with each vertex of the dodecahedron located along a ray from the origin through the centre of one of the faces of the icosahedra while each vertex of the icosahedra was located along a ray from the origin through the centre of one of the faces of the dodecahedron. The icosahedra were spatially oriented so one axis that passed through two vertices and the common centre was normal to the plane of the transducer array at its centre. From the common centre, the distance to the vertices of the inner icosahedron, dodecahedron, and outer icosahedron were 0.79, 1.50, and 1.50 mm, respectively.

Aberration mimicking the distortion produced by an abdominal wall was introduced by placing a specially-designed phantom[23] between the transducer and the scattering region. The phantom was either a *medium aberrator* (mab) or a *strong aberrator* (sab). For these phantoms, the isoplanatic patch is known to be large enough to contain all focal positions used in the study. Table 4.1 summarises relevant measurement information.

The 13 measurements in a dataset were numbered from 0 to 12. The labelling reflected the corresponding icosahedron vertices in Fig. 4.4.

The effective radius of the focal zone at a relative amplitude of $1/\sqrt{e}$ was 0.45 mm. An 80-sample interval that corresponds to a range of 3.00 mm at the 20 MHz sampling rate of the 2D array system was used in the processing.

A total of 22 transducer elements were identified as bad during the calibration process. These were effectively removed from the datasets as described in Sec. III.D. This was performed prior to any other processing.

V Results

The average correlations between measurement 0 and each of the measurements 1 to 12 in the datasets are listed in Table 4.2 for icosahedra with three different radii. The correlation in the data set with 0.50 mm radius icosahedron is clearly higher than that of the dataset with the same aberrator and 1.00 mm focal-point separation. Moreover, measurements from focal points with 1.00 mm separation are relatively uncorrelated. Averaging n spectral estimates from different measurements in this dataset will, therefore, reduce the estimate variance by a factor of close to n. Measurements on the dataset with 0.79 mm focal-point separation are also sufficiently uncorrelated for this to be the case. The true variance reduction when averaging n spectral estimates

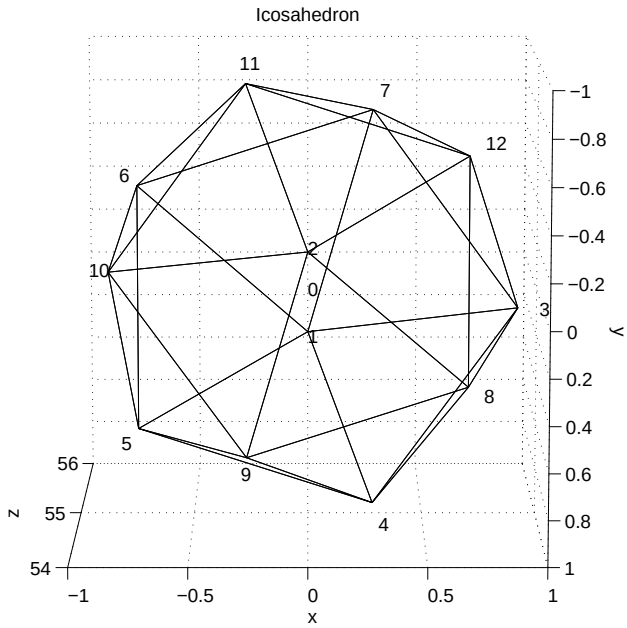

Figure 4.4: Labelling of the vertices of the icosahedron used for focusing.

from the dataset with 0.50 mm separation is expected to be much less than n due to the significantly higher correlation.

Only the results from estimating spectra using measurements inthe dataset with 0.79 mm focal point separation are presented in detail.

A Parzen window was employed in the Blackman-Tukey estimator. The measurement sampling frequency of 20 MHz and a pulse length of 1.5 µs for the transmitted pulse indicate that the scaling factor M should be chosen such that the window does not distort the covariance function significantly for lags less than 30 samples. The value of M was, therefore, chosen to be 50 for the Parzen window.

Figure 4.5 shows the estimated power spectrum for eight transducer elements surrounding the centre element. The 95% confidence intervals are approximately ±2 dB wide for this estimate. A normalisation was chosen such that the corresponding auto-correlation functions are 1 for zero lag. The square root of this quantity is an estimate for the magnitude of aberration.

The phase of the estimated cross-spectrum between the centre element and each of its eight neighbours is plotted in Fig. 4.6. In this case, the 95% confidence intervals are about ±15° wide. These phases are the relative phase differences from which the

Table 4.2: Correlation between different measurements. These are values for the correlation $\hat{C}(0)$ between the measurement labelled $k = 0$ and different measurements n in the same dataset. The presented values were calculated as an average over a 20×20 neighbourhood of the centre transducer element. Mean values for the correlation in the 0.50 mm, 1.00 mm and 0.79 mm case are 0.31, 0.03 and 0.00, respectively.

n	$\hat{C}(0)$ ($r = 0.5$ mm) (mab)	$\hat{C}(0)$ ($r = 1.0$ mm) (mab)	$\hat{C}(0)$ ($r = 0.79$ mm) (sab)
1	0.31	0.07	0.24
2	0.19	0.10	0.16
3	0.03	-0.22	0.12
4	0.38	-0.08	-0.09
5	0.35	0.12	-0.20
6	0.04	-0.00	-0.02
7	0.39	0.06	-0.04
8	0.48	0.23	-0.01
9	0.44	-0.09	0.07
10	0.31	-0.02	-0.01
11	0.23	0.06	0.09
12	0.52	0.18	0.19

relative phase across the transducer is to be recovered.

A comparison between the estimate and the point source reference for the amplitude and the phase of aberration is presented in Fig. 4.7. Recovery of the relative phase was performed for each frequency separately, thus not utilising the spectral smoothness inherent in the spectral phase estimate. The reference magnitude obtained from the point reflector has been normalised to account for the energy difference in the scattering from point reflector and stochastic medium.

In order to preserve the smoothness of the phase, the orthogonal expansion technique discussed in Sec. II.C and the basis functions discussed in Sec. III.C were used. The resulting first six coefficients of this expansion are shown in Fig. 4.8. Visual inspection reveals that all of these six coefficients exhibit reasonable spatial structure for the reference. The coefficients for the estimate, however, only display obviously similar spatial structure in the first coefficient, and to a lesser extent in the second. The lack of spatial structure in the estimated coefficients beyond the first two indicates that they consist mainly of noise, although there is still a vague structure similar to that of the reference in higher coefficients as well.

In Fig. 4.9, the relative phase has been reconstructed using the first two coeffi-

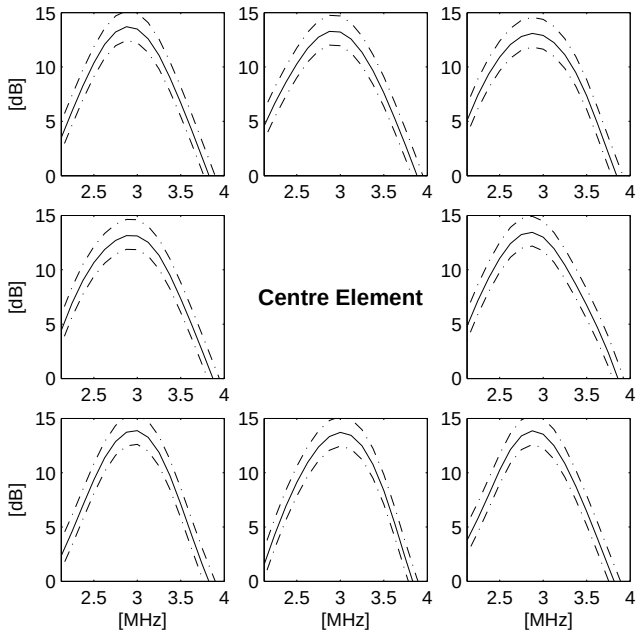

Figure 4.5: Magnitude of estimated cross-spectrum for the backscatter received at eight transducer elements surrounding the centre element. The dash-dot line corresponds to a 95% confidence interval.

cients in the orthogonal expansion of the phase. The magnitude of aberration has been adjusted separately for each frequency to account for some of the difference in system response between point reflector and stochastic medium.

In light of the confidence bands for the amplitude and phase estimates in Figs. 4.5 and 4.6, the dataset was augmented to contain 75 measurements with focal points distributed as described in Sec. IV. Estimated power spectrum and cross-spectral phase for this dataset are plotted in Figs. 4.10 and 4.11. In this case, confidence bands for the power spectra are about 1 dB wide, while confidence bands for the cross-spectral phase are about $\pm 5^\circ$. The associated coefficients and final aberration characterisation are plotted in Figs. 4.12 and 4.13, respectively.

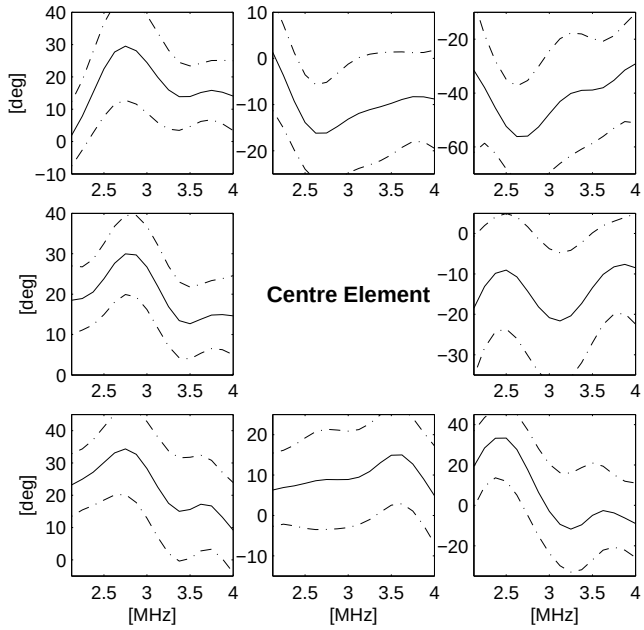

Figure 4.6: Phase of the estimated cross-spectra between the centre transducer element and each of the surrounding eight elements. The dash-dot line corresponds to a 95% confidence interval.

VI Discussion

The data in Table 4.2 show that 0.50 mm focal-point separation is not enough to obtain an independent set of measurements for this experimental configuration. Using a 0.79 mm or 1.00 mm radius icosahedron to place the focal points, however, does appear to give independent samples. This is in agreement with the predicted size of the focal region in Sec. IV. The conclusion is also supported by the fact that no significant improvement was observed when combining the 0.50 mm and the 1.00 mm datasets to obtain an aggregate estimate. This demonstrates the necessity of separating the focal points for different measurements to aquire statistically independent samples.

The confidence bands are appreciable for both the estimated cross-spectrum phase and amplitude when using a dataset of 13 measurements. The estimation variance could be reduced by choosing a smaller parameter M, but at the expense of increased estimation bias and blurring of the spectral estimate. Increasing the

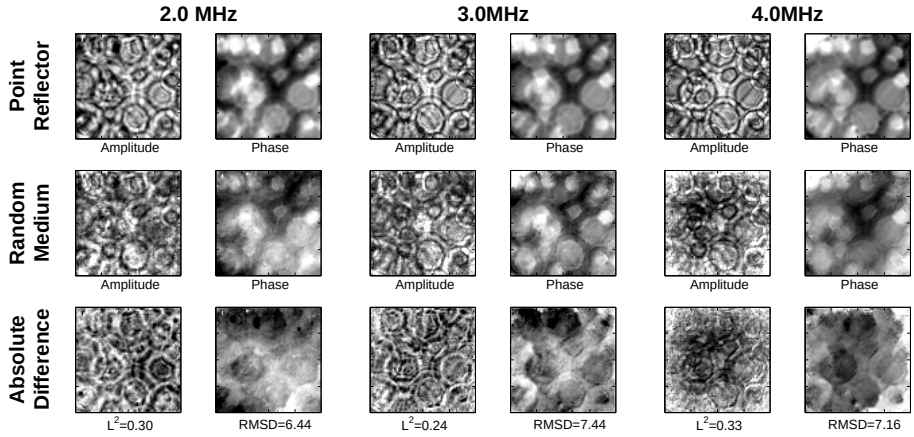

Figure 4.7: Magnitude and relative phase of aberration recovered from the estimated cross-spectra. The magnitude has been adjusted by a constant factor to compensate for the energy difference between point reflector data and stochastic data. The RMSD is expressed in units of degrees.

sample length would also seemingly reduce the variance. However, the stationarity assumption about the received scattering can only be expected to hold locally, *i.e.*, within the depth of field. Furthermore, increasing the sample length would lead to a significant overlap of the scattering regions in the depth direction, thus increasing the correlation between the samples. A better solution to reduce the estimation variance is to increase the number of measurements in the dataset. Indeed, using an augmented dataset consisting of 75 measurements gives significantly improved spectral estimates as shown in Figs. 4.10 and 4.11. In the situation of interest, however, the possibility of increasing the number of measurements is fundamentally limited by the size of the isoplanatic region. When moving out of the isoplanatic region, the phase and amplitude of aberration will gradually change. Averaging measurements outside this region will, therefore, give a blurred estimate.

Despite the wide confidence bands for the spectral estimates in Figs. 4.5 and 4.6, the magnitude and relative phase of aberration obtained from the estimated spectra have the same spatial structure observed in the reference solution seen in Fig. 4.7. The similarity is quantified by the L^2 norm and RMSD given in the figure.

Projecting the relative phase onto the first two basis functions improves the phase retrieval as shown clearly by comparison of Figs. 4.7 and 4.9. However, the data in Fig. 4.8 also show that the spectral estimates obtained from 13 measurements are not good enough to warrant looking for more than two coefficients in this expansion,

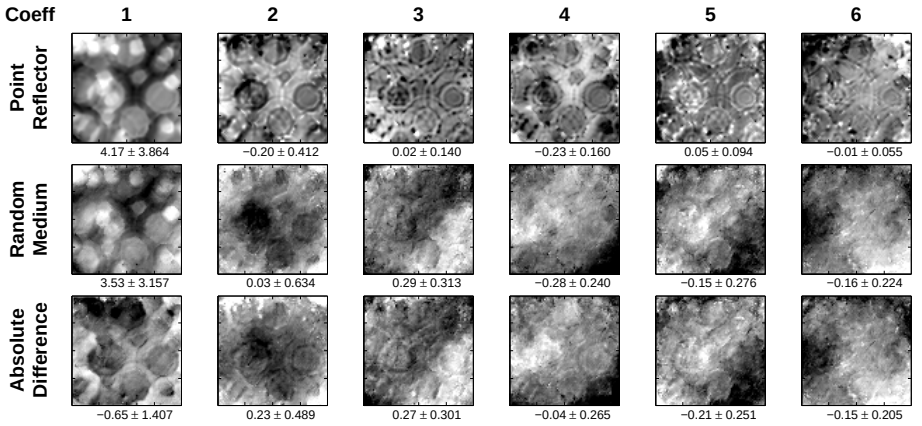

Figure 4.8: Coefficients in an orthogonal expansion of the relative phase. Mean value and standard deviation are indicated below each panel.

i.e., classical time-delay with a second-order correction term. For 75 measurements, the estimates are improved as seen in Figs. 4.10-4.13. However, the higher-order correction coefficients still contain limited information. (See Fig. 4.12.) This indicates that classical time-delay is a good approximation of the frequency-dependent phase in the measurements reported here.

For the case with 13 measurements, the RMSD for the relative phase is approximately half the width of the confidence bands. (See Figs. 4.6 and 4.7.) Approximately four relative phase estimates were used to obtain the least-mean-square-error estimate of the phase at each point. A reduction of the error by a factor of 2 is therefore optimal, and indicates that the error in each of the relative phase estimates is independent.

For the case with 75 measurements, the error is not reduced significantly compared to the width of the confidence bands. The quantitative measure of improvement is, in fact, not as good as one would expect when going from 13 to 75 measurements. (See Figs. 4.10-4.13.) The reason is that the aberration from the random scatterers is smoothed out. The difference between the reference and the estimate clearly shows that the main deviations are found around the edges of spatial structures; an indication of blurring. This is a deviation that grows as more measurements from a larger region are used, as the isoplanatic assumption is gradually invalidated. The same trend is visible for the amplitude estimates. A simple spatial blur of the reference amplitude or phase, *e.g.*, averaging over a 3×3 neighbourhood of each point, reduces the difference between the reference and the

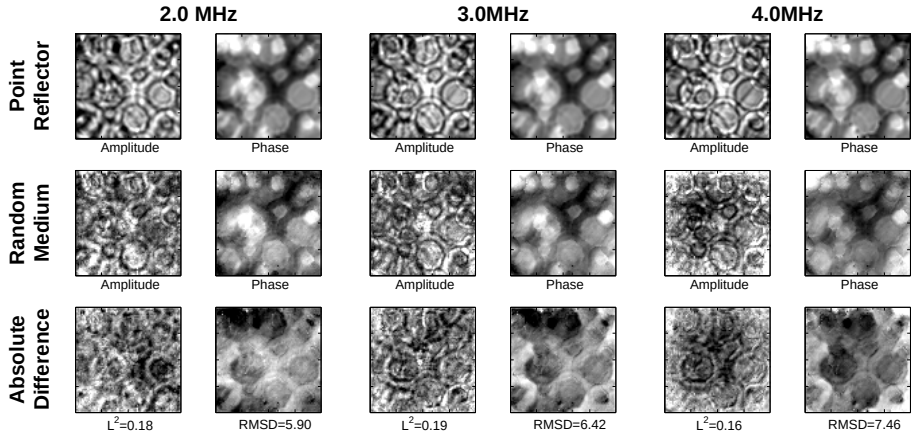

Figure 4.9: Magnitude and relative phase of aberration. The phase has been recovered from the estimated cross-spectra using an orthogonal expansion. The magnitude determined from the point reflector has been adjusted separately by multiplicative constant for each frequency. The RMSD is expressed in units of degrees.

estimate. This also supports the conclusion that a spatial blurring is taking place.

A major part of the RMSD is due to the spatial blurring. (See Figs. 4.7 and 4.13.) Another reason for the estimate to differ from the reference is that the system response is different for scattering from the random medium and scattering from the point reflector. According to Eq. (4.3), the relative phase reconstructed from phase differences from the cross-spectrum will also contain the phase of the system function $P^{(h)}$. The same is true for the magnitude. A better estimate would therefore be obtained if the system response could be identified and removed.

The choice of window function and orthogonal basis functions here is not based on an optimality criterion. Indeed, such an optimality criterion would be difficult to construct so as to be valid for a wide range of aberration cases. Thus an alternate choice will certainly result in different performance. The choice was based on a plausibility rationale, and serve to illustrate features that the window function and basis functions should possess. Also, the presented basis functions were able to describe the true aberration with almost as few significant coefficients as a basis obtained using a singular-value decomposition of the aberration. Therefore, it should not be a bad choice.

An important issue with the spectral estimation is that the coherence in the received signals is low (~ 0.6) for the aberrated signal. It can be shown that, assuming the aberration is well described by a screen model, the coherence is determined by

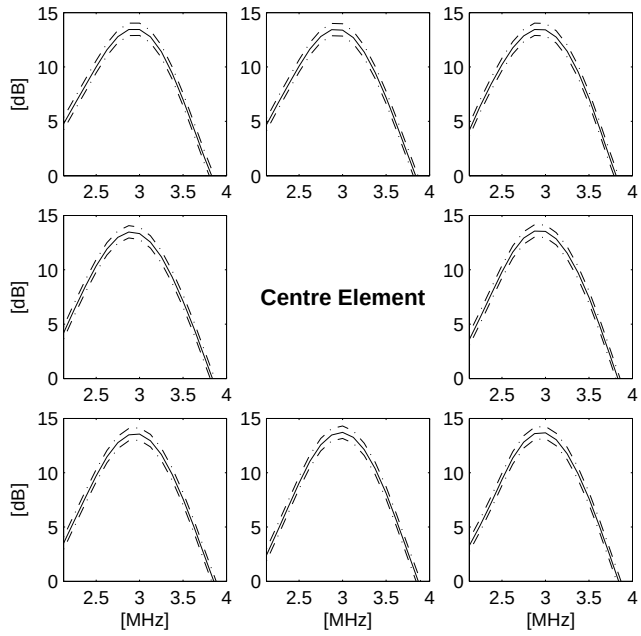

Figure 4.10: Magnitude of estimated cross-spectrum for the backscatter based on 75 measurements, with corresponding 95% confidence interval.

the aberration on transmit, and not on receive.[15] Therefore, if a limited correction of the aberration is to be obtained, the coherence will also improve, resulting in better conditions for the spectral estimation. An iterative approach would, therefore, seem natural. It is not clear, however, that an iterated estimate would result in an improved estimate for the situation studied here. The problem is that the scatterers will remain the same, and therefore the measurements will be correlated from one iteration to the next. The way this affects the convergence of the iterated estimate is not obvious.

VII Conclusion

The confidence bands for the presented estimates are appreciable for both the cross-spectrum phase and amplitude when using a dataset of 13 measurements. Despite the wide confidence bands, a good estimate of the time-delay and, to a certain extent, a *second-order correction* has been obtained using the processing and data described here. The magnitude estimate also resolves most of the structure observed in the

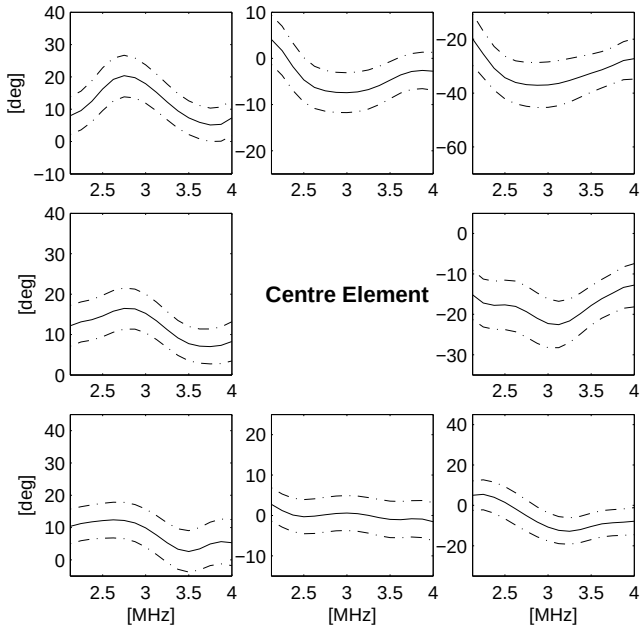

Figure 4.11: Phase of the estimated cross-spectra based on 75 measurements, with corresponding 95% confidence interval.

reference solution, and is in agreement with the reference.

In order to utilise fully the method presented, and use higher-order corrections, an increase in the quality of the phase difference estimate is required. A different choice of window function is worth investigating in order to improve these estimates. However, the best way to improve the estimates is most likely to increase the number of measurements. When doing this, care must be taken not to exceed the isoplanatic region.

Using an augmented dataset consisting of 75 measurements yielded a significant improvement in the spectral estimates. The visual impression of the retrieved magnitude and phase of aberration is also improved. It is, however, difficult to quantify this improvement, as spatial blurring of the estimate seems to dominate the difference between the estimate and the reference. This deviation from the reference will only become more of a problem when the region of measurements is expanded further.

The presented characterisation of the aberration is, nevertheless, well suited for the construction of a filter for the purpose of aberration correction.

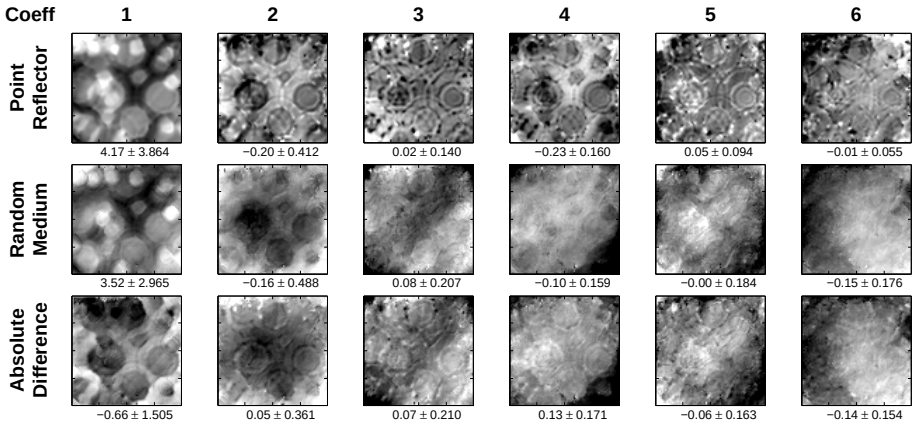

Figure 4.12: Coefficients in an orthogonal expansion of the relative phase based on 75 measurements. Mean value and standard deviation are indicated below each panel.

Acknowledgments

The authors thank Dr. Daniel B. Phillips and Wayne Pilkington for collection of the data used in the processing. Dr. Jeffrey P. Astheimer in the United States and Professor Harald Krogstad at NTNU are thanked for useful discussions. Support for this work was provided by The Research Council of Norway, NIH grants CA74050 and HL50855, and the University of Rochester Diagnostic Ultrasound Research Laboratory Industrial Associates Program.

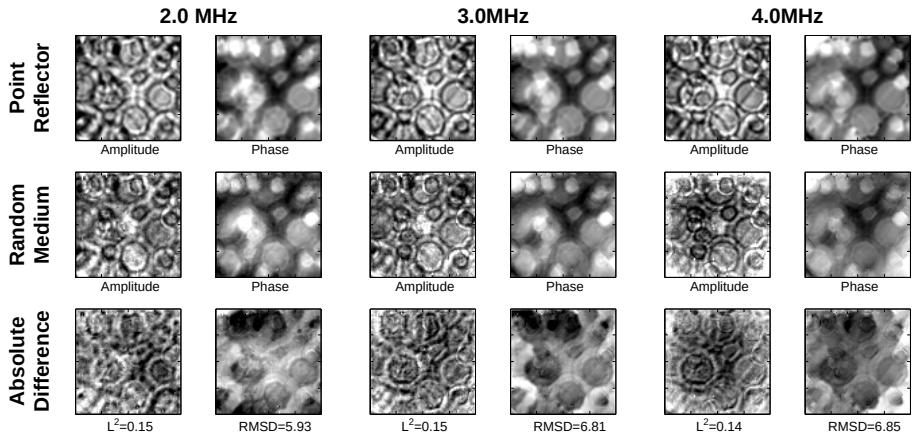

Figure 4.13: Magnitude and relative phase of aberration based on 75 measurements. The phase has been recovered from the estimated cross-spectra using an orthogonal expansion. The magnitude determined from the point reflector has been adjusted by multiplicative constant for each frequency separately. The RMSD is expressed in units of degrees.

References

[1] U. Haberkorn, G. Layer, V. Rudat, I. Zuna, A. Lorenz, and G. van Kaick, "Ultrasound image properties influenced by abdominal wall thickness and composition," *J. Clin. Ultrasound*, vol. 21, pp. 423–429, 1993.

[2] L. Hinkelman, D.-L. Liu, L. A. Metlay, and R. C. Waag, "Measurements of ultrasonic pulse arrival time and energy level variations produced by propagation through abdominal wall," *J. Acoust. Soc. Am.*, vol. 95, no. 1, pp. 530–541, January 1994.

[3] G. E. Trahey, P. D. Freiburger, L. F. Nock, and D. C. Sullivan, "In-vivo measurements of ultrasonic beam distortion in the breast," *Ultrason. Imaging*, vol. 13, no. 1, pp. 71–90, 1991.

[4] P. D. Freiburger, D. Sullivan, B. H. LeBlanc, and G. E. Trahey, "Two-dimensional ultrasonic beam distortion in the breast: in-vivo measurements and effects," *Ultrason. Imaging*, vol. 14, pp. 398–414, 1992.

[5] Q. Zhu and B. D. Steinberg, "Wavefront amplitude distribution in the female breast," *J. Acoust. Soc. Am.*, vol. 96, no. 1, pp. 1–9, April 1994.

[6] S. E. Måsøy, T. F. Johansen, and B. Angelsen, "Correction of ultrasonic wave aberration with a time delay and amplitude filter," *J. Acoust. Soc. Am.*, vol. 113, no. 4, pp. 2009–2020, April 2003.

[7] M. Tabei, T. D. Mast, and R. C. Waag, "Simulation of ultrasonic focus aberration and correction through human tissue," *J. Acoust. Soc. Am.*, vol. 113, no. 2, pp. 1166–1176, February 2003.

[8] D.-L. Liu and R. C. Waag, "Estimation and correction of ultrasonic wavefront distortion using pulse-echo data received in a two-dimensional aperture," *IEEE Trans. Ultrason. Ferroelectr. Freq. Control*, vol. 45, no. 2, pp. 473–490, 1998.

[9] K. W. Rigby, C. L. Chalek, B. H. Haider, R. S. Lewandowski, M. O'Donnell, L. S. Smith, and D. G. Wildes, "Improved in vivo abdominal image quality using real-time estimation and correction of wavefront arrival time errors," in *Proc. 2000 IEEE-UFFC Ultrasonics Symposium*, vol. II, NY, 2000, pp. 1645–1653, IEEE Cat. No. 00CH37121.

[10] M. Fink, "Time reversal of ultrasonic fields - part I: Basic prinsiples," *IEEE Trans. Ultrason. Ferroelectr. Freq. Control*, vol. 39, pp. 555–567, 1992.

[11] M. O'Donnell and S. W. Flax, "Phase-aberration correction using signals from point reflectors and diffuce scatterers: Measurements," *IEEE Trans. Ultrason. Ferroelectr. Freq. Control*, vol. 35, no. 6, pp. 768–774, 1988.

[12] G. C. Ng, S. S. Worrell, P. D. Freiburger, and G. E. Trahey, "A comparative evaluation of several algorithms for phase aberration correction," *IEEE Trans. Ultrason. Ferroelectr. Freq. Control*, vol. 41, no. 5, pp. 631–643, 1994.

[13] D.-L. Liu and R. C. Waag, "Time-shift compensation of ultrasonic pulse focus degradation using least-mean-square-error estimates of arrival time," *J. Acoust. Soc. Am.*, vol. 95, no. 1, pp. 542–555, January 1994.

[14] ——, "Correction of ultrasound wavefront distortion using backpropagation and a reference waveform method for time-shift compensation," *J. Acoust. Soc. Am.*, vol. 96, no. 2, pp. 649–660, August 1994.

[15] B. A. Angelsen, *Ultrasound imaging. Waves, signals and signal processing.* Trondheim, Norway: Emantec, 2000, vol. 2, http://www.ultrasoundbook.com.

[16] F. Lin and R. C. Waag, "Estimation and compensation of ultrasonic wavefront distortion using a blind system identification method," *IEEE Trans. Ultrason. Ferroelectr. Freq. Control*, vol. 49, no. 6, pp. 739–755, 2002.

[17] G. M. Jenkins and D. G. Watts, *Spectral Analysis and its applications.* San Francisco: Holden-Day, 1968.

[18] S. Kay and S. Marple, "Spectrum analysis - a modern perspective," *Proc. IEEE*, vol. 69, no. 11, pp. 1380–1419, January 1981.

[19] M. B. Priestley, *Spectral Analysis and Time Series.* London: Academic Press, 1981.

[20] P. Stoica and R. Moses, *Introduction to Spectral Analysis.* Englewood Cliffs, New Jersey: Prentice Hall, 1997.

[21] D. L. Snyder, *Random Point Processes.* New York: Wiley, 1975.

[22] J. S. Simonoff, *Smoothing Methods in Statistics.* New York: Springer, 1996.

[23] J. C. Lacefield, W. C. Pilkington, and R. C. Waag, "Distributed aberrators for emulation of ultrasonic pulse distortion by abdominal wall," *Acoust. Res. Lett. Online*, vol. 3, no. 2, pp. 47–52, 2002.

Chapter 5

Eigenfunction analysis of acoustic aberration correction

T. Varslot*, E. Mo†, B. Angelsen†, H. Krogstad*
*) Dept. Mathematical Sciences, NTNU
†) Dept. Circulation and Imaging, NTNU

Presented here is a characterisation of aberration in medical ultrasound imaging. The characterisation is optimal in the sense of maximising the expected energy in a modified beamformer output of the received acoustic backscatter. Aberration correction based on this characterisation takes the form of an aberration correction filter. The situation considered is frequently found in applications when imaging organs through a body wall: aberration is introduced in a layer close to the transducer, and acoustic backscatter from a scattering region behind the body wall is measured at the transducer surface. The scattering region consists of scatterers randomly distributed with very short correlation length compared to the acoustic wavelength of the transmit pulse. The scatterer distribution is therefore assumed to be δ-correlated. This paper shows how maximising the expected energy in a modified beamformer output signal naturally leads to eigenfunctions of a Fredholm integral operator, where the associated kernel function is a spatial correlation function of the received stochastic signal. Aberration characterisation and aberration correction are presented for simulated data constructed to mimic aberration introduced by the abdominal wall. The results compare favourably with what is obtainable using data from a simulated point source.

I Introduction

An ultrasound image is formed as a map of the intensity of the reflected sound pulse from different spatial locations. By focusing the transmitted sound pulse at a specific location, the intensity of the transmitted field is highest around the focal point. The reflected signal then originates largely from this region. A limitation is therefore imposed on the image resolution by the size of the focal zone. The smallest obtainable size is limited by diffraction.

In medical ultrasound imaging, the transmitted pulse typically travels through the body wall before arriving at the intended focal point. The body wall consists of a heterogeneous configuration of muscular, fatty and connective tissue. The result of propagation through a medium with variable speed of sound is degradation of the initial geometric focus beam by a widening of the focal zone. The transmitted pulse is then said to be *aberrated*. Experimental studies [1,2,3,4,5] and simulations [6,7] show that this aberration can significantly reduce the image resolution.

Several different approaches have been suggested to reduce the effect of the aberration. These are mostly based on either a time-reversal mirror [8] or a time-delay filter. [9] To use the time-reversal mirror, a well-defined point scatterer is needed in order to focus the signal at a point. This limits its applicability in clinical situations. Time-delay (and amplitude) filters rely on the ability to estimate filter coefficients. When the received signal is from a single, known point reflector, this is mostly a trivial task; time-delay and amplitude fluctuations may be observed directly in the signal. [10] For scattering from a stochastic medium, the filter must be estimated from the stochastic properties of the received signal. If the scattering medium is δ-correlated, the resulting received signal is approximately a Gaussian process. [11] By considering scattering from a limited depth interval, the process may be assumed to be stationary and have zero mean. Since all information about a Gaussian process may be expressed in terms of its mean and its covariance function, it is reasonable to base a characterisation of the aberration on the covariance function. Various algorithms for doing this are available. [12]

This paper considers the characterisation of aberration based on measurements of acoustic backscatter from a stochastic distribution of scatterers, as depicted in Fig. 5.1. The aberration is introduced in a layer close to the transducer and is, therefore, modelled using an infinitesimal aberrating layer on the transducer surface. This layer is called a *generalised frequency-dependent screen* [10,11] or simply a *generalised screen*. The received signal is scattering from a region with δ-correlated scatterers around the focal point. This situation is found in medical imaging applications, *e.g.*, when imaging organs like liver and spleen.

It has been shown that transmitting an eigenfunction of the scattering operator will result in focusing the energy within the support of a deterministic scattering object. [13] The eigenfunctions associated with high eigenvalues will focus on regions

with high scattering intensity. In the case of deterministic, well-separated point scatterers, each with a unique scattering intensity, an eigenfunction of the scattering operator corresponds to a diffraction-limited focusing on one of the scatterers.[13] The corresponding eigenvalue will, in this case, reflect the intensity of the respective point scatterer. Furthermore, it has been shown that under these circumstances, an iterative application of the time-reversal mirror will converge to a diffraction-limited focusing on the point scatterer with strongest intensity.[14]

This paper shows how a similar analysis may be performed on stochastic backscatter signals. The main difference from previous work[13,14] is that the focal region does not contain any distinguished scatterers. However, the initially-transmitted aberrated pulse will have higher amplitude in certain regions, partly due to the geometric focusing and partly due to the aberration. The aberration correction method presented is shown to focus on regions where the initially transmitted pulse has high amplitude. The location of the focal point is, therefore, determined by the aberration. The size of the focal region, however, will be close to that of an unaberrated, diffraction-limited transmit-beam.

The starting point for the aberration characterisation is the intuitive notion of adjusting the receive signal so that, on average, it is as coherent as possible. This leads to a characterisation of the aberration consistent with the generalised screen model.

The paper is organised in the following way. A short review of first-order scattering is given in Sec. II.A. Then a model for the stochastic signal received at the transducer is discussed in Sec. II.B. A formulation for maximising the energy in the received signal is developed in Sec. II.B. The connection between this energy formulation and aberration characterisation is discussed in Sec. II.B. The simulated data are described in Sec. III. Results are presented in Sec. IV. Discussion and concluding remarks are given in Secs. V and VI, respectively.

II Theory

II.A First-order scattering

The theory of first-order scattering is thoroughly covered in the literature,[11,15] and is briefly included here for completeness and to set the notation.

Lagrangian coordinates are particularly well suited for a description of the propagation of an ultrasonic pulse as seen in medical ultrasound imaging.[16] For simplicity, both nonlinear and dissipative terms have been neglected. Conservation of mass, conservation of inertia and a compressibility relation produce a linear wave equation for the Lagrangian pressure.[17]

$$\nabla \cdot \left(\frac{1}{\rho} \nabla p \right) - \kappa \frac{\partial^2 p}{\partial t^2} = 0.$$

Here, $\rho(r)$ and $\kappa(r)$ are the material density and compressibility at equilibrium, *i.e.*, they are not time-dependent. Introduction of an adjusted pressure $\tilde{p} = p/\sqrt{\rho}$ simplifies the equation.[18]

$$\nabla^2 \tilde{p} - \frac{1}{c^2}\frac{\partial^2 \tilde{p}}{\partial t^2} = \Phi \tilde{p}, \tag{5.1}$$

where $\Phi = \sqrt{\rho}\nabla^2\left(1/\sqrt{\rho}\right)$. In the following, the adjusted pressure will be denoted p.

In soft tissue, *e.g.*, muscle, fat and blood, the density and compressibility ranges from 950 to 1070 kg/m^3 and 350 to 500×10^{-12} Pa^{-1} respectively.[16] It is, therefore, appropriate to express the material parameters ρ and κ as

$$\rho(r) = \rho_0 + \gamma\rho_1(r)$$
$$,\kappa(r) = \kappa_0 + \gamma\kappa_1(r),$$

where ρ_0 and κ_0 are constant background values, and ρ_1 and κ_1 represent deviation from these background values with a small non-dimensional factor γ. A reasonable value for γ in this case is 0.1. This suggests looking for a perturbation solution[19] of Eq. (5.1) of the form

$$p(r,t) = p_0(r,t) + \gamma p_1(r,t) + O(\gamma^2).$$

Let $c_1(r)$ be given from

$$\frac{1}{c^2} = \frac{1}{c_0^2} - \gamma\frac{2c_1}{c_0^3},$$

where $1/c_0^2 = \rho_0\kappa_0$. Using this definition $c(r) = c_0 + \gamma c_1(r) + O(\gamma^2)$. Note also that Φ will be $O(\gamma)$. Let therefore $\Phi(r) = \gamma\Phi_1(r)$. Using these definitions, Eq. (5.1) may be written as

$$\nabla^2 p - \frac{1}{c_0^2}\frac{\partial^2 p}{\partial t^2} = \gamma\left(-2\frac{c_1}{c_0^3}\frac{\partial^2 p}{\partial t^2} + \Phi_1 p\right) \tag{5.2}$$

to first order in γ. A perturbation solution is found from

$$\nabla^2 p_0 - \frac{1}{c_0^2}\frac{\partial^2 p_0}{\partial t^2} = 0,$$
$$\nabla^2 p_1 - \frac{1}{c_0^2}\frac{\partial^2 p_1}{\partial t^2} = -2\frac{c_1}{c_0^3}\frac{\partial^2 p_0}{\partial t^2} + \Phi_1 p_0.$$

Now p_0 is the solution of the wave equation in a homogeneous medium, and p_1 represents a first-order correction term introduced by the inhomogeneities, *i.e.*, first-order scattering. When transmitting an initial pulse from the transducer, and receiving the acoustic backscatter from an inhomogeneous medium, the backscatter

will be approximately p_1. This is known as the *Born approximation* of the scattered signal.

In the frequency domain, the problem will be formulated as

$$\nabla^2 \hat{p}_0 + \left(\frac{\omega}{c_0}\right)^2 \hat{p}_0 = 0,$$
$$\nabla^2 \hat{p}_1 + \left(\frac{\omega}{c_0}\right)^2 \hat{p}_1 = \Psi \hat{p}_0.$$

Here

$$\Psi(r,\omega) = 2\frac{c_1(r)}{c_0}\left(\frac{\omega}{c_0}\right)^2 + \Phi_1(r). \tag{5.3}$$

Thus, p_1 on the transducer is found from p_0 by means of the appropriate Green's function[20] g,

$$\hat{p}_1(\xi,\omega) = \int g(\xi - r,\omega)\Psi(r,\omega)\hat{p}_0(r,\omega)\mathrm{d}r. \tag{5.4}$$

Calculations presented in this paper are obtained using the Green's function for the Helmholtz equation in $\mathbb{R}^3$

$$g(r,\omega) = \frac{e^{-i\frac{\omega}{c_0}|r|}}{4\pi|r|}.$$

Throughout this paper, r denotes a coordinate in the scattering region, and ξ is a coordinate on the transducer surface.

II.B Modelling of the received scattered signal

The situation studied here is one where all aberration takes place in a region close to the transducer, while all measured scattering emerges from a region close to the focal point. This is a situation typical for medical ultrasound imaging. The body wall, consisting of a heterogeneous mixture of fat, muscle, and connective tissue, produces considerable distortion of the propagating pulse, while the organs inside the body have very little impact to this effect.[11]

Instead of dealing with ρ_1, κ_1 and c_1 directly, let Ψ be an appropriate scattering distribution. For simplicity, $\Psi(r,\omega)$ is assumed to be a spatial point process for each frequency ω, such that the "covariance function" R_Ψ is proportional to the Dirac δ function,

$$R_\Psi(r_2 - r_1,\omega) = \mathrm{E}\left[\Psi(r_1,\omega)\overline{\Psi(r_2,\omega)}\right]$$
$$= \begin{cases} \sigma_\omega^2 \delta(|r_2 - r_1|), & r_1, r_2 \in \Omega \\ 0, & \text{otherwise} \end{cases}.$$

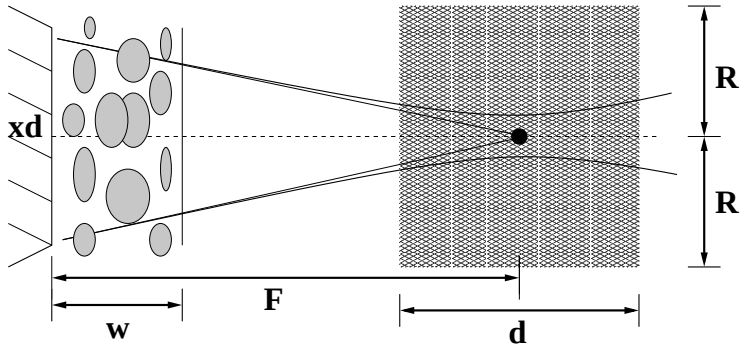

Figure 5.1: Situation of interest. The presented simulation results use a focal depth F of 6 cm, body wall thickness w of 2 cm, and scattering region extending 1.5 cm to either side of the focal point ($d = 3$ cm).

Here $\mathrm{E}[\cdot]$ is the expectation operator, σ_ω^2 is the intensity of the point process[21] at frequency ω, and Ω is the scattering region.

A common assumption is that the aberration introduced by the body wall is the same for all locations within the focal zone. This is valid as long as the focal zone is narrow enough, *i.e.*, located within what is referred to as the isoplanatic patch or region.[11] Using this assumption, propagation through the body wall may be modelled by propagating through a homogeneous medium and then applying a filter. The received signal $\hat{p}_r$ is thus obtained from the scattered signal $\hat{p}_1$ as

$$\hat{p}_r(\xi,\omega) = s(\xi,\omega)\,\hat{p}_1(\xi,\omega).$$

The function s, which accounts for the aberration, is denoted *generalised screen*. The time-reversal argument implies that transmitting a pulse $\hat{p}(\xi,\omega)$ through the aberrating layer, the beam pattern in the focal zone will be as if the pulse $s(\xi,\omega)\,\hat{p}(\xi,\omega)$ were transmitted through a homogeneous medium.

As the aberration is mainly introduced by tissue structures in the body wall, it does not change over the time scale of the imaging process. Therefore, keeping the body wall fixed relative to the transducer, scattering from within a given isoplanatic region will have undergone the same aberration. The function $s(\xi)$ is therefore the same for all realisations.

In the rest of this paper, all computations will be performed in the temporal frequency domain, unless otherwise stated. Explicit dependence of ω in quantities like pressure pulses, screens, and scatterer distributions is therefore omitted. Hence,

the field $\hat{p}_0(r)$, for a transmitted pulse $\hat{p}$, geometrically focused at r_f, is given as

$$\hat{p}_0(r) = \hat{p} \int_T L(\xi) \frac{e^{-i\frac{\omega}{c_0}\left(|r-\xi|+|r_f-\xi|-|r_f|\right)}}{4\pi|r-\xi|} \mathrm{d}\xi,$$

where $L(\xi) = s(\xi)\, l(\xi)$, and $l(\xi)$ is the apodisation function used on transmit. Here T indicates that integration is done over the transducer surface.

Applying the Fraunhofer approximation, valid for large $f$numbers, the transmitted field is given by

$$\hat{p}_0(r) = \hat{p} \frac{e^{-i\frac{\omega}{c_0}|r|}}{4\pi|r|} \hat{L}(\frac{\omega}{c_0} e_r), \tag{5.5}$$

where $e_r = r/|r|$ and $\hat{L}$ denotes the spatial Fourier transform of L obtained when L is extended by zero outside the transducer aperture. The pressure in the far field is, therefore, approximately a spherical wave modified by the Fourier transform of the product of the screen and the transducer apodisation.

The scattered pressure field p_1 at a coordinate ξ on the transducer is now calculated using Eq. (5.4) as

$$\hat{p}_1(\xi) = \int_\Omega \frac{e^{i\frac{\omega}{c_0}|\xi-r|}}{4\pi|\xi-r|} \Psi(r) \hat{p}_0(r) \mathrm{d}r. \tag{5.6}$$

The Fraunhofer approximation then gives the received signal at the transducer surface as

$$\begin{aligned} \hat{p}_r(\xi) = s(\xi) &\frac{e^{i\frac{\omega}{c_0}|\xi-r_f|}}{4\pi|r_f|} \\ &\times \int_\Omega \exp\left(i\frac{\omega}{c_0}\frac{\xi\cdot r}{|r_f|}\right) \Psi(r) \hat{p}_0(r) \mathrm{d}r. \end{aligned}$$

The term $\exp(i\frac{\omega}{c_0}|\xi - r_f|)/4\pi|r_f|$ represents geometric curvature of this signal, and is customarily removed before further processing. The measured signal is thus defined as

$$\hat{p}_m(\xi) = s(\xi) \int_\Omega \exp\left(i\frac{\omega}{c_0}\frac{\xi\cdot r}{|r_f|}\right) \Psi(r) \hat{p}_0(r) \mathrm{d}r.$$

The corresponding (spatial) covariance function for a frequency ω is given as

$$\begin{aligned} R_{\hat{p}_m}(\xi_1,\xi_2) &= \mathrm{E}\left[\hat{p}_m(\xi_1)\overline{\hat{p}_m(\xi_2)}\right] \\ &= s(\xi_1)\overline{s(\xi_2)}\sigma^2 \int_\Omega \exp\left(i\frac{\omega}{c_0}\frac{(\xi_1-\xi_2)\cdot r}{|r_f|}\right)| \\ &\quad \times \hat{p}_0(r)|^2 \mathrm{d}r. \end{aligned} \tag{5.7}$$

Here use has been made of the fact that the scatterer distribution is δ-correlated. Strictly speaking, it is the time-dependent received signal at each transducer element which is a zero-mean Gaussian stochastic process. Thus, Eq. (5.7) is really the cross-spectrum between the received signal at coordinates ξ_1 and ξ_2 as a function of ω. However, for the purpose of this paper, it is more convenient to consider the cross-spectrum as a function of ξ_1 and ξ_2 for a fixed frequency ω. This is therefore denoted the covariance function for the received signal at frequency ω.

Eigenfunction formulation for random signals

Let $\hat{p}_m(\xi)$ be the measured signal at location ξ on the transducer surface. This is now assumed to be a second-order random field (as a function of space for each frequency). Let x be a complex L^2 function with norm 1, and define the stochastic linear functional $\mathscr{L}_x$ as

$$\mathscr{L}_x \hat{p}_m = \langle \hat{p}_m, x \rangle = \int_T \hat{p}_m(\xi)\overline{x(\xi)}\mathrm{d}\xi,$$

where T indicates integration over the transducer aperture. Then

$$\begin{aligned} ||\mathscr{L}_x \hat{p}_m||^2 &\equiv \mathrm{E}\left[\mathscr{L}_x \hat{p}_m \overline{\mathscr{L}_x \hat{p}_m}\right] \\ &= \int_{T^2} \overline{x(\xi_1)} x(\xi_2) \mathrm{E}\left[\hat{p}_m(\xi_1)\overline{\hat{p}_m(\xi_2)}\right] \mathrm{d}\xi_1 \mathrm{d}\xi_2 \\ &= \int_{T^2} \overline{x(\xi_1)} x(\xi_2) R_{\hat{p}_m}(\xi_1, \xi_2) \mathrm{d}\xi_1 \mathrm{d}\xi_2. \end{aligned}$$

Physically, $\mathscr{L}_x \hat{p}_m$ may be interpreted as a *modified beamformer output signal*. The quantity $||\mathscr{L}_x \hat{p}_m||^2$ is the variance of the signal, *i.e.*, the expected energy of the modified beamformer output.

Define the positive semi-definite linear operator A as

$$Ax(\xi) = \int_T R_{\hat{p}_m}(\xi, \xi_2) x(\xi_2) \mathrm{d}\xi_2. \tag{5.8}$$

Now

$$||\mathscr{L}_x \hat{p}_m||^2 = \mathrm{E}\left[|\mathscr{L}_x \hat{p}_m|^2\right] = \langle Ax, x \rangle.$$

The operator A is Hermitian and compact with kernel function $R_{\hat{p}_m}$. Therefore, all eigenvalues are real and non-negative, eigenfunctions belonging to distinct eigenvalues are orthogonal and there exists a largest eigenvalue.[22] It follows that the expected energy of the modified beamformer output signal is maximised when x is an eigenfunction of A associated with the largest eigenvalue.

The eigenvalues and their corresponding eigenfunctions may be ordered according to the magnitude of the eigenvalues. The eigenfunction associated with the largest eigenvalue, denoted λ_1, is then referred to as x_1 and so on.

Focusing properties

In order to investigate further the properties of the eigenfunctions of the operator A defined in Eq. (5.8), consider

$$\langle Ax, x\rangle = \int_{T^2} R_{\hat{p}_m}(\xi_1,\xi_2)x(\xi_2)\overline{x(\xi_1)}\mathrm{d}\xi_2\mathrm{d}\xi_1.$$

Using $R_{\hat{p}_m}$ from Eq. (5.7) and defining $\alpha(r)$ to be

$$\alpha(r) = \int_T s(\xi)\overline{x(\xi)}\exp\left(i\frac{\omega}{c_0}\frac{\xi\cdot r}{|r_f|}\right)\mathrm{d}\xi, \tag{5.9}$$

this may be expressed as

$$\langle Ax, x\rangle = \sigma^2\int_\Omega |\hat{p}_0(r)|^2|\alpha(r)|^2\mathrm{d}r. \tag{5.10}$$

Furthermore, transmitting the pulse $\overline{x(\xi)}\hat{p}$, geometrically focused at r_f, will have the far-field approximation

$$\hat{p}_{\mathrm{cor}}(r) = \hat{p}\frac{e^{-i\frac{\omega}{c_0}|r|}}{4\pi|r|}\alpha(r). \tag{5.11}$$

This expression assumes that no apodisation is used on transmit for the corrected pulse, *i.e.*, $l(\xi) = 1$ when compared to Eq. (5.5). Thus, correcting the transmitted pulse using the eigenfunction x_1 as an aberration correction filter, will focus the transmitted energy according to the initially transmitted field $\hat{p}_0$, in order to maximise Eq. (5.10). Note that there is a separate eigenvalue problem to be solved for each frequency.

Consider first the extreme case when $|\hat{p}_0(r)| = 1$, *i.e.*, the transmitted field insonifies the whole scattering region with equal intensity. Assume also that the scattering region is cylindrical with height d and radius R (see Fig. 5.1). Noting that $\alpha(r)$ is independent of the distance from the transducer along the focal axis, then

$$\begin{aligned}\langle Ax, x\rangle &= \sigma^2\int_\Omega |\alpha(r)|^2\mathrm{d}r \\ &= \sigma^2\int_{T^2} s(\xi_1)\overline{s(\xi_2)}x(\xi_2)\overline{x(\xi_2)}\Lambda\mathrm{d}\xi_1\mathrm{d}\xi_2,\end{aligned}$$

where

$$\Lambda = dR\frac{\mathrm{J}_1(R\omega|\xi_1-\xi_2|/c_0|r_f|)}{\omega|\xi_1-\xi_2|/c_0|r_f|},$$

and J_1 is the Bessel function of first kind. In the current situation $\omega/c_0|r_f| \sim 10^5$. As a consequence of this, $\Lambda \sim \delta(|\xi_1-\xi_2|)$. The largest possible value $\langle Ax, x\rangle$ is therefore

obtained if $|x|^2$ is proportional to $|s|^2$. The amplitude of the eigenfunction x_1 thus matches that of s. A shift of the corrected focus will not influence the eigenvalue, as long as the focus is kept within the scattering region. The phase is therefore not determined.

In the other extreme case, when $p_0(r) = \delta(|r - r_f|)$ is the Dirac δ function, then

$$\begin{aligned}\langle Ax, x\rangle &= \sigma^2 |\alpha(r_f)|^2 \\ &= \sigma^2 \Big| \int_T s(\xi)\overline{x(\xi)}\mathrm{d}\xi \Big|^2.\end{aligned}$$

The maximum for this expression is obtained if x is proportional to s. Thus, the eigenfunction x_1 will be proportional to the screen.

In the general case, which lies somewhere between these two extremes, it is difficult to find a direct relationship between the screen x_1 and s. Let $1/|r|$ be approximated by $1/|r_f|$ in the region where $\hat{p}_0(r)$ is significantly different from zero, *i.e.*, the region which contributes to the integral in Eq. (5.10). Combining Eqns. (5.10) and (5.11) yields

$$\langle Ax, x\rangle \left(\frac{|\hat{p}|}{4\pi |r_f|} \right)^2 = \sigma^2 \int_\Omega |\hat{p}_0(r)|^2 |\hat{p}_{\mathrm{cor}}(r)|^2 \mathrm{d}r.$$

The intensity of the transmit signal using x_1 as a correction filter will, therefore, be focused into areas where the intensity of $p_0(r)$ is high.

It is worth noting that there is an upper bound for the largest eigenvalue since

$$\left(\frac{|\hat{p}|}{4\pi |r_f|} \right)^2 \langle Ax, x\rangle \leq \sigma^2 ||\hat{p}_0||_4^2 ||\hat{p}_{\mathrm{cor}}||_4^2. \tag{5.12}$$

Furthermore,

$$\begin{aligned}||\hat{p}_{\mathrm{cor}}||_4^4 \sim \int_{T^4} &\beta(\xi_1)\overline{\beta(\xi_2)}\beta(\xi_3)\overline{\beta(\xi_4)}\Lambda \\ &\times \mathrm{d}\xi_1 \mathrm{d}\xi_2 \mathrm{d}\xi_3 \mathrm{d}\xi_4,\end{aligned} \tag{5.13}$$

where

$$\begin{aligned}\beta(\xi) &= s(\xi)\overline{x(\xi)}, \\ \Lambda &= dR \frac{\mathrm{J}_1(R\omega|\xi_1 - \xi_2 + \xi_3 - \xi_4|/c_0|r_f|)}{\left(\omega|\xi_1 - \xi_2 - \xi_3 + \xi_4|/c_0|r_f|\right)}.\end{aligned}$$

Again, since $\Lambda \sim \delta(|\xi_1 - \xi_2 + \xi_3 - \xi_4|)$,

$$\begin{aligned}||\hat{p}_{\mathrm{cor}}||_4^4 \sim \int_{T^3} &\beta(\xi_1)\overline{\beta(\xi_2)}\beta(\xi_3)\overline{\beta(\xi_1 - \xi_2 + \xi_3)} \\ &\times \mathrm{d}\xi_1 \mathrm{d}\xi_2 \mathrm{d}\xi_3.\end{aligned}$$

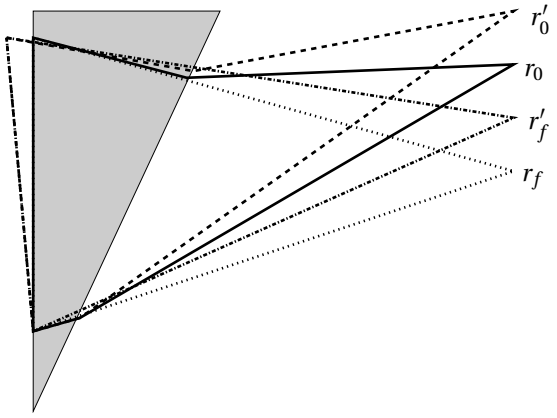

Figure 5.2: The actual focal point is shifted from the intended location r_f to r_0 by a net prism effect in the body wall. Thus, steering the beam towards r_f' will, in reality, steer the beam towards r_0'.

Maximum for $||\hat{p}_{\text{cor}}||_4^2$ is attained when the phase of β is zero, *i.e.*, the phase of x is equal to that of s. Inequality (5.12) is an equality, however, if $|\hat{p}_{\text{cor}}(r)|$ is proportional to $|p_0(r)|$. An iterative correction process is therefore suggested, where the eigenfunction associated with the largest eigenvalue is used to transmit a corrected pulse. The scattering of this corrected transmit pulse has a correlation function which is then used to find a new eigenfunction. No further improvement is possible if Inequality (5.12) is satisfied as an equality, and $||\hat{p}_{\text{cor}}||_4^2$ attains its maximum.

A net prism effect of the body wall manifests itself as a shift of the actual focal point from the intended location of r_f to the location r_0 (see Fig. 5.2). However, as the result of reciprocity, scattering from r_0 will appear as if emerging from r_f, when observed at the transducer.[11] Therefore, scattering from a uniform distribution of scattering will always appear to emerge from a location around r_f. A consequence of this is that observations of the screen s based on such random scattering data do not contain information about the shift from r_f to r_0, *i.e.*, what is observed is not $s(\xi)$ but a different screen $\tilde{s}(\xi)$. The phase of $\tilde{s}(\xi)$ does not contain a linear component as a function of ξ,

$$\int_T \arg\{\tilde{s}(\xi)\}\xi \mathrm{d}\xi = \int_T \arg\{s(\xi)e^{-i\frac{\omega}{c_0}\frac{r_0\cdot\xi}{|r_f|}}\}\xi \mathrm{d}\xi = 0.$$

Using $\tilde{s}(\xi)$ as a correction filter, but adding a steering angle to the transmit-beam in order to move the focus from r_f to r_f', will, in fact, move the focus of the transmit-

beam from r_0 to r_0', where $r_f' - r_f = r_0' - r_0$,

$$\tilde{s}(\xi)\exp\left(i\frac{\omega}{c_0}\frac{(r_f'-r_f)\cdot\xi}{|r_f|}\right) = s(\xi)\exp\left(i\frac{\omega}{c_0}\frac{(r_f'-r_f-r_0)\cdot\xi}{|r_f|}\right).$$

Therefore, a linear term (as a function of ξ) in the phase of the correction filter is connected with a shift of the focal point away from r_0. As there is no way to identify a shift from r_0 to r_f based on the available random scattering data, no distinction will be made here between s and $\tilde{s}$.

Thus far, most of the calculations have been performed assuming everything is within an isoplanatic region. Furthermore, studies have concluded that the isoplanatic assumption is justified in practical situations of interest.[23] The idea of maximising the expected energy of the received signal does make sense also without this assumption. Intuitively, maximising the energy will align the aberrated wavefront, thus countering the aberration experienced in the received signal.

III Method

The simulated ultrasound measurements were created using ABERSIM, a simulation package with routines for simulating forward propagation of an acoustic wave field[24] and aberration of the ultrasonic pulse.[10] In this study, only linear effects without absorption were studied.

A similar theory may be developed using the two-dimensional (2D) Green's function for the Helmholtz equation instead of the 3D Green's function employed here. The fundamental results of Sec. II.B are thus valid also in 2D. In order to reduce the computational requirements, all simulations were conducted in 2D.

A transmit pulse with centre frequency of 2.5 MHz and a geometric focal point at a depth of 6.0 cm was transmitted from a 2.0 cm-wide transducer. The f number for the simulations is therefore approximately 3.0. Aberration was introduced in a 2.0 cm-thick aberrating layer close to the transducer. The acoustic scattering was produced by a $d = 3.0$ cm-thick scattering region. The scattering region extended symmetrically about the focal plane; between ranges 4.5 and 7.5 cm from the transducer. The width of the scattering region was $R = 5$ cm to either side of r_f (see Fig. 5.1). It consisted of a spatially-uniform distribution of point scatterers, approximately 1600 scatterers per square centimetre. Each point scatterer was independently assigned a scattering intensity from a Gaussian distribution. In accordance with Eq. (5.3), the scattering was simulated as proportional to ω^2.

Uncorrelated realisations of the backscatter signal were obtained by replacing the set of point scatterers from one simulation to the next. In order to estimate the required spatial correlation functions, 20 uncorrelated realisations of the acoustic backscatter were used.

Two different aberrators were utilised in this study; a weak aberrator, and a strong aberrator. A detailed description of them is given by Måsøy *et al.*,[10] where they are referred to as w6 and s6 respectively. The weak aberrator produced arrival time fluctuations with an rms value of 49.8 ns and a correlation length of 6.4 mm. The corresponding energy level fluctuations had an rms value of 3.1 dB with a 3.6 mm correlation length. The strong aberrator produced arrival time fluctuations with an rms value of 53.7 ns and a correlation length of 5.8 mm. The corresponding energy level fluctuations had an rms value of 4.1 dB with 1.4 mm correlation length. These aberrators were created to produce aberration exhibiting similar characteristics to that of published measurements. Måsøy showed that almost ideal aberration correction was obtained for both aberrators using a time-delay and amplitude correction filter. This filter was obtained by identifying the wave front from a known point source, and is an approximation of the screen s by making the phase a linear function of frequency.

Since a point source correction filter was found to work well, it was selected as a reference in the current study. However, in order for this to be comparable to a correction filter based on random scattering, the point source was placed in the real focal point of the transmit-beam r_0, and not in the intended focal point r_f. (See the discussion at the end of Sec. II.B.) It further motivates looking for a time-delay and amplitude correction filter only, instead of solving the eigenvalue problems for each frequency and performing aberration correction using a general filter.

IV Results

In the following, eigenvalues and their corresponding eigenfunctions are ordered according to the magnitude of the eigenvalues. The eigenfunction associated with the largest eigenvalue is then referred to as the first eigenfunction, and so on.

A transmit pulse was created being the sum of three pulses u_1, u_2, and u_3. These pulses had focal points r_f, 0.4 mm to the left of r_f, and 0.4 mm to the right of r_f, respectively. No aberration was used for the transmitted beam, thus p_0 consisted of three diffraction-limited lobes with different peak values. Aberration was introduced using the weak aberrator for the scattered signal. The three first eigenfunctions were then used to compute time-delay and amplitude characterisations of the aberration. The time-delay and amplitude screens were used to correct the transmit-signal. Figure 5.3 shows the result with relative transmit amplitudes 1.0, 0.75 and, 0.5 for u_1, u_2, and u_3, respectively. Time-delay and amplitude estimates from the first eigenfunction are very similar to the reference, although an additional apodisation

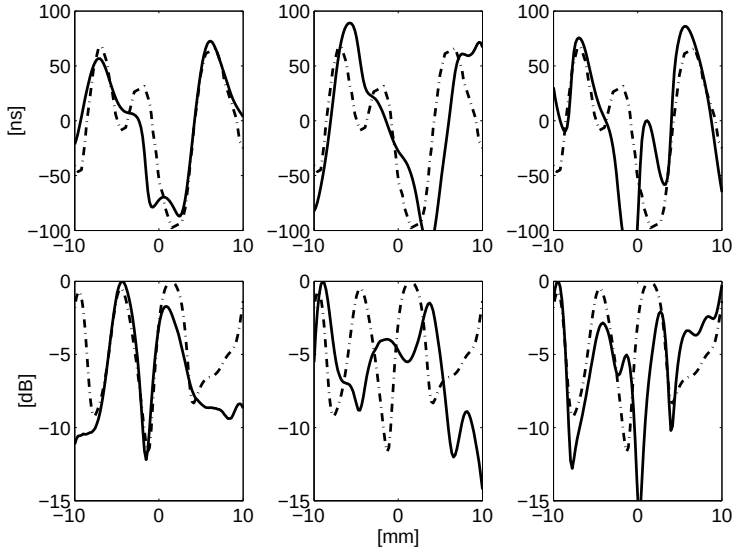

Figure 5.3: Characterisations of the aberration. The transmit pulse had three distinct, diffraction-limited focal points (not aberrated). The acoustic backscatter was aberrated by the weak aberrator. Time-delay and amplitude characterisation was obtained from the covariance function estimated at the centre frequency (solid) and compared to a reference obtained from point source simulations (dash-dot). Top: time-delays estimated from the first, second and third eigenfunction (left to right). Bottom: amplitude fluctuations estimated from the first, second and third eigenfunction (left to right). Relative magnitude of the eigenvalues was: 1, 0.8 and 0.5. A linear term corresponding to a steering of -1.4, -16.5 and 4.9 degrees (left to right) was removed from the time-delays before presentation.

is included in the estimate. The corresponding corrected beam profiles are shown in Fig. 5.4. It is evident that each eigenfunction focuses on a location with high initial transmit amplitude. The strength of these maxima is associated with the respective eigenvalue.

A transmit pulse with a single focal point r_f was then transmitted through the weak aberrator, producing an aberrated beam profile. Figure 5.5 displays the results using the first eigenfunction for correction. Again, as with Eq. (5.10), using the first eigenfunction focuses the transmit signal onto maxima for the amplitude of the initial transmit signal.

Figures 5.6 and 5.7 display the estimation and correction results using a transmit pulse with a single focal point and the strong aberrator on both transmit and receive. In this case, the first eigenfunction does a good job of gathering the beam in a narrow focus, but causes a shifted focal point. However, using the second eigenfunction

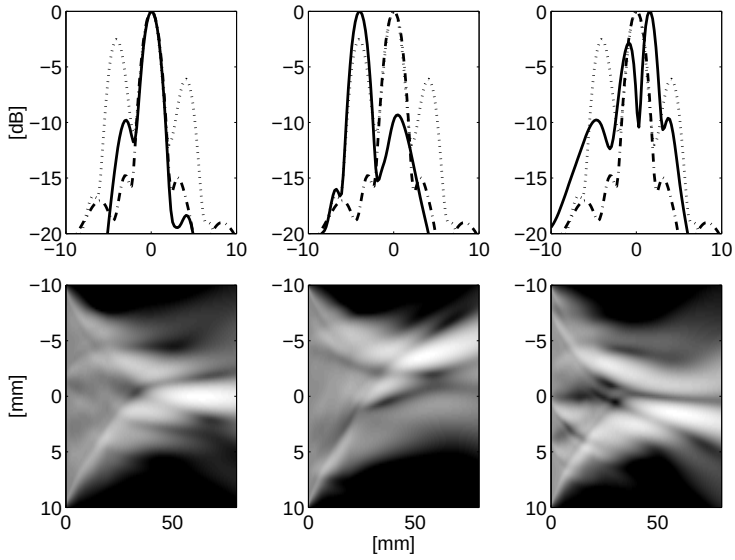

Figure 5.4: Corrected beam profiles. The amplitude and delay screen characterisation of the weak aberrator, presented in Fig. 5.3 was used to transmit a corrected signal through the aberrator. Top: beam profiles in the focal plane. Bottom: corrected beam profiles as a function of depth. The corrected profile (solid) is plotted with the initial transmit pulse beam profile (dotted) and the ideally corrected transmit pulse (dash-dot).

recovers the correct focal point. Note that the linear term in the phase is larger for the first eigenfunction than for the second eigenfunction.

In accordance with the theory, these simulations show that eigenfunctions associated with a reasonably large eigenvalue have focusing properties. Furthermore, the linear contribution to the eigenfunction phase is related to a shift of the focal point relative to the focal point of a transmit-beam with ideal correction.

In order to improve the tightness of the focus while minimising the shift of the focal point caused by the aberration correction, a modification of the iterative approach would be to choose among the eigenfunctions associated with reasonably large eigenvalues, the one with the smallest linear contribution to the phase. Iteration should be repeated until one eigenvalue is dominant.

Figure 5.8 shows how consistently choosing the eigenfunction associated with a large eigenvalue, but with the smallest linear term in the screen phase, will result in improved focusing.

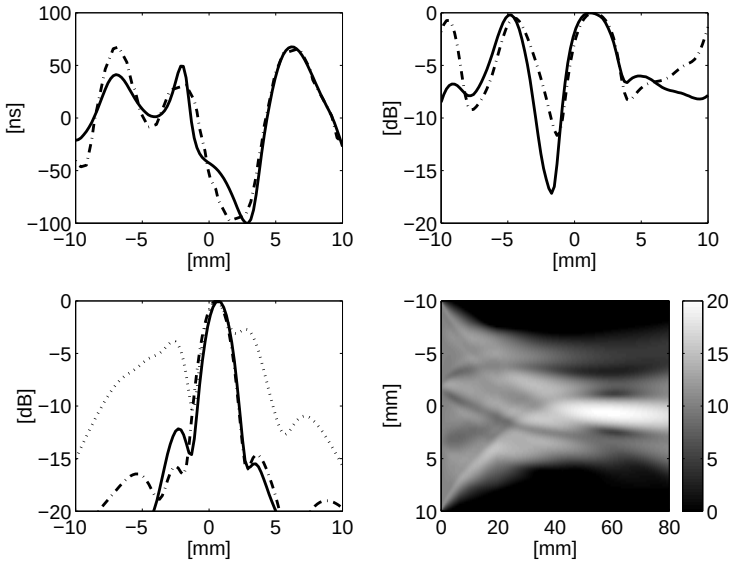

Figure 5.5: Aberration correction for the weak aberrator. An aberrated transmit pulse with a single focal point was scattered, and again aberrated. Results are shown for aberration characterisation from the first eigenfunction. Top left: estimated time-delay (solid), reference (dash-dot). Top right: estimated amplitude (solid), reference (dash-dot). Bottom left: beam profiles in the focal plane; corrected using estimate (solid), aberrated (dotted), corrected using reference (dash-dot).

V Discussion

The beam profiles obtained from corrected transmit pulses in Fig. 5.4 show that the first two eigenfunctions will focus the transmit pulse at maxima for the initial transmit pulse. The corresponding eigenvalues are 1.0 and 0.8, respectively. Therefore they will both result in a reasonable focusing, but at different locations. The third eigenfunction is associated with a smaller eigenvalue (0.5), and hence does not produce the same degree of focusing when used as an aberration correction filter. The same trend is also apparent in Fig. 5.7 for the strong aberration. However, the corrected pulse here shows a more marked split into two relatively large lobes. This is due to the severe aberration also having two more or less equal lobes.

When comparing the estimated time-delays and amplitudes to their respective references, there is relatively close concurrence with the first eigenfunction in the simulations using the weak aberrator and for the second eigenfunction in the simulations using the strong aberrator. The amplitude of the eigenfunction does,

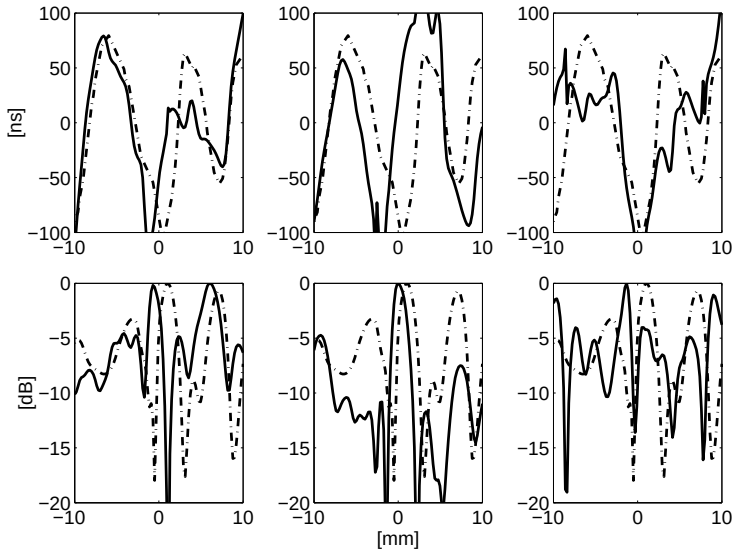

Figure 5.6: Characterisations of the aberration. The transmit pulse with a single focal point was aberrated both on transmit and receive using the strong aberrator. The panel layout is the same as in Fig. 5.3. Relative magnitude of the eigenvalues was: 1, 0.7 and 0.4. A linear slope of 7.9, 5.8 and 5.9 degrees (left to right) was removed from the time-delays before presentation.

however, include an additional apodisation compared to the reference. Apodisation is commonly used to reduce the side-lobe levels at the expense of broadening the main lobe. In the presence of aberration, however, apodisation may well produce increased aberration instead of reduced side-lobe levels. As the eigenfunction will produce a corrected transmit pulse which focuses the energy according to Eq. (5.10), the appropriate apodisation will be part of the eigenfunction itself. No additional apodisation is therefore necessary, and may indeed alter the transmit pulse sufficiently to make the eigenfunction an ineffective correction filter.

For the strong aberrator, the first eigenfunction produces a corrected beam profile with a maximum which does not coincide with the maximum of the reference. The second eigenfunction does recover the correct maximum. The eigenfunction which produces a shifted focus also has a linear term in the phase, corresponding to a larger steering angle. However, even the second eigenfunction has a significant linear term, although it is smaller than for the first eigenfunction. This is due to the fact that asymmetric side lobes will contribute to an effective shift of the centre of mass for the beam profile. It is tempting, although not necessarily correct to assume that removing the linear slope observed in the phase estimate will recover the correct focal

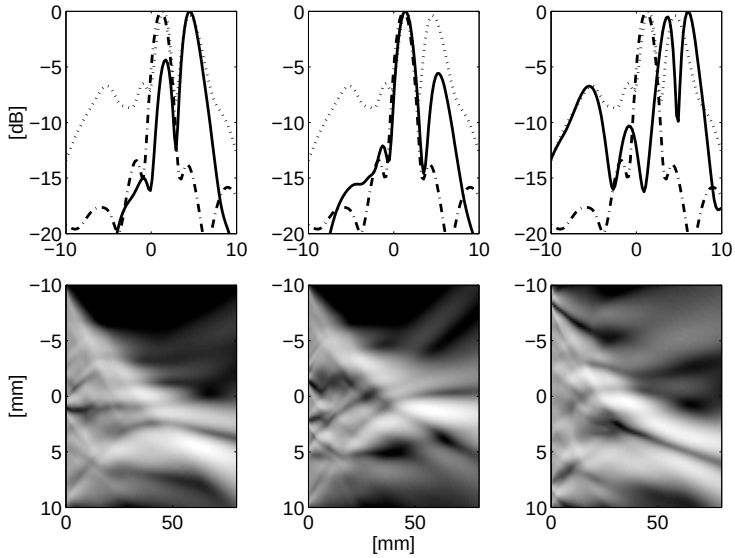

Figure 5.7: Corrected beam profiles. The characterisation of the strong aberrator, presented in Fig. 5.6, was used to transmit a corrected transmit signal through the aberrator. Panel layout is the same as in Fig. 5.4.

point. Again this is because the filter has been constructed to focus transmit energy according to a specific criterion. Altering the filter may invalidate these properties. That being said, when the steering angle is small, the isoplanatic assumption justifies removing the slope.

Subsequent eigenfunctions will have corresponding eigenvalues which are smaller, and do not concentrate the beam to the same extent when used for aberration correction. They are, therefore, not as compelling for focusing purposes. In addition, the linear phase will be highly influenced by asymmetric side lobes, making it difficult to predict the actual focal point.

Using the argument about the linear component of the eigenfunction phase, an eigenfunction with minimal linear term of the phase will concentrate the corrected pulse around the same location as the initial pulse. It will, therefore, not add significantly to the translation of the focal point. However, the focusing will be weaker for smaller eigenvalues. As a result, a trade-off will have to be made, depending on whether a narrow focus is desired or if a correctly-located focus is more important. An iterative procedure will improve the focus. This is demonstrated in Fig. 5.8.

The aberration correction technique presented here is based on an energy maximisation, and hence will focus the signal according to Eq. (5.10). The focusing

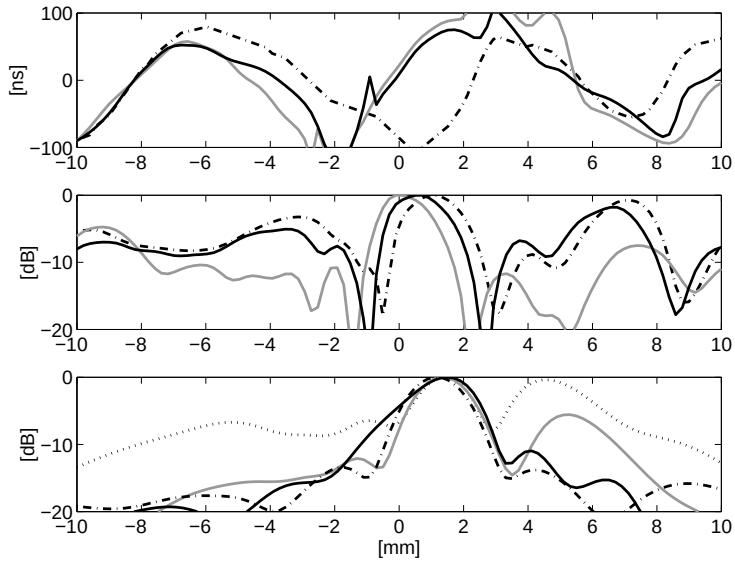

Figure 5.8: Iterative characterisation of aberration from the strong aberrator. Top: initial delay estimate (solid light grey), iterated delay estimate (solid black) compared to reference (dash-dot). Middle: initial amplitude estimate (solid light grey), iterated amplitude estimate (solid black) compared to reference (dash-dot). Bottom: aberrated beam profile (dotted), beam profile from first correction (solid light grey), beam profile for second correction (solid black), beam profile for correction with reference.

properties are therefore preserved, even for strong aberration.

The focus of this paper has been to show how eigenfunctions may be applied as aberration correction filters in order to improve the transmit focus for ultrasound imaging. It is obvious, however, that aberration correction also needs to be applied on the receive signal in order to form a good image. By construction, using the eigenfunction associated with the largest eigenvalue will produce the highest expected energy in the beamformer output of any aberration correction filters for the given receive signal. As the image is formed from the envelope of this beamformer output, the filter maximises what has been referred to as *speckle brightness*.[25] Zhao and Trahey[26] suggested using speckle brightness as an image quality factor. Using this measure, the eigenfunction will not only produce an improved transmit focus, but also result in an optimal ultrasound image, when applied for aberration correction on the received signal.

VI Conclusion

Theoretical considerations of the far-field scattering pattern suggest that eigenfunctions associated with large eigenvalues of a Fredholm integral operator possess the desired focusing properties when used as an aberration correction filter. The kernel function of this operator is the covariance function of the received stochastic backscatter. In the limiting case, where the transmitted pulse is reflected from only the focal point, the operator will have only one non-zero eigenvalue, and the corresponding eigenfunction will coincide with the generalised screen model for the aberration. This is analogous to the focusing properties of eigenfunctions investigated in Refs. 13 and 14.

Scattering simulations have been presented to illustrate the focusing property. The degree of aberration correction obtained depends on the size of the corresponding eigenvalue relative to the others.

A linear term in the phase of the eigenfunction indicates that the focal point of the corrected pulse will be shifted relative to the initially transmitted pulse. This will therefore contribute to a shift of the corrected focal point away from the intended focal point. Allowing the use of eigenfunctions with a lower eigenvalue makes it possible to reduce this movement by selecting an eigenfunction with a small linear term. This comes at the expense of the focus quality of the corrected transmit pulse. An iterative approach where the eigenfunction with smallest linear term is used in each step, will recover the lost degree of focusing, and thus provide an optimal focus recovery.

Acknowledgments

This work was financed, in part, by a grant from the Norwegian Research Council, and partly by the Norwegian University of Science and Technology.

References

[1] M. O'Donnell and S. W. Flax, "Phase-aberration correction using signals from point reflectors and diffuce scatterers: Measurements," *IEEE Trans. Ultrason. Ferroelectr. Freq. Control*, vol. 35, no. 6, pp. 768–774, 1988.

[2] U. Haberkorn, G. Layer, V. Rudat, I. Zuna, A. Lorenz, and G. van Kaick, "Ultrasound image properties influenced by abdominal wall thickness and composition," *J. Clin. Ultrasound*, vol. 21, pp. 423–429, 1993.

[3] L. Hinkelman, D.-L. Liu, L. A. Metlay, and R. C. Waag, "Measurements of ultrasonic pulse arrival time and energy level variations produced by propagation through abdominal wall," *J. Acoust. Soc. Am.*, vol. 95, no. 1, pp. 530–541, January 1994.

[4] L. Hinkelman, T. D. Mast, L. Metlay, and R. C. Waag, "The effect of abdominal wall morphology on ultrasonic pulse distortion. part I. measurements," *J. Acoust. Soc. Am.*, vol. 104, no. 6, pp. 3635–3649, December 1998.

[5] G. E. Trahey, P. D. Freiburger, L. F. Nock, and D. C. Sullivan, "In-vivo measurements of ultrasonic beam distortion in the breast," *Ultrason. Imaging*, vol. 13, no. 1, pp. 71–90, 1991.

[6] T. D. Mast, L. Hinkelman, M. O, V. Sparrow, and R. C. Waag, "Simulation of ultrasonic pulse propagation through the abdominal wall," *J. Acoust. Soc. Am.*, vol. 102, no. 2, pp. 1177–1190, August 1997.

[7] T. D. Mast, L. Hinkelman, M. Orr, and R. C. Waag, "The effect of abdominal wall morphology on ultrasonic pulse distortion. part II. simulations," *J. Acoust. Soc. Am.*, vol. 104, no. 6, pp. 3651–3664, December 1998.

[8] M. Fink, "Time reversal of ultrasonic fields - part I: Basic prinsiples," *IEEE Trans. Ultrason. Ferroelectr. Freq. Control*, vol. 39, pp. 555–567, 1992.

[9] S. W. Flax and M. O'Donnell, "Phase-aberration correction using signals from point reflectors and diffuce scatterers: Basic prinsiples," *IEEE Trans. Ultrason. Ferroelectr. Freq. Control*, vol. 35, no. 6, pp. 758–767, 1988.

[10] S. E. Måsøy, T. F. Johansen, and B. Angelsen, "Correction of ultrasonic wave aberration with a time delay and amplitude filter," *J. Acoust. Soc. Am.*, vol. 113, no. 4, pp. 2009–2020, April 2003.

[11] B. A. Angelsen, *Ultrasound imaging. Waves, signals and signal processing.* Trondheim, Norway: Emantec, 2000, vol. 2, http://www.ultrasoundbook.com.

[12] G. C. Ng, S. S. Worrell, P. D. Freiburger, and G. E. Trahey, "A comparative evaluation of several algorithms for phase aberration correction," *IEEE Trans. Ultrason. Ferroelectr. Freq. Control*, vol. 41, no. 5, pp. 631–643, 1994.

[13] T. D. Mast, A. I. Nachman, and R. C. Waag, "Focusing and imaging using eigenfunctions of the scattering operator," *J. Acoust. Soc. Am.*, vol. 102, no. 2, pp. 715–725, August 1997.

[14] C. Prada, J. L. Thomas, and M. Fink, "The iterative time reversal process: analysis of convergence," *J. Acoust. Soc. Am.*, vol. 97, no. 1, pp. 62–71, January 1995.

[15] M. F. Hamilton and D. T. Blackstock, *Nonlinear Acoustics*. San Diego: Academic Press, 1997.

[16] B. A. Angelsen, *Ultrasound imaging. Waves, signals and signal processing*. Trondheim, Norway: Emantec, 2000, vol. 1, http://www.ultrasoundbook.com.

[17] G. Taraldsen, "Derivation of a generalized Westervelt equation for nonlinear medical ultrasound," *J. Acoust. Soc. Am.*, vol. 109, no. 4, pp. 1329–1333, April 2001.

[18] T. D. Mast, L. Sourian, D.-L. Liu, M. Tabei, A. Nachman, and R. C. Waag, "A k-space method for large-scale models of wave propagation in tissue," *IEEE Trans. Ultrason. Ferroelectr. Freq. Control*, vol. 48, no. 2, pp. 341–354, March 2001.

[19] L. A. Segel, *Mathematics Applied to Continuum Mechanics*. New York: Dover, 1987.

[20] R. McOwen, *Partial Differential Equations*. Englewood Cliffs, New Jersey: Prentice Hall, 1996.

[21] D. L. Snyder, *Random Point Processes*. New York: Wiley, 1975.

[22] E. Kreyszig, *Introductory Functional Analysis*. Wiley, 1989.

[23] D.-L. Liu and R. C. Waag, "Estimation and correction of ultrasonic wavefront distortion using pulse-echo data received in a two-dimensional aperture," *IEEE Trans. Ultrason. Ferroelectr. Freq. Control*, vol. 45, no. 2, pp. 473–489, 1988.

[24] T. Varslot, G. Taraldsen, T. Johansen, and B. Angelsen, "Computer simulation of forward wave propagation in non-linear, heterogeneous, absorbing tissue." in *Proc. 2001 IEEE-UFFC Ultrasonics Symposium*, 2001, pp. 1193–1196.

[25] G. E. Trahey and S. W. Smith, "Properties of acoustical speckle patterns in the presence of phase aberration. part i: First order statistics," *Ultrason. Imaging*, vol. 6, pp. 12–28, 1988.

[26] D. Zhao and G. E. Trahey, "A statistical analysis of phase aberration correction using image quality factors in coherent imaging systems," *IEEE Trans. Med. Imaging*, vol. 11, no. 3, pp. 446–452, 1992.

Chapter 6

An approximate maximum likelihood estimator

T. Varslot*, S.-E. Måsøy†
*) Dept. Mathematical Sciences, NTNU
†) Dept. Circulation and Imaging, NTNU

The generalised frequency-dependent screen is used to model wavefront aberration in medical ultrasound imaging. Here a maximum likelihood estimator for the generalised frequency-dependent screen is derived. The underlying assumptions are that the acoustic backscatter measured at each transducer element is a realisation of a Gaussian stochastic process and that the cross-spectra between each pair of these processes is known *a priori*. The relationship between this estimator and previously developed estimators is explored.

I Introduction

In order to construct an appropriate aberration correction filter, the relevant information must be extracted from acoustic backscatter. Many approaches to extracting this information have been suggested. Most commonly, a pure time-delay is determined from a cross-correlation function between a given signal and a reference. The reference may be the measured backscatter at an adjacent transducer element,[1] the coherent sum of all measurements[2] or the coherent sum of corrected measurements in a neighbouring region.[3] The time-delay is then found as the temporal displacement of the peak value of the correlation function. An overview of such methods for extracting time-delays was recently published.[4]

The time-delay model does not describe the distortion of the pulse shape observed in medical ultrasound.[5] Therefore, in some situations, a time-delay screen

may not be adequate for describing the aberration. Moving the screen away from the transducer surface has been suggested as a way to characterise the pulse-shape distortion and amplitude fluctuation introduced by interference between different parts of the pulse.[6] The utility of also including amplitude when performing aberration correction has been demonstrated,[7] and various methods for extracting amplitude and time-delays or, more generally, a *generalised frequency-dependent screen*, have been published.[8,9,10,11]

However, none of these methods applies the *maximum likelihood principle*.[12] A *maximum likelihood estimate* (MLE) for the generalised frequency-dependent screen is a natural approach because it will asymptotically achieve the Cramér-Rao lower bound for the estimator variance. An algorithm for estimating time-delays based on the maximum likelihood principle was presented by Fortes.[13,14] An underlying assumption for the work was that the unaberrated signal consisted of a deterministic *desired signal* and additive speckle noise. The aberration was modelled using a time-delay at the transducer surface. This signal model requires the scattering object to scatter equally in all directions. An example would be a strong point reflector embedded in a diffuse scattering distribution. However, the main focus of that paper was the develpment of an electronic circuit for solving the resulting set of equations, rather than an analysis of the equations themselves.

The goal for the present work is to estimate aberration based on a pure speckle signal. The development of the MLE is therefore somewhat simplified compared to what is presented by Fortes.

II Maximum likelihood estimation

II.A Signal model

Let a temporal frequency component of the measured signal at the transducer be

$$y(\omega) = \left[y_1(\omega), y_2(\omega), \ldots, y_N(\omega)\right]^{\mathrm{T}},$$

where $y_k(\omega)$ represents the signal at transducer element k. Furthermore, let

$$f(\omega) = [f_1(\omega), f_2(\omega), \ldots, f_N(\omega)]^{\mathrm{T}}$$

be a vector representing a temporal frequency component in the unaberrated acoustic backscatter. The aberration model used here is the *generalised frequency-dependent screen*. At a given frequency the screen may be represented by a vector $s(\omega) = [s_1(\omega), \ldots s_N(\omega)]^{\mathrm{T}}$ or a diagonal matrix $S(\omega)$ with elements $S_{kk}(\omega) = s_k(\omega)$. If explicit dependence on ω is omitted, the relationship between y and f is

$$y = Sf. \tag{6.1}$$

A natural assumption is that the matrix S is non-singular, since this corresponds to $s_k \neq 0$ for all k. In many ultrasound imaging situations the acoustic backscatter may be modelled by a Gaussian process. In this case, the temporal Fourier transform of the discretely sampled backscatter at each transducer element will be a realisation of a complex Gaussian variable for a given frequency. The vector y will therefore be a complex Gaussian random vector with covariance matrix R given by

$$R = E\left[yy^H\right] = E\left[Sff^HS^H\right] = SFS^H, \tag{6.2}$$

where F is the corresponding covariance matrix of the unaberrated backscatter f. There is no loss in generality in assuming that f is normalised such that $F_{kk} = 1$. The goal is to estimate S, or equivalently s based on the observations of y.

Strictly speaking R and F are cross-spectra associated with the stochastic processes at each element. However, for the purpose of this work it is more natural to consider them as covariance matrices associated with the stochastic vectors y and f, respectively.

II.B Classical theory

Following Burg *et al.*[15] the maximum likelihood estimate of *structured covariance matrices* for complex Gaussian processes is obtained as follows. If $\{y_{(1)},\ldots,y_{(M)}\}$ are M observations of a zero-mean random vector y of length n, with a Complex Gaussian distribution, the joint probability for $\{y_{(1)},\ldots,y_{(M)}\}$ is

$$p(y_{(1)},\ldots,y_{(M)};R) = \frac{1}{(2\pi)^{nM}|R|^M}\exp\left(-\frac{1}{2}\sum_{m=1}^{M} y_{(m)}^H R^{-1} y_{(m)}\right),$$

where R is the covariance matrix for y, and $|R|$ denotes its determinant. A MLE for R, given the observations, is provided by maximising $p(y_{(1)},\ldots,y_{(M)};R)$ with respect to R, or equivalently maximising $\ln[p(y_{(1)},\ldots,y_{(M)};R)]$ with respect to R. Omitting constant terms, this is the same as maximising

$$g(R;y_{(1)},\ldots,y_{(M)}) = -\ln|R| - \frac{1}{M}\sum_{m=1}^{M} y_{(m)}^H R^{-1} y_{(m)}.$$

For a scalar a, the trace $\mathrm{tr}[a] = a$, implying that

$$\begin{aligned} g(R; y_{(1)}, \ldots, y_{(M)}) &= -\ln|R| - \frac{1}{M}\sum_{m=1}^{M} \mathrm{tr}\left[y_{(m)}^H R^{-1} y_{(m)}\right] \\ &= -\ln|R| - \frac{1}{M}\sum_{m=1}^{M} \mathrm{tr}\left[R^{-1} y_{(m)} y_{(m)}^H\right] \\ &= -\ln|R| - \mathrm{tr}\left[R^{-1}\frac{1}{M}\sum_{m=1}^{M} y_{(m)} y_{(m)}^H\right] \\ &= -\ln|R| - \mathrm{tr}\left[R^{-1}\hat{R}\right]. \end{aligned}$$

The standard estimate for the correlation function is here denoted by

$$\hat{R} = \frac{1}{M}\sum_{m=1}^{M} y_{(m)} y_{(m)}^H.$$

The MLE of R is therefore found by maximising

$$g(R; \hat{R}) = -\ln|R| - \mathrm{tr}\left[R^{-1}\hat{R}\right] \tag{6.3}$$

with respect to R. This should be a maximum over all *admissible* R. Therefore, the maximum depends on the structure of R. Inserting the signal model from Eq. (6.2) into Eq. (6.3) yields

$$g(SFS^H; \hat{R}) = \ln|F| - 2\sum_{k=1}^{N} \ln|s_k| - \mathrm{tr}\left[S^{-H}F^{-1}S^{-1}\hat{R}\right].$$

If F is known *a priori*, a MLE for R, or equivalently S, is obtained by maximising $g(S; F, \hat{R})$ with respect to S

$$g(S; F, \hat{R}) \equiv -2\sum_{k=1}^{N} \ln|s_k| - \mathrm{tr}\left[S^{-H}F^{-1}S^{-1}\hat{R}\right]. \tag{6.4}$$

It is convenient to define

$$\begin{pmatrix} \sigma_1 \\ \vdots \\ \sigma_N \end{pmatrix} = \begin{pmatrix} 1/\overline{s}_1 \\ \vdots \\ 1/\overline{s}_N \end{pmatrix}, \tag{6.5}$$

and

$$A = \overline{F}^{-1} \circ \hat{R}. \tag{6.6}$$

Here $\circ$ denotes the *Hadamard product*[16] of matrices [element-wise multiplication: $A_{kn} = (\overline{F}^{-1})_{kn}\hat{R}_{kn}$]. Straightforward calculation of the trace in Eq. (6.4), combined with the definitions from Eqns. (6.5) and (6.6) produces

$$g(\sigma; A) \equiv \sum_{k=1}^{N} \ln|\sigma_k|^2 - \sigma^{\mathrm{H}} A \sigma. \tag{6.7}$$

A discussion of various properties of g is offered in Appendix A. The most important result from this discussion is that in order for the MLE to exist, the matrix A needs to be positive definite.

Since F and $\hat{R}$ are covariance matrices, they are Hermitian positive semi-definite matrices. The matrix $\overline{F}^{-1}$ also has this property. It is clear that the Hadamard product of two Hermitian matrices is Hermitian. However, it is possible to show that, in general, the Hadamard product of two positive definite matrices is also positive definite.[16] The matrix $A = \overline{F}^{-1} \circ \hat{R}$ is therefore positive provided that F and $\hat{R}$ are also positive. Existence of the MLE is in this case ensured.

The reason why A may fail to be positive is that F is not positive. In this case, the inversion of F will fail, and the likelihood-function g is not well defined. A Moore-Penrose inverse, $F^{\dagger}$, may be employed instead of the standard inverse.[17] However, this does not alter the fact that A is only semi-definite.

The underlying cause of this problem is that the model contains too many variables. The correct approach is, therefore, to reduce the number of variables in the model by a change of basis. The change of basis is accomplished by means of a singular-value decomposition[18] of F. This will not be discussed further.

A necessary condition for a maximum of g in Eq. (6.7) is that the derivative of g with respect to σ equals zero. Appendix A shows that this is achieved when

$$s = A\sigma, \tag{6.8}$$

where the relation between σ and s stated in Eq. (6.5).

It is easy to see from Eq. (6.7) that for a fixed $\sigma = [\sigma_1, \sigma_2, \ldots \sigma_N]^{\mathrm{T}}$ and for any real number θ

$$g(\sigma; A) = g(\sigma e^{i\theta}; A).$$

The solution is therefore not unique. Indeed, if A has a block-diagonal structure, the solution for one block is not coupled to the solutions for the other blocks. The solution may therefore be modified in this manner, independently for each block. An extreme case of this is when A is diagonal, in which case the absolute value of σ_k is determined from the equation, but nothing may be inferred about the phase.

The fact that the solution is not unique in this sense is explained by the physics of the problem. A phase shift which is constant over the whole aperture shifts

and modifies the shape of the ultrasound pulse, but otherwise does not affect the aberration. A unique solution may be determined by fixing the phase on a particular element. A block-diagonal structure of the matrix A implies that the signals received on the different parts of the array are uncorrelated. If this were the case, the signals at each part of the array should also be corrected independently of each other. Such decoupling does not make sense for the physical problem.

As the function g is not concave, several local maxima may exist. In order to locate the global maximum, global optimisation techniques such as *simulated annealing*[19] or *genetic algorithms*[20] may be employed. It is difficult, however, to determine the conditions under which Eq. (6.8), combined with fixing the phase on one element, is sufficient for finding a unique global maximum.

III Unaberrated transmit-beam: corrected neighbour correlation

Consider the case where F in the signal model [Eq. (6.2)] is a real "triangular matrix", *i.e.*, a Toeplitz matrix where each row and column decreases linearly from one at the diagonal. According to the van Zittert-Cernike theorem, this is what F would be if there were no aberration of the transmitted beam.[21] In this situation aberration is only introduced to the scattered signal.

It is not difficult to see that the central part of the inverse matrix F^{-1} is a "second derivative"; a tridiagonal Toeplitz matrix with a constant multiple of $[-1,2,-1]$ as the non-zero elements on each row of F^{-1}. A minor adjustment is needed in the lower left and the upper right corner of the matrix in order to handle the edges correctly, but this adjustment becomes insignificant as N becomes large.

The apparent connection between element 1 and element N in F^{-1} is artificial, and is an indication that the model is not properly specified for this correlation matrix F. In this discussion it will simply be omitted since it is asymptotically negligible.

For an $(N \times N)$ matrix it is convenient to write the matrix as follows:

$$F^{-1} = N\left(\tilde{I} - W\right).$$

Here $\tilde{I}$ and W are defined as

$$\tilde{I} = \begin{pmatrix} 1/2 & & & & \\ & 1 & & & \\ & & \ddots & & \\ & & & 1 & \\ & & & & 1/2 \end{pmatrix}, \qquad W = \frac{1}{2}\begin{pmatrix} 0 & 1 & & & \\ 1 & \ddots & \ddots & & \\ & \ddots & \ddots & 1 & \\ & & 1 & 0 & \end{pmatrix}.$$

Inserting this into Eq. (6.8), the MLE of the screen s is a solution of

$$\left(\tilde{I}\circ\hat{R}\right)\sigma-\frac{1}{N}s=\left(W\circ\hat{R}\right)\sigma. \tag{6.9}$$

Asymptotically, as N becomes large, this becomes

$$\left(\tilde{I}\circ\hat{R}\right)\sigma=\left(W\circ\hat{R}\right)\sigma. \tag{6.10}$$

A solution for σ_{k+1} in terms of σ_k and σ_{k-1} is thus found:

$$\sigma_{k+1}=\frac{\hat{R}_{kk}\tilde{I}_{kk}}{\hat{R}_{kk+1}}\sigma_k+\frac{\hat{R}_{kk}\tilde{I}_{kk}}{\hat{R}_{kk+1}}\left(\sigma_k-\frac{\hat{R}_{kk-1}}{\hat{R}_{kk}\tilde{I}_{kk}}\sigma_{k-1}\right).$$

According to the signal model, the second term inside the parenthesis is itself an estimate of σ_k based on σ_{k-1}. This is a neighbour correlation method for σ_{k+1} with a simple correction term. In addition to fixing the phase on one of the elements, the norm, $\|\sigma\|_2$ should be specified in order to obtain a unique solution.

IV Weighted estimates

It is natural to interpret of W in Eq. (6.10) as a weight matrix in a weighted average between a forward and a backward neighbour correlation method. This is basis for the following formulation.

Let I be the identity matrix. Using the Hadamard product as a notation for the diagonal matrix consisting of the diagonal elements of another matrix, the matrices $\tilde{I}$ and W are defined as

$$\left(\tilde{I}\right)_{kn}=\left(I\circ\overline{F}^{-1}\right)_{kn}=\begin{cases}\left(\overline{F}^{-1}\right)_{kk} & k=n\\ 0 & k\neq n\end{cases}$$

$$W=\tilde{I}-\overline{F}^{-1}.$$

Equation (6.8) is now rewritten as

$$\left(\tilde{I}\circ\hat{R}\right)\sigma-s=\left(W\circ\hat{R}\right)\sigma. \tag{6.11}$$

Compare this equation to Eq. (6.9).

IV.A Linear approximation

In the case of the unaberrated transmit-beam, the second term on the left of Eq. (6.11) was negligible compared to the other two terms. The problem was then reduced to a set of linear equations for σ.

Consider the case where Eq. (6.11) is approximated by the linear set of equations

$$\left(\tilde{I}\circ\hat{R}\right)\sigma = \left(W\circ\hat{R}\right)\sigma. \tag{6.12}$$

These equations leave the norm of the solution undetermined. Therefore, an additional constraint such as $\|\sigma\|_2 = 1$ is permitted. Since the matrix $\tilde{I}\circ\hat{R}$ is a diagonal matrix consisting of the product of diagonal elements from F^{-1} and $\hat{R}$, it is easily inverted. This may be utilised to formulate an eigenvalue problem for the quantity $e_k = (\sigma_k\sqrt{\hat{R}_{kk}})$:

$$e = \left(\tilde{I}\circ\hat{R}\right)^{-\frac{1}{2}}\left(W\circ\hat{R}\right)\left(\tilde{I}\circ\hat{R}\right)^{-\frac{1}{2}} e.$$

The estimate is thus $\sigma_k = e_k/\sqrt{\hat{R}_{kk}}$. Existence and uniqueness of this approximate solution depends on 1 being an eigenvalue of the matrix, and that this eigenvalue has multiplicity 1.

A slightly different approach is to look for a solution of Eq. (6.12) in the least-mean-square-error sense. This is equivalent to defining the solution as

$$\sigma = \underset{\|\sigma\|_2=1}{\operatorname{argmin}} \|A\sigma\|_2,$$

where, once again, $A = \overline{F}^{-1}\circ\hat{R}$. As mentioned previously, the matrix A is assumed to be Hermitian and positive definite. The solution is thus found as an eigenvector associated with the smallest eigenvalue of this matrix. Assuming the eigenvalue has multiplicity 1, the solution is unique when the phase on one element is fixed.

Unfortunately, small eigenvalues tend to be associated with noise in the data used to form $\hat{R}$. The estimate is therefore not very attractive from a practical point of view. Neglecting the small term, in the same manner as when one obtains the corrected neighbour estimator, has consequences for the ability of the estimator to perform well in a noisy environment.

A common remedy for this problem is regularisation.[17] The matrix A which is a linear operator on σ is, in fact, a nonlinear operator on s. The usual formulation for Tikhonov regularisation of nonlinear problems is

$$s = \underset{\|\sigma\|_2=1}{\operatorname{argmin}} \|A\sigma\|_2 + \epsilon\|s\|_2 \quad \text{with } \sigma_k = 1/\overline{s}_k,$$

where ϵ is a regularisation parameter.

It is of interest to note that an LMSE solution of Eq. (6.11) is

$$s = \operatorname{argmin} \|A\sigma - s\|_2. \tag{6.13}$$

Let s_* be *a priori* information about what the solution s should be. A nonlinear regularisation scheme is then

$$s = \underset{\|\sigma\|_2=1}{\operatorname{argmin}} \|A\sigma - s_*\|_2 + \epsilon\|s - s_*\|_2, \text{ with } \sigma_k = 1/\overline{s}_k. \tag{6.14}$$

IV.B Model-based approximation

Consider a modification of Eq. (6.11) where a term $\tilde{I}s$ is added on both sides. The result is rewritten as

$$\left(\tilde{I}-I\right)s=\left(W\circ\hat{R}\right)\sigma+\tilde{I}s-\left(\tilde{I}\circ\hat{R}\right)\sigma. \tag{6.15}$$

According to the signal model described in Sec. II.A

$$R_{kn}=s_kF_{kn}\overline{s}_n.$$

Thus, if a good estimate $\hat{R}_{kn}$ of R_{kn} is obtained, the following approximation is valid:

$$\tilde{I}s-\left(\tilde{I}\circ\hat{R}\right)\sigma\approx\tilde{I}s-\left(\tilde{I}\circ F\right)s=0.$$

Applying the approximation to Eq. (6.15) produces the modified estimate

$$s=\left(\tilde{I}-I\right)^{-1}\left[W\circ\hat{R}\right]\sigma=\left(\tilde{W}\circ\hat{R}\right)\sigma,$$

where the modified weight matrix $\tilde{W}$ is

$$\tilde{W}=\left(\tilde{I}-I\right)^{-1}W=\left(\tilde{I}-I\right)^{-1}\left(\tilde{I}-\overline{F}^{-1}\right). \tag{6.16}$$

This estimate may be written out for a particular element

$$\begin{aligned}s_k&=\sum_{n\neq k}\frac{-\overline{F}_{kn}^{-1}\hat{R}_{kn}}{\overline{F}_{kk}^{-1}-1}\frac{1}{\overline{s}_n}=\sum_n\tilde{W}_{kn}\frac{\hat{R}_{kn}}{F_{kn}}\frac{1}{\overline{s}_n}\\ \tilde{W}_{kn}&=\begin{cases}\frac{\overline{F}_{kn}^{-1}\overline{F}_{nk}}{1-\overline{F}_k^{-1}}=\frac{\overline{F}_{kn}^{-1}\overline{F}_{nk}}{\sum_{m\neq k}\overline{F}_{km}^{-1}\overline{F}_{mk}} & k\neq n\\ 0 & k=n.\end{cases}\end{aligned} \tag{6.17}$$

According to the signal model, $\hat{R}_{kn}/F_{kn}\overline{s}_n$ is, itself, an estimate for s_k. Since $\sum_n\tilde{W}_{kn}=1$, the estimate is a weighted-average estimate. The weights are permitted to take complex values.

In accordance with the previous approximation

$$\hat{R}_{kn}/\overline{s}_n\approx\hat{R}_{kn}s_n/\hat{R}_{nn}.$$

Thus, from Eq. (6.17) an estimate of the quantity $s_k/\sqrt{\hat{R}_{kk}}$ is obtained:

$$\frac{s_k}{\sqrt{\hat{R}_{kk}}}=\sum_n\tilde{W}_{kn}\frac{\hat{R}_{kn}}{F_{kn}\sqrt{\hat{R}_{kk}\hat{R}_{nn}}}\frac{s_n}{\sqrt{\hat{R}_{nn}}} \tag{6.18}$$

The solution is found as an eigenvector to the matrix with elements $\tilde{W}_{kn}\hat{R}_{kn}/F_{kn}\sqrt{\hat{R}_{kk}\hat{R}_{nn}}$. If the multiplicity of the eigenvalue is 1, this solution is unique when the magnitude of the estimate is prescribed and phase on one element is fixed.

IV.C Approximating the weight matrix

The matrix F is thus far assumed to be known *a priori*. However, it is instructive to look at approximations of F. This is important because exact knowledge of F is not available in most situations.

Consider the simple situation where the matrix F is $F = I + \tilde{F}$, where the matrix $\tilde{F}$ satisfies $\|\tilde{F}\| < 1$. In this case

$$F^{-1} = I - \tilde{F} + \tilde{F}^2 - \ldots \approx I - \tilde{F}. \tag{6.19}$$

Inserting this approximation, the weight matrix in Eq. (6.17) then becomes

$$\tilde{W}_{kn} = \begin{cases} \frac{|F_{kn}|^2}{\sum_{m \neq k} |F_{km}|^2} & k \neq n \\ 0 & k = n. \end{cases}$$

The coherence of the aberrated signal is defined as

$$w_{kn} = R_{kn} / \sqrt{R_{kk} R_{nn}}.$$

Combined with the signal model from Eq. (6.2), the square of the absolute value of the coherence is

$$|w_{kn}|^2 = |R_{kn}|^2 / |R_{kk} \| R_{nn}| = |F_{kn}|^2 / |F_{kk} \| F_{nn}|.$$

Using the assumption that $F_{kk} = F_{nn} = 1$, the modified weights are seen to be

$$\tilde{W}_{kn} = \begin{cases} \frac{|w_{kn}|^2}{\sum_{m \neq k} |w_{km}|^2} & , k \neq n \\ 0 & , k = n. \end{cases} \tag{6.20}$$

With the exception of not including the term $k = n$ in each equation, this is the *modified beamformer output* estimator (MBFO) which was proposed by Måsøy *et al.*[10] The MBFO estimator was developed as a weighted average of individual estimates. The weights were chosen based on the coherence in the acoustic backscatter using the rationale that the coherence is low when the variance is high and the estimate unreliable. As shown here, the MBFO may also be derived as an approximation to the MLE. This produces a whole family of weighted-average estimates where the weights are selected as approximations to the MLE.

V Aberration of transmit-beam

It is not very realistic to model the transmitted beam as if it was unaberrated. In an imaging situation, the pulse would have to pass though the body wall both ways.

Hence, the matrix F is a function of the aberration as well. In principle, if the aberration of the transmitted pulse may be modelled using the same screen as that causing the aberration of the scattered signal, then the van Zittert-Cernike theorem could be applied to create a model for F. In this situation

$$(F)_{kn} \sim \sum_m s_{k+m}\overline{s}_{n+m}.$$

In order to construct a true MLE based on the signal model, the structure of F should also be included when constructing the likelihood function.

However, the use of the van Cittert-Zernike theorem for an uncorrected transmit-beam is an approximation at best. A different approach is to use the structure of the MLE from a known F and insert an estimate for F. According to the signal model

$$|F_{kn}| \sim |w_{kn}|.$$

The coherence may therefore be utilised as an estimate for $|F_{kn}|$. In doing so, the phase of F is not included. This is an additional source of error in the estimate.

If there is no aberration, then the phase of F is zero. Aberration may cause the location of the focal point of the transmitted beam to be shifted (refraction), widening of the main lobe, or higher side-lobe levels. This will, in turn, produce acoustic backscatter for which the correlation matrix F is not real.

Consider the weighted-average estimate

$$s_k = \sum_n W_{kn} \frac{\hat{R}_{kn}}{F_{kn}} \frac{1}{\overline{s}_k}, \tag{6.21}$$

where the weights are assumed to satisfy $\sum_n W_{kn} = 1$. Assume for simplicity that the weights are real and positive.

To analyse the error which is introduced in the estimate by omitting the phase of F_{kn}, let s_k be the estimate of the screen according to Eq. (6.21), and let $\tilde{s}_k$ satisfy

$$\tilde{s}_k = \sum_n W_{kn} \frac{\hat{R}_{kn}}{|F_{kn}|} \frac{1}{\overline{\tilde{s}}_k}. \tag{6.22}$$

The relationship between s_k and $\tilde{s}_k$ is described as

$$s_k = \tilde{s}_k \alpha_k e^{i\delta_k}. \tag{6.23}$$

Thus the amplitude error is α_k and the phase error is δ_k. Let Δ_{kn} be the phase of F_{kn}. Because F is Hermitian and Toeplitz, the phase $\Delta_{kn} \equiv \Delta(k-n)$ is an odd function of $(k-n)$.

Inserting Eqs. (6.21) and (6.22) into Eq. (6.23), it is seen that

$$s_k = \sum_n W_{kn} \frac{\hat{R}_{kn}}{|F_{kn}|} \frac{\alpha_k \alpha_n e^{i(\delta_k - \delta_n)}}{\overline{s}_n} = \sum_n W_{kn} \frac{\hat{R}_{kn}}{|F_{kn}|} \frac{e^{-i\Delta(k-n)}}{\overline{s}_n}.$$

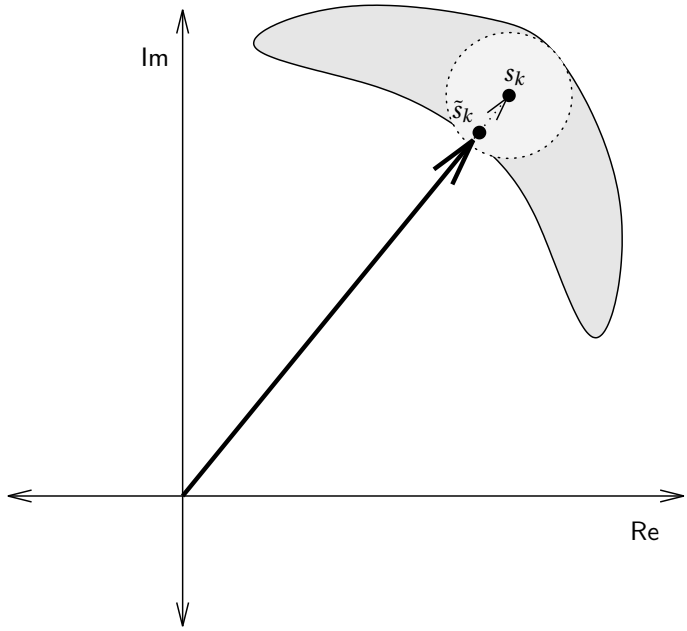

Figure 6.1: An illustration of the effect not including the phase of F has on a weighted-average estimate; *i.e.* employing Eq. (6.22) instead of Eq. (6.21).

The effect of not including Δ_{kn} is apparent when considering the estimate for a particular element, s_k, when s_n is given for all the other elements. In this case s_p is a weighted-average of properly-aligned individual estimates, more or less evenly spread about the true value. $\tilde{s}_k$, on the other hand, is an average of estimates which have a much larger angular spread than they should due to the phase of F. Since $\Delta(k-n)$ is an odd function, the additional spread of the points will be symmetrical about the expectation value, at least for the central part of the transducer. In this case the angular spread will not affect the angular expectation value, but will ensure that the radial expectation value is biased (see Fig. 6.1). At the edges of the transducer, where the estimate does not contain the same number of points to each side, the phase may also be affected.

If the weights are non-zero only in a narrow band about the diagonal, or equivalently, if the phase of F varies slowly as a function of space, then the estimate is not significantly affected by the missing $\Delta(k-n)$. However, when the weights are non-zero over a wider band, then the missing phase will introduce an error in the amplitude estimate.

A trade-off must be made when selecting the weights. Averaging over a large

number of neighbours will potentially yield an estimate with a low variance. However, it the transmitted pulse is aberrated, such that the phase of F is non-zero, averaging over a large number of neighbours will bias the amplitude estimate.

VI Simulations

In order to illustrate the MLE-based estimation, a two-dimensional (2D) simulation of acoustic backscatter from a uniform distribution of point scatterers was performed. The scatterers were ensonified by a transmit-beam of 2.5 MHz with a geometric focus 6 cm from the transmitting array. The width of the transmitting array was 2 cm.

The scattering region was filled with approximately 1600 point scatterers/cm^2. This is sufficient to ensure that the backscatter is approximately a Gaussian process. [22] Aberration was introduced using a model emulating aberration from the human abdominal wall. [7]

In all figures MLE is the estimate obtained as the global maximum of Eq. (6.7) and MBFO(F) denoted the weighted average estimate obtained by employing the weights from Eq. (6.20). Estimates obtained from a modification of Eq. (6.20) where F_{pn} is replaced by $|F_{pn}|$ are labelled MBFO(|F|). Furthermore, mle2 and mle4 denote estimates obtained as solutions of Eqs. (6.13) and (6.14), respectively.

Equations (6.7), (6.13) and (6.14) were solved with a genetic algorithm published by Dorsey *et al.* [23] The MBFO estimates were obtained using a fix-point iteration. [10]

Figure 6.2 shows the phase and absolute value of the cross-correlation function for the unaberrated acoustic backscatter produced by an unaberrated transmit-beam. The amplitude decreases linearly from the diagonal, as predicted by the van Cittert-Zernike theorem. With the exception of errors in the estimate at the lower left and upper right corners, the phase is zero, also in accordance with the van Cittert-Zernike theorem.

Figure 6.3 shows the phase and absolute value of the cross-correlation function for the unaberrated acoustic backscatter produced by an aberrated transmit-beam. The amplitude decreases much more rapidly from the diagonal than for the unaberrated transmit-beam in Fig. 6.2. The phase is also no longer zero.

Time-delay and amplitude estimates obtained from an unaberrated transmit-beam are shown in Fig. 6.4. As a reference, estimates obtained from a point scatterer are also indicated.

Time-delay and amplitude estimates obtained from an aberrated transmit-beam are shown in Fig. 6.5. Estimates obtained from a point scatterer are also indicated.

Finally, a linear slope was subtracted from each estimate. The results are shown both for the unaberrated transmit-beam and the aberrated transmit-beam in Fig. 6.6.

All estimators provide reasonable results for the time-delays. Most notably, the MBFO($|F|$) stands out as the only estimate which is unable to detect the linear slope in

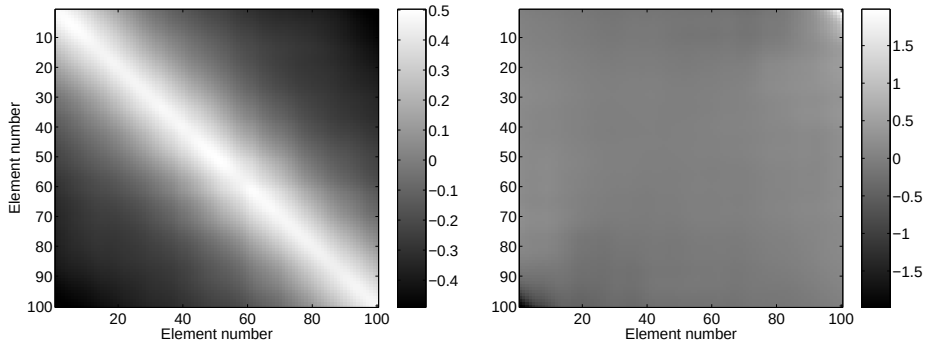

Figure 6.2: Cross-correlation for unaberrated acoustic backscatter (F) from unaberrated transmit-beam. Left: absolute value of F. Right: phase of F.

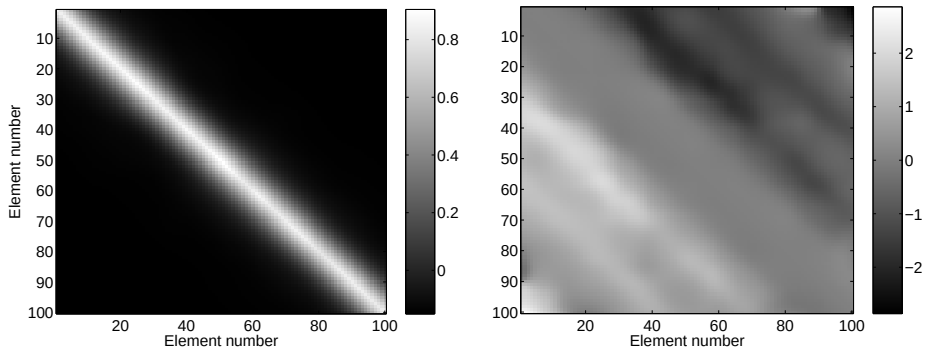

Figure 6.3: Cross-correlation for unaberrated acoustic backscatter (F) from aberrated transmit-beam. Left: absolute value of F. Right: phase of F.

the time-delay. Failure to detect the linear slope is not to be considered a weakness of the estimate, since a linear slope is generally not detectable using acoustic backscatter from random scatterers in a two-way imaging system. Additional information is required, *e.g.* a point reflector with a known location. The extra insight provided by knowing F is enough to enable the determination of the linear slope.

Removing the linear slope in the time-delay estimates results in almost identical estimates for all estimators. The estimates also compare well with the reference obtained from a point source simulation.

For the unaberrated transmit-beam all estimators perform well, also as amplitude estimators. The differences are only reflected in the ability to predict large amplitude fluctuations. It seems like MLE-based estimates under-estimate the amplitude

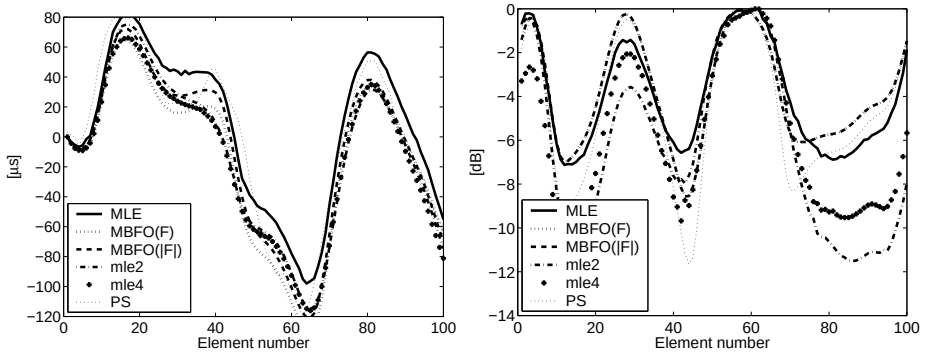

Figure 6.4: Time-delay and amplitude estimates based on unaberrated transmit-beam.

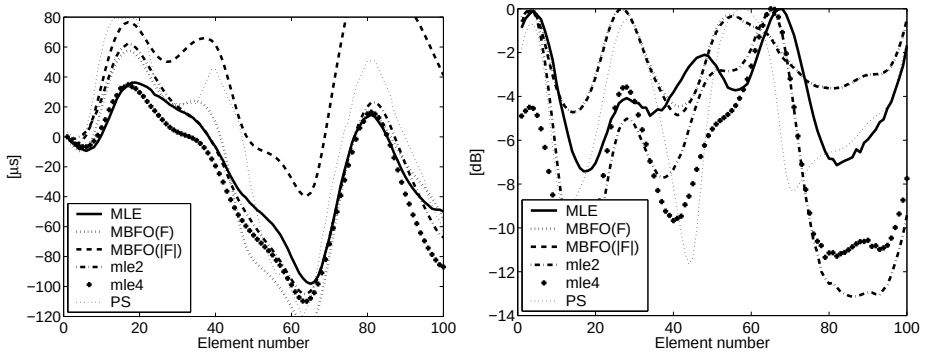

Figure 6.5: Time-delay and amplitude estimates based on aberrated transmit-beam.

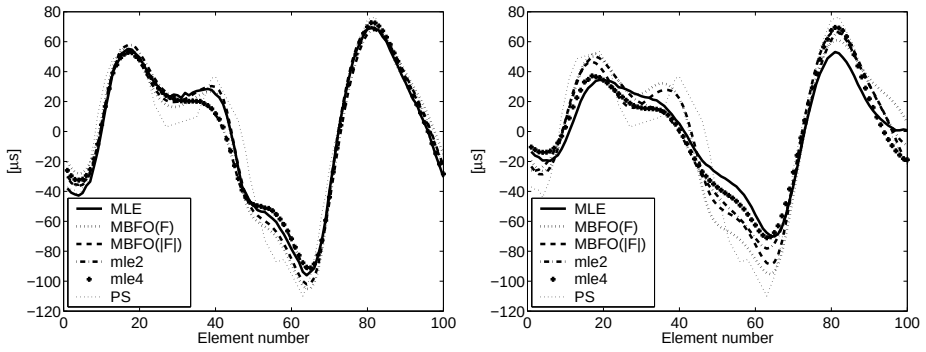

Figure 6.6: Time-delay estimates where the linear slope has been removed. Left: based on unaberrated transmit-beam. Right: based on aberrated transmit-beam.

fluctuations systematically when compared to the point source reference.

In the aberrated case, only the MBFO algorithm yields an estimate which is comparable to the point source estimate. All the other estimates return an amplitude estimate which is very different from the point source. The maximum seemed to be stable for all three estimators. Furthermore, they display similarities which indicate that the MLE is genuinely different from the point source.

In the case of an aberrated transmit-beam, the acoustic backscatter will be generated from a large area. If this area is not within the isoplanatic patch of the aberrator, the difference between the measured backscatter and the unaberrated backscatter will not be modelled by the same screen as for the point source. This is the most likely cause of the difference between the MLE-based estimates and the point source reference, and was discussed by Måsøy *et al.*[10] The MBFO algorithm does seem to perform better when compared to the point source reference, although amplitude variations here are also much smaller than for the reference. The poor performance of the MLE-based estimates are, in this situation, caused by an incorrect underlying model.

It is interesting to note that both the amplitude and time-delay estimates for the MBFO algorithm are almost identical when applying F as when applying $|F|$. Omitting the phase of F does not, therefore, seem to have much effect in this situation.

VII Concluding remarks

The MLE for the generalised frequency-dependent screen has been developed for a situation where the unaberrated acoustic backscatter is assumed to be known. The critical points for the likelihood-function are determined by a nonlinear relation which, through model-based approximations, reduces to a weighted-average estimate of the screen.

For an unaberrated transmit-beam, the covariance function of the unaberrated backscatter is a "triangular matrix". In this situation, the MLE of the screen turns out to be a neighbour correlation method with a simple correction term. This estimate is sensitive to noise, and not the preferred option in practical situations. An alternative solution is found by nonlinear regularisation of the critical-point conditions.

The MBFO was originally developed by forming a weighted average of individual estimates. As the variance in each individual estimate depends on the coherence, the weights were chosen according to the coherence. It turns out that this choice coincides with the MLE under certain conditions. The rationale is valid even if the assumption behind this approximation is not satisfied. It is therefore a reasonable estimate, also in other situations. However, the connection to the MLE is then not apparent.

References

[1] S. W. Flax and M. O'Donnell, "Phase-aberration correction using signals from point reflectors and diffuce scatterers: Basic prinsiples," *IEEE Trans. Ultrason. Ferroelectr. Freq. Control*, vol. 35, no. 6, pp. 758–767, 1988.

[2] L. F. Nock, G. E. Trahey, and S. W. Smith, "Phase aberration correction in medical ultrasound using speckle brightness as an image quality factor," *J. Acoust. Soc. Am.*, vol. 85, no. 5, pp. 1819–1833, May 1989.

[3] G. C. Ng, S. S. Worrell, P. D. Freiburger, and G. E. Trahey, "A comparative evaluation of several algorithms for phase aberration correction," *IEEE Trans. Ultrason. Ferroelectr. Freq. Control*, vol. 41, no. 5, pp. 631–643, 1994.

[4] F. Viola and W. F. Walker, "A comparison of the performance of time-delay estimators in medical ultrasound," *IEEE Trans. Ultrason. Ferroelectr. Freq. Control*, vol. 50, no. 4, pp. 392–401, April 2003.

[5] D.-L. Liu and R. C. Waag, "Time-shift compensation of ultrasonic pulse focus degradation using least-mean-square-error estimates of arrival time," *J. Acoust. Soc. Am.*, vol. 95, no. 1, pp. 542–555, January 1994.

[6] ——, "Correction of ultrasound wavefront distortion using backpropagation and a reference waveform method for time-shift compensation," *J. Acoust. Soc. Am.*, vol. 96, no. 2, pp. 649–660, August 1994.

[7] S. E. Måsøy, T. F. Johansen, and B. Angelsen, "Correction of ultrasonic wave aberration with a time delay and amplitude filter," *J. Acoust. Soc. Am.*, vol. 113, no. 4, pp. 2009–2020, April 2003.

[8] F. Lin and R. C. Waag, "Estimation and compensation of ultrasonic wavefront distortion using a blind system identification method," *IEEE Trans. Ultrason. Ferroelectr. Freq. Control*, vol. 49, no. 6, pp. 739–755, 2002.

[9] T. Varslot, B. A. Angelsen, and R. C. Waag, "Spectral estimation for characterization of acoustic aberration," *J. Acoust. Soc. Am.*, vol. 116, no. 1, pp. 97–108, July 2004.

[10] S.-E. Måsøy, T. Varslot, and B. Angelsen, "Estimation of ultrasonic wave aberration with signals from random scatterers," *J. Acoust. Soc. Am.*, vol. 115, no. 6, pp. 2998–3009, June 2004.

[11] T. Varslot, E. Mo, H. Krogstad, and B. Angelsen, "Eigenfunction analysis of stochastic backscatter for characterization of acoustic aberration in medical ultrasound imaging," *J. Acoust. Soc. Am.*, vol. 115, no. 6, pp. 3068–3076, June 2004.

[12] G. Casella and R. Berger, *Statistical Inference*, 1st ed. California: Duxbury, 1990.

[13] J. M. Fortes, "A closed loop ml algorithm for phase aberrration correction in phased array imaging systems - part I: Algorithm synthesis and experimental results," *IEEE Trans. Ultrason. Ferroelectr. Freq. Control*, vol. 44, no. 2, pp. 259–270, 1997.

[14] ——, "A closed loop ml algorithm for phase aberrration correction in phased array imaging systems - part II: Performancs analysis," *IEEE Trans. Ultrason. Ferroelectr. Freq. Control*, vol. 44, no. 2, pp. 259–270, 1997.

[15] J. P. Burg, D. Luenberger, and D. L. Wenger, "Estimation of structured covarianve matrices," *IEEE Proc.*, vol. 70, no. 9, pp. 963–974, 1982.

[16] V. V. Prasolov, *Problems and Theorems in Linear Algebra*. USA: AMS, 1994.

[17] H. Engl, M. Hanke, and A. Neubauer, *Regularization of inverse problems*. Netherlands: Kluwer Academic Publishers, 2000.

[18] G. Strang, *Linear Algebra and its Applications*, 3rd ed. USA: Saunders, 1988.

[19] P. J. M. van Laarhoven and E. H. L. Aarts, *Simulated Annealing: Theory and Applications*. Dordrecht, The Netherlands: Kluwer Academic Publishers, 1987.

[20] M. Mitchell, *An Introduction to Genetic Algorithms*. Cambridge, Mass.: MIT Press, 1996.

[21] R. Mallart and M. Fink, "The van Cittert-Zernike theorem in pulse echo measurements," *J. Acoust. Soc. Am.*, vol. 90, no. 5, pp. 2718–2727, November 1991.

[22] D. L. Snyder, *Random Point Processes*. New York: Wiley, 1975.

[23] R. E. Dorsey and W. J. Mayer, "Genetic algorithms for estimation problems with multiple optima, nondifferentiability, and irregular features," *J. Bus. Econ. Stat.*, vol. 13, pp. 53–66, 1995.

Chapter 7

Iteration of transmit-beam aberration correction

T. Varslot* and S. Måsøy†, B. Angelsen†
*) Dept. Mathematical Sciences, NTNU
†) Dept. Circulation and Imaging, NTNU

Simulations of iterative transmit-beam aberration correction using a time-delay and amplitude filter have been performed to study the convergence of such a process. Aberration in medical ultrasonic imaging is usually modelled by arrival-time and amplitude fluctuations concentrated on the transducer array. This is an approximation of the physical aberration process, and may be applied to correct the transmitted signal using a time-delay and amplitude filter. Estimation of such a filter has proven difficult in the presence of severe aberration. Presented here is an iterative approach, whereby a filter estimate is applied to correct the transmit-beam. This beam induces acoustic backscatter better suited for arrival-time and amplitude estimation, thus facilitating an improved filter estimate. Two correlation-based methods for estimating arrival-time and amplitude fluctuations in received echoes from random scatterers were employed. Aberration was introduced using eight models emulating aberration produced by the human abdominal wall. Results show that only a few iterations are needed to obtain corrected transmit-beam profiles comparable to those of an ideal aberration correction filter. Furthermore, a previously developed focusing criterion is found to quantify the convergence accurately.

I Introduction

Aberration in medical ultrasound imaging is observed as reduced resolution in the images. It is mainly produced by spatial variation of acoustic parameters (mass density and bulk compressibility) in the human body wall. The loss of resolution may, in many situations, render a reliable diagnosis based on these images difficult to obtain. Extensive research has therefore been carried out in order to solve this problem.

Iteration of transmit-beam aberration correction is defined as a process where a set of aberration parameters is estimated; the estimated parameters are used for correcting the transmitted ultrasound beam; and a new estimate of the same parameters is calculated. This process is then repeated. The parameters are typically arrival-time or arrival-time and amplitude fluctuations. Iteration of transmit-beam aberration correction is sometimes referred to as adaptive imaging or auto-focusing, but these terms are also used to denote aberration correction in general.

In the presented work, iteration of transmit-beam aberration correction is studied. This process is abbreviated *transmit-beam iteration* in the remainder of the article.

Flax and O'Donnell[1,2] studied transmit-beam iteration using estimated arrival-time differences between neighbour elements on the receiving array. They considered aberration from a thin phase-screen just in front of the array. Using such aberration, a transmit-beam iteration process for correcting the phase of the transmit signal using time-delays estimated from neighbour correlation, was argued to be a process that inherently converges to an ideal transmit-focus.

In Refs. 3 and 4 the morphology of the abdominal wall was studied. It was found that a single time-delay or phase-screen is not adequate for modelling aberration of the ultrasound wave. This is due to the fact that aberration consists of both phase and amplitude aberration, and that these effects occur throughout the whole thickness of the body wall.[4] In this situation, the arguments of Flax and O'Donnell[2] are not sufficient. In Ref. 5 it was shown that an appropriate time-delay and amplitude filter can produce close-to-ideal correction. It has yet to be shown that iterative transmit-beam aberration correction based on estimating a time-delay and amplitude filter from random scatterers will yield a similar correction.

In Refs. 6,7,8 transmit-beam iteration was performed using different methods for aberration correction, but no consistent measure of convergence was introduced. In Ref. 6 several iterations were performed in order to estimate phase aberrations only. The efficiency of the correction was evaluated using the root-mean-square (rms) difference between the estimated phase and a reference phase, where the reference was obtained from a beacon signal (point source). In many practical situations such a beacon signal is not available. This metric is therefore not useful for evaluating convergence of transmit-beam iteration in most imaging situations.

Rigby *et al.*[9] performed *in vivo* transmit-beam iteration using time-delays with a 1.75D array. They used a beamsum-channel correlation method for estimating arrival-time fluctuations and found the algorithm to converge after three or four iterations. The results obtained showed improved image quality, but it is not certain to what the algorithm converged as no reference values could be obtained from the subjects investigated.

Other authors have also described transmit-beam iteration,[10,11,12,13,14] but only performed aberration correction on either the received signal, or on the transmitted and the received signal. No further iterations were carried out.

In order to obtain qualitative data concerning the convergence of a transmit-beam iteration process, two aberration estimation methods are compared in this article. Both methods estimate arrival-time and amplitude fluctuations using signals from random scatterers. The estimated arrival-time and amplitude fluctuations are then used as a matched filter for time-delay and amplitude aberration correction.

The first estimation method correlates each element signal with a reference signal. The reference signal is a weighted and modified beamformer output of the received signal.[15] The second method uses an eigenfunction decomposition of the cross-spectrum to maximise the expected energy in the received signal.[16]

In order to evaluate the quality of an aberration correction method, Mallart and Fink developed a focusing criterion based on the van Cittert-Zernike theorem.[11] An analogous criterion was developed by Liu and Waag.[10] Lacefield and Waag[14] discuss the utility of this focusing criterion since the van Cittert-Zernike theorem is only valid for propagation in a homogeneous medium. The width of the average receive coherence function at different levels was suggested as an alternative measure to evaluate an aberration correction method. A monotonic relation between the coherence widths and the effective widths of point spread functions was observed in single-transmit images.

Both of these measures are used in this article, in order to evaluate the convergence of the transmit-beam iteration process. The process is also evaluated by comparing arrival-time and amplitude fluctuation estimates to those obtained from point source simulations. A simulation with a point source in the focus of the array provides an optimal situation for observing aberration of the ultrasound wave, and serves as a good reference.

Absorption effects, electronic noise and acoustic reverberation noise were not included in the simulations.

II Theory

II.A Signal and aberration correction modelling

Following Angelsen[17] (Ch. 11), the aberration is modelled by relating the Green's function for the wave equation with constant coefficients to the Green's function for the wave equation with spatially variable coefficients using a filter denoted the *generalised frequency-dependent screen*. The frequency response of this filter describes the aberration introduced to each frequency component of the signal.

If the generalised frequency-dependent screen is independent of the position in space at which the backscatter was created, the signal received at array coordinate $\mathbf{r}_a$ can be written as[15]

$$y(\mathbf{r}_a;\omega) = s(\mathbf{r}_a;\omega)\ f(\mathbf{r}_a;\omega)\ . \tag{7.1}$$

The function $f(\mathbf{r}_a;\omega)$ is an integral over a volume containing scatterers distributed in space, and represents the unaberrated acoustic backscatter signal. It does, however, depend on the transmitted beam, and is thus a function of the transmit aberration.

The situation where aberration on an array element satisfies the assumption of being independent of the spatial position of the scatterer, is denoted *scatterer-independent aberration*.[15] This can be viewed as concentrating all aberration of the inhomogeneous medium to a layer at the array surface. For an extended aberrator of varying thickness, this assumption is generally not satisfied, but may be a good approximation within a region surrounding the focal point; *the isoplanatic patch*. A received signal according to Eq. (7.1) is thus obtained by focusing the transmitted beam to the inside of the isoplanatic patch.

The two aberration estimation methods employed in this article perform aberration correction using a time-delay and amplitude correction filter with transfer function

$$h(\mathbf{r}_a;\omega) = a(\mathbf{r}_a)\ e^{i\omega\tau(\mathbf{r}_a)}. \tag{7.2}$$

The time-delay τ, and amplitude a, are functions of the array coordinate $\mathbf{r}_a$, but do not depend on frequency. This approximation of the correction filter is valid for band-limited signals assuming scatterer-independent aberration.

It has been shown that a time-delay and amplitude filter produces close-to-ideal correction (no aberration), if correct estimates for the arrival-time and amplitude fluctuations are obtained, even in the case of severe aberration.[5]

II.B Scatterer-independent aberration

When the scatterers are randomly distributed in space, the backscatter signal is a stochastic variable. Assuming scatterer-independent aberration, the cross-spectrum between the received signal at location $\mathbf{r}_p$ and $\mathbf{r}_n$ on an array may be expressed using

Eq. (7.1)

$$R(\mathbf{r}_p, \mathbf{r}_n) = s(\mathbf{r}_p) s^*(\mathbf{r}_n)\ F(\mathbf{r}_p, \mathbf{r}_n). \tag{7.3}$$

Here $F(\mathbf{r}_p, \mathbf{r}_n)$ is the cross-spectrum of the backscatter signal without aberration. Dependence on frequency has been omitted for notational convenience.

In Ref. 18 the van Cittert-Zernike theorem was developed for incoherent acoustic backscatter and propagation through a homogeneous medium. If the aberration is scatterer-independent, the van Cittert-Zernike theorem may be applied. In this case, $F(\mathbf{r}_p, \mathbf{r}_n) = F(\mathbf{r}_p - \mathbf{r}_n) \equiv F(\boldsymbol{\xi})$ is computed as [17] (pp. 11.55)

$$F(\boldsymbol{\xi}) = \frac{\sigma_v^2}{4\pi^2} \int_{S_a} s(\mathbf{r}+\boldsymbol{\xi}) s^*(\mathbf{r}) o(\mathbf{r}+\boldsymbol{\xi}) o^*(\mathbf{r}) \mathrm{d}\mathbf{r}. \tag{7.4}$$

Here σ_v^2 is the scattering intensity, the integration is performed over the array surface S_a, and $o(\mathbf{r})$ denotes the array apodisation function.

Equation (7.4) shows that the coherence in the received signal is limited by the aberration as well as the apodisation function. This has been experimentally observed, [14] although it was not compared to an explicit theoretical prediction.

III Estimators

In this article two previously developed estimators [15,16] are employed to study transmit-beam iteration. For the convenience of the reader and to introduce notation, the rationale behind both estimators is briefly reviewed. Then the two methods are compared, and new insight into the similarities and differences between them is provided.

Both estimators are based on the cross-spectrum of the received acoustic backscatter. For the purpose of this study, the received signal is assumed to be a Gaussian stochastic process with zero mean value. This implies that all statistical information is contained in the covariance function, or equivalently, the cross-spectrum. For a time-delay and amplitude correction filter as in Eq. (7.2), it is sufficient to consider the cross-spectrum at a single frequency.

For a given frequency ω, the cross-spectrum between the *element signals* $y_p(\omega)$ and $y_n(\omega)$, received at element p and n respectively, is defined as

$$R_{pn} = \mathrm{E}[y_p\ y_n^*]\,. \tag{7.5}$$

Frequency-dependence has been dropped for notational convenience.

For the comparison to be useful, both estimation methods use the same estimate of the cross-spectrum. In order to obtain a proper estimate of the cross-spectrum with low variance, an average over statistically independent backscatter signals is

used. In a practical situation, statistically independent signals can be obtained by imaging scatterers which are replaced between each consecutive transmit-beam, *e.g.* blood or contrast agents. Alternatively, non-overlapping regions of the scatterer distribution may be utilised by combining beams in a linear/sector scan. [6,19]

The estimate of the cross-spectrum is a cross-periodogram given as

$$\tilde{R}_{pn} = \frac{1}{K} \sum_{k=1}^{K} y_{kp} y_{kn}^{*} \,, \tag{7.6}$$

where k denotes received backscatter signals from different random scatterer realisations, and K is the total number of such realisations. To further lower the variance of the estimate in Eq. (7.6), additional averaging over a small band of frequencies is performed which results in a smoothed cross-periodogram.

Reference 20 (pp. 703) shows that the variance of the cross-spectrum estimate in Eq. (7.6) may be found as

$$\begin{aligned} \mathrm{Var}[\, |\tilde{R}_{pn}| \,] &\sim \frac{1}{2K} |R_{pn}|^2 \left(\frac{1}{|w_{pn}|^2} + 1 \right) \\ \mathrm{Var}[\, \angle \tilde{R}_{pn} \,] &\sim \frac{1}{2K} \left(\frac{1}{|w_{pn}|^2} - 1 \right) , \end{aligned}$$

where the coherence w_{pn} is defined as

$$w_{pn} = \frac{R_{pn}}{\sqrt{R_{pp}\, R_{nn}}} \,. \tag{7.7}$$

This implies that the variance of the cross-spectrum is high when the coherence is low and vice versa.

Modified beamformer output - MBFO

This section offers a brief description of the *modified beamformer output* (MBFO) estimator, which was presented in Ref. 15.

The basic premise for this method is that the received signal can be written as in Eq. (7.1), that is, scatterer-independent aberration is assumed. Applying the same discrete notation as in Eq. (7.5) to denote elements p and n in Eq. (7.3), and solving for s_p leads to

$$s_p = \frac{R_{pn}}{F_{pn}} \frac{1}{s_n^{*}}. \tag{7.8}$$

In order to use all possible correlation information to estimate the phase and amplitude of s_p, a weighted average $\hat{s}_p$ is defined

$$\hat{s}_p = \sum_{n=1}^{N} W_{pn} \, \frac{\tilde{R}_{pn}}{F_{pn}} \frac{1}{\hat{s}_n^{*}} \,, \tag{7.9}$$

where N is the total number of elements on the array. Here W_{pn} is a set of weights and $\tilde{R}_{pn}$ is the estimate for R_{pn}.

In this article the weights are chosen as

$$W_{pn} = |\tilde{w}_{pn}|^2 \Big/ \sum_{n=1}^{N} |\tilde{w}_{pn}|^2 \ , \tag{7.10}$$

where $\tilde{w}_{pn}$ is an estimate of the coherence w_{pn} [Eq. (7.7)] based on $\tilde{R}_{pn}$. Thus the estimates of R_{pn} with low variance are emphasised. Furthermore, the phase of F_{pn} is not known, and F_{pn} is therefore replaced by its absolute value. The MBFO estimator $\tilde{s}_p$ is then

$$\tilde{s}_p = \sum_{n=1}^{N} W_{pn} \frac{\tilde{R}_{pn}}{|F_{pn}|} \frac{1}{\tilde{s}_n^*} \ . \tag{7.11}$$

An estimate for $|F_{pn}|$ can be found from the van Cittert-Zernike theorem as formulated in Eq. (7.4).[15]

The estimator in Eq. (7.11) is a set of N coupled nonlinear equations which has to be solved, that is, for $p \in \{1, \cdots, N\}$. An iterative solution method as described in Ref. 15 was utilised for this purpose. The initial estimate for s_p in the iterative solution method was chosen as zero phase and unity amplitude across the array.

Eigenfunction estimator - EFE

The *eigenfunction estimator* (EFE) was presented in Ref. 16. Thus, only a short description of the method is provided here.

Consider the stochastic vector of receive signals at a particular frequency ω and transducer elements indexed from 1 to N

$$\mathbf{y} = [y_1 \ y_2 \ \cdots \ y_N]^{\mathrm{T}}.$$

Given a vector $\mathbf{h} = [h_1 \ h_2 \ \cdots \ h_N]^{\mathrm{T}}$, a stochastic linear functional $\mathscr{L}_h$ may be defined on $\mathbf{y}$ as

$$\mathscr{L}_h \mathbf{y} = \mathbf{h}^{\mathrm{H}} \mathbf{y} = \sum_{p=1}^{N} y_p h_p^*, \tag{7.12}$$

where H denotes the Hermitian of the vector.

The quantity $\mathscr{L}_h \mathbf{y}$ from Eq. (7.12) is the temporal frequency result when a filter with transfer function $h_p(\omega)$ is applied to the signal received at transducer element p before the standard beam-forming procedure is executed. It is a stochastic variable

with associated variance expressed as

$$\begin{aligned} ||\mathscr{L}_h\mathbf{y}||^2 &\equiv \mathrm{E}\left[\mathscr{L}_h\mathbf{y}\left(\mathscr{L}_h\mathbf{y}\right)^{\mathrm{H}}\right] \\ &= \mathbf{h}^{\mathrm{H}}\mathrm{E}\left[\mathbf{y}\mathbf{y}^{\mathrm{H}}\right]\mathbf{h} \\ &= \mathbf{h}^{\mathrm{H}}R\mathbf{h}. \end{aligned} \tag{7.13}$$

Here R is the cross-spectrum matrix of the receive signal at the frequency ω.

The variance is the *expected energy* for $\mathscr{L}_h\mathbf{y}$ at this frequency. Since the matrix R is Hermitian, the expected energy, subject to the constraint $\mathbf{h}^{\mathrm{H}}\mathbf{h} = 1$, is maximised when $\mathbf{h}$ is an eigenvector associated with the largest eigenvalue of R (see Ref. 21, Ch. 6.5).

Through finding the eigenvector which maximises the expression in Eq. (7.13), a match filter which maximises the *speckle brightness*[22] is constructed. The normalisation $\mathbf{h}^{\mathrm{H}}\mathbf{h} = 1$ for each frequency ensures that the correction filter does not alter the frequency distribution for the energy of the aberration-corrected transmit-beam.

The eigenvector $\tilde{\mathbf{h}}$ associated with the largest eigenvalue of $\tilde{R}$ is calculated and used as an estimate of the filter $\mathbf{h}$.

Comparison of the estimators

Both methods estimate aberration from the cross-spectrum of stochastic backscatter. The MBFO estimator also assumes the aberration on a receive element to be independent of the spatial position of the scatterers, *i.e.*, a signal model according to Eq. (7.3). The EFE estimator makes no such assumption.

The MBFO estimator has been shown to be equivalent to correlating the received signal with a correlation reference;[15] a *modified beamformer output*

$$\begin{aligned} \tilde{s}_p &= \frac{1}{K}\sum_{k=1}^{K} y_{kp}\, b_{kp}^{*} \\ b_{kp} &= \sum_n W_{pn}\frac{1}{|F_{pn}|\tilde{s}_n}\, y_{kn}. \end{aligned} \tag{7.14}$$

The modified beamformer output, b_{kp}, is formed by using a weight term W_{pn} and a correction term $1/|F_{pn}|s_n$ for each element signal y_{kn}.

The same interpretation is possible for the EFE

$$\begin{aligned} \tilde{h}_p &= \frac{1}{K}\sum_{k=1}^{K} y_{kp}\beta_k^{*} \\ \beta_k &= \sum_n \frac{1}{\lambda}\tilde{h}_n^{*} y_{kn}. \end{aligned}$$

Equal weight, $1/\lambda$, is placed on all element signals when forming the modified beamformer output β_k. The correction term in this case is h_n^*.

A major difference between the two estimators is that the correction term for the MBFO estimate is obtained by applying the aberration correction filter as an inverse filter, while the correction for the EFE is obtained by matched filtering. In addition, the MBFO estimator utilises a different set of weights for each transducer channel p, thus obtaining a different correlation reference signal for each channel. The EFE estimator makes use of the same correlation reference for all channels.

To compare the estimators further, it is instructive to consider the case where $F_{pn} = |F_{pn}|$. This will be the case when, for example, the scattering medium is incoherent and all phase aberration of the transmitted beam has been corrected.

Let S be the diagonal matrix

$$S = \begin{pmatrix} s_1 & & \\ & \ddots & \\ & & s_N \end{pmatrix}.$$

Equation (7.13) is then reformulated as

$$\begin{aligned} ||\mathscr{L}_h \mathbf{y}||^2 &= \mathbf{h}^{\mathrm{H}} R \mathbf{h} \\ &= \mathbf{h}^{\mathrm{H}} S F S^{\mathrm{H}} \mathbf{h}, \end{aligned} \tag{7.15}$$

where F is the cross-spectrum matrix for the unaberrated acoustic backscatter. Therefore, $S^{\mathrm{H}}\mathbf{h}$ must be an eigenvector of F. Now, since F is real, then the eigenvector $S^{\mathrm{H}}\mathbf{h}$ is real as well. In this case the phase of h_p is equal to that of s_p; the phase estimated by the EFE will be an unbiased estimate for the phase of the screen.

Furthermore, it is easy to see that if $\mathbf{h}$ is an eigenvector of R with eigenvalue λ, then

$$h_p = \frac{1}{\lambda} \sum_n R_{pn} h_n = \sum_n \frac{|F_{pn}||h_n|^2}{\lambda} \frac{R_{pn}}{|F_{pn}|} \frac{1}{h_n^*}. \tag{7.16}$$

The EFE therefore satisfies an equation of the same type as Eq. (7.11) for the MBFO, with weights $W_{pn} = |F_{pn}||h_n|^2/\lambda$.

If the weights W_{pn} in Eq. (7.11) are required to satisfy $\sum_n W_{pn} = 1$, then the MBFO will be an unbiased estimate for the screen.[15] However, for the EFE this requirement is not necessarily fulfilled. The result is a biased estimate of the amplitude.

Express the amplitude bias in a multiplicative fashion

$$h_p = \alpha_p s_p,$$

where α_p is real and positive, and s_p, as previously, denotes the screen. Inserting this into Eq. (7.16) yields

$$s_p = \sum_n \frac{|F_{pn}||s_n|^2 \alpha_n}{\lambda \alpha_p} \frac{R_{pn}}{|F_{pn}|} \frac{1}{s_n^*}.$$

The fact that a normalised set of weights will obtain an unbiased estimate for the screen implies that the amplitude bias may be expressed as a solution to

$$\alpha_p = \sum_{n=1}^{N} \frac{|F_{pn}||s_n|^2}{\lambda} \alpha_n. \tag{7.17}$$

Because of the Toeplitz structure of F, and the fact that $|F_{pn}|$ decreases off the main diagonal, any solution α_p of Eq. (7.17) will decrease as a function of p when p moves towards the edges of the array. If $|F_{pn}|$ decreases monotonically, then α_p will also decrease monotonically from a maximum in the central region of the array. The filter amplitude is therefore an estimate for an apodised version of the screen amplitude. This apodisation has previously been discussed,[16] but the expression for the apodisation is new.

In general, when F is not real, the relationship between h_p and s_p is more complicated. It is, however, possible to show that an iterative transmit-beam aberration correction procedure will converge to a h_p which has a phase that concurs with the screen.[16] Applying the correct phase for aberration correction will result in a F which satisfies $F_{pn} = |F_{pn}|$. The preceding argument may then be used to assert that an apodised amplitude estimate is also obtained.

By omitting the phase of F_{pn}, an error is introduced in the MBFO estimate of the screen. Equation (7.9) can be written as

$$\hat{s}_p = \sum_{n=1}^{N} W_{pn} \frac{\tilde{R}_{pn}}{|F_{pn}|} \frac{e^{-i\Delta_{pn}}}{\hat{s}_n^*}, \tag{7.18}$$

where Δ_{pn} is the phase of F. Neglecting this phase will, in general, contribute both to a phase and an amplitude error in the estimation of $\tilde{s}_p$ from Eq. (7.9). Assuming the transmit-beam iteration process converges to the true phase of s_p, as discussed above, F will be real valued and $\hat{s}_p$ becomes by definition equal to $\tilde{s}_p$.

Arrival-time and amplitude estimates

After obtaining an estimate at the centre angular frequency, ω_0, for the scatterer-independent screen s_p and the energy maximising filter h_p using the MBFO and the EFE estimator respectively, arrival-time and amplitude fluctuations were calculated in a standard way.[15]

Note that although in the presented work only arrival-time and amplitude fluctuations were used, both the MBFO and the EFE may be employed to estimate a phase and amplitude aberration correction filter for all frequency components in the signal.

IV Simulations

The simulations presented in this article were performed using the two-dimensional (2D) simulation setup shown in Fig. 7.1. An angular spectrum operator was used for homogeneous propagation of the simulated signals.[5] A beam was propagated from the transducer through a body wall model to the scattering region. There it was scattered according to the Born approximation and propagated back to the transducer.

Eight body wall models were generated using equally spaced time-delay screens, filtered and tuned to obtain characteristics according to abdominal wall measurements.[23] The body wall models were also used in Ref. 5. A thorough description of

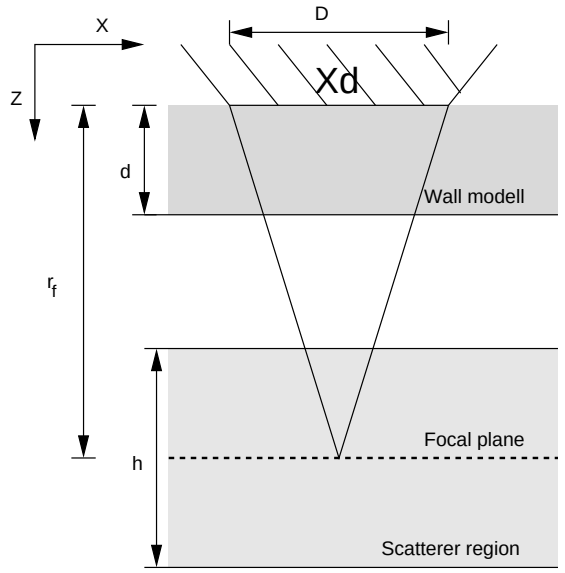

Figure 7.1: An ultrasound pulse was propagated from the transducer (xd), through a body wall to a scattering region. Scattering was computed according to the Born approximation and propagated back through the body wall to the transducer.

the body wall models is offered in this reference.

The point source simulations were of a one-way nature: a point source was situated at the position of maximum energy of the transmitted beam in the focal plane for each of the aberrators. An emitted pulse from the source, identical to the transmit pulse from the array, was propagated to the array and processed to obtain a reference for the arrival-time and amplitude fluctuations.

IV.A Simulation parameters and data processing

The simulations were implemented in MATLAB. The simulation domain was 10.24 cm in the lateral direction (x-direction in Fig. 7.1) with a resolution of 0.2 mm. To avoid reflections at the edges of the spatial domain due to the FFT being periodic, the signal was tapered to zero with a raised cosine window over a 2.54 cm-wide band. The sampling frequency was 35.1 MHz providing a time window of 58.3 µs. The transmitted pulse had a centre frequency of 2.5 MHz and a -6 dB bandwidth of 1.5 MHz. An array aperture size of 20 mm with point-like elements was chosen. The focal depth of the array was set to 60 mm. The medium through which the signals were propagated had a speed of sound equal to that of water; 1523 m/s. Geometric focusing was removed from all received signals prior to further processing of the results.

To generate a realistic speckle signal, an area of 30.5 mm (time window of 20 µs), centred with 15.25 mm to each side of the focal plane was used as a scattering region (see Fig. 7.1). The scatterer density was approximately 1600 scatterers per square centimetre. The scatterers were uniformly distributed in space, and had a Gaussian distributed reflection strength.

For each transmit-beam iteration, scattering from twenty independent realisations of the scattering region were simulated for the purpose of cross-spectrum estimation.

Estimation of arrival-time fluctuations for the point source simulation was performed with a phase front tracking algorithm.[5] The method has proved to yield accurate estimates of the wavefront, and is not sensitive to waveform deformation which occurs behind the wavefront.

For all arrival-time fluctuation estimates presented in this article, a linear fit was subtracted in order to remove refraction steering of the beam.

Amplitude fluctuations from the point source simulations were determined by taking the Fourier transform of the received signal on each element as a function of time. The amplitude on each element of the array was calculated as the arithmetic mean of the amplitudes of the now frequency-dependent signal, over a band of frequencies ranging from 2-3 MHz. This band was chosen empirically.

In order to evaluate the accuracy of the estimation methods, the relative L^2 distances between arrival-time and amplitude estimates and their respective references obtained from the point source simulations were calculated. The L^2 distance was

normalised with respect to the L^2 norm of the reference, and was thus calculated as

$$d(x, x_{\text{ref}}) = \sqrt{\sum_{i=1}^{N} |x_i - x_{i,\text{ref}}|^2} \Bigg/ \sqrt{\sum_{i=1}^{N} |x_{i,\text{ref}}|^2} \, .$$

Here x is the arrival-time or amplitude estimate, and x_{ref} is the reference value obtained from the point source simulations. The mean value was subtracted from all estimates prior to the calculation of the L^2 distance.

For the comparison to be useful, the amplitude estimates and the point source reference need to have equal power. Assuming the estimated values for the amplitude fluctuations are proportional to the reference, a gain factor α may be defined as

$$\hat{\mathbf{a}} = \alpha \mathbf{a}.$$

Here $\hat{\mathbf{a}}$ is the estimate and $\mathbf{a}$ the point source reference. The gain factor was determined by minimising the error between the reference and the estimate

$$\alpha = \frac{\hat{\mathbf{a}}^T \mathbf{a}}{\mathbf{a}^T \mathbf{a}} \, .$$

To ensure equal power, the estimated arrival amplitudes were then scaled using the gain factor, prior to the calculation of the relative L^2 distance.

The focusing criterion was calculated according to the derivations by Mallart and Fink.[11] They defined a focusing criterion as

$$C = \frac{\int_{-\infty}^{+\infty} \left(\sum_{p=1}^{N} y_p(t - \tau_p) \right)^2 \mathrm{d}t}{N \cdot \sum_{p=1}^{N} \int_{-\infty}^{+\infty} y_p^2(t) \mathrm{d}t} \quad ,$$

where N is the number of elements on the receiving array. Liu and Waag[10] independently proposed a similar criterion denoted the *waveform similarity factor*.

For a point source, the value of C lies between 0 and 1. For an incoherent medium Mallart and Fink showed that the maximum value of C is 2/3. Note that C can only attain its maximum value if τ_p is properly estimated.

The focusing criterion was, as described earlier, used to evaluate the convergence of the iterative aberration correction procedure, along with the widths of the average receive coherence function introduced by Lacefield and Waag.[14]

The average coherence function for the received signal, from now on denoted *coherence function*, was calculated as

$$\overline{w}_{p-n} = \frac{1}{N_\Delta} \sum_{N_\Delta} \tilde{w}_{pn} = \frac{1}{N_\Delta} \sum_{N_\Delta} \frac{\tilde{R}_{pn}}{\sqrt{\tilde{R}_{pp} \, \tilde{R}_{nn}}} \, ,$$

where N_Δ denotes the number of element pairs with separation $p-n$. Note that the coherence function was only calculated for the centre frequency of the signal. The magnitude of the coherence function was interpolated to a resolution of 0.05 mm sampling, before the width of the magnitude of the coherence function was calculated at levels 0.6 and 0.4.

All received data were corrected using arrival-time fluctuation estimates, obtained by the estimators, prior to the calculation of the focusing criterion C and the coherence function. For the focusing criterion, the linear fit of the arrival time estimates was not subtracted prior to receive correction.

Beam profiles in the focal plane of the array were acquired as the rms value of the temporal signal at each spatial position. These profiles were used for the visual evaluation of the effect of the different aberration correction methods.

V Results

Simulations were performed using eight different aberrators. To limit the amount of data presented, detailed results are only offered for two of the aberrators; w6 and s6. The w6 and s6 aberrators represent weak and strong aberration respectively, and are representative for overall performance of the iterative transmit-beam aberration correction. Only the parameter C is presented for all aberrators, as this proved to be the best criterion by which to quantify the transmit-beam iteration results.

In all the results presented, MBFO and EFE denote results obtained using the corresponding method for estimating arrival-time and amplitude fluctuations.

All results in this section are labelled with an iteration number. The iteration number is defined according to the transmit-beam. One transmit-beam iteration is defined as consisting of an estimation of arrival-time and amplitude fluctuations; an application of these estimates to a transmit-beam in order to obtain a corrected transmit-beam profile; and finally, receiving scattering generated by the corrected transmit-beam. In this labelling scheme, *iteration 0* refers to the initial transmit-beam, where no aberration correction is applied. The arrival-time and amplitude fluctuations estimated using scattering created by the transmit-beam from iteration 0 are used to form the first truly corrected transmit-beam. These arrival-times, amplitudes, and the resulting beam profiles are thus labelled *iteration 1*, and so on.

Figure 7.2 shows beam profiles in the focal plane of the array. For the w6 aberrator, the corrected beam profiles appear to converge after two iterations for both methods. The resulting beam profiles are very well corrected and close to the unaberrated profile. In the case of the s6 aberrator, one additional iteration is required for MBFO to obtain the same results. Since only minor changes occur from iteration 2 to iteration 5 for the w6 aberrator, and from iteration 3 to iteration 5 for the s6 aberrator, only results from iterations 0, 1, 2 and 5 are presented.

The estimated time-delay and amplitude fluctuations used to produce the corrected beam profiles in Fig. 7.2 are shown in Figs. 7.3 and 7.4. The visual impression of convergence for the estimates is the same as for the beam profiles. It is worth noting, however, that the time-delay estimate is also very accurate after two iterations for MBFO applied to the s6 aberrator. The amplitude improves significantly at the third iteration. The improvement between iterations 2 and 3 for the beam profile is thus mainly explained by an improved amplitude estimate.

The relative L^2 distance between the estimated arrival-time/amplitude and the respective references was computed for each iteration. Figure 7.5 shows how the distance decreases for the first two iterations. In the case of the w6 aberrator the distances level out after the second iteration. For the s6 aberrator, the distance for the amplitude levels out in the same manner as for the w6 aberrator. The distance for the arrival-time, however, increases after the second iteration. This is related to the discontinuities in the arrival-time estimates observed in Fig. 7.3. The value at which the L^2 distance levels out for the EFE amplitude estimate is significantly higher than for the MBFO estimate. This is explained by the fact that the EFE amplitude is apodised relative to the screen, while the MBFO is not.

The magnitude of the coherence functions, and the coherence widths for the received scattering, are presented in Figs. 7.6 and 7.7. The coherence widths at different levels increase gradually with iteration, demonstrating an increased degree of spatial coherence in the receive signal.

The focus quality parameter for all aberrators is presented in Figs. 7.8 and 7.9 as a mean value and a standard deviation. These were calculated using the twenty independent receive signals for each iteration. In concurrence with the theoretical foundation for the parameter,[11] the strong increase in the focus quality parameter C corresponds to the improved focus apparent in the beam profiles in Fig. 7.2. With the exception of s8, convergence was obtained after 1-3 iterations using either algorithm.

VI Discussion

As shown in this article, both the MBFO and EFE algorithm use an average of element signals as the reference value in a correlation process, in other words, a beam-forming correlation process. This is conceptually similar to the speckle brightness method,[22] speckle look-back,[12] the beamsum-channel correlation method,[9] and the scaled covariance matrix algorithm[24] for phase estimation. The principal difference is that both methods presented here can estimate both phase and amplitude aberration at all frequency components, and thus represent a generalisation of the methods described above.

In order to obtain a correlation-based estimate, a stable reference signal is needed. The variance of the estimate will be as low as possible when the reference signal is coherent with the backscatter signal. In the case of the MBFO estimator, a separate

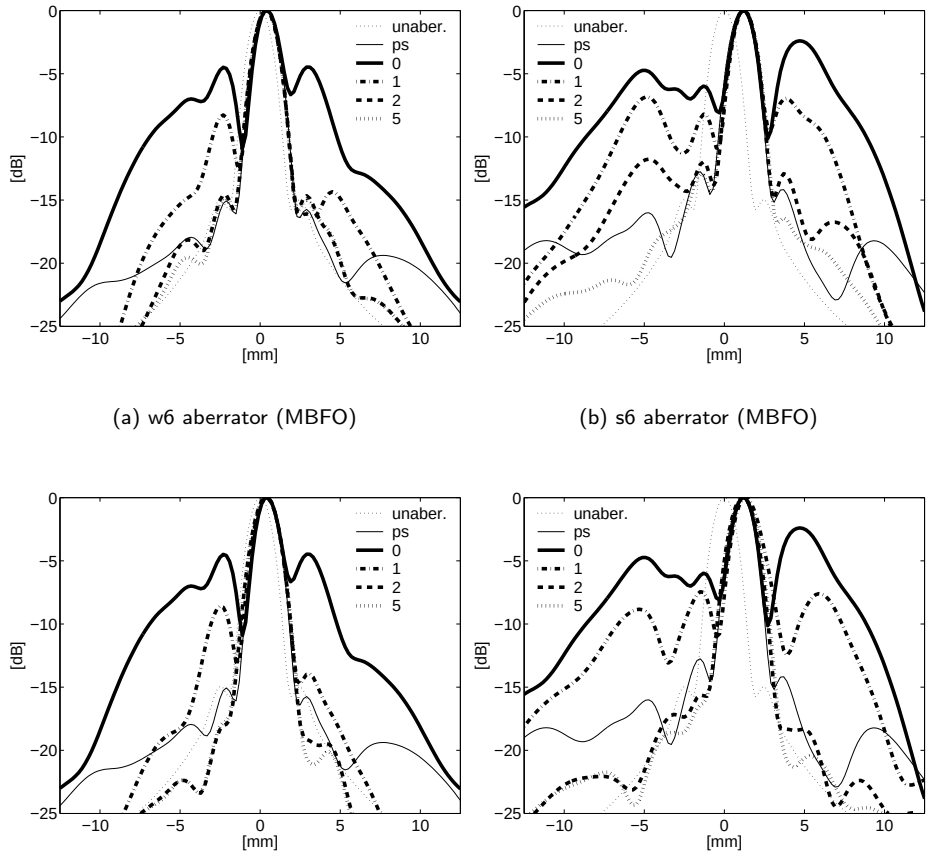

(a) w6 aberrator (MBFO)

(b) s6 aberrator (MBFO)

(c) aberrator (EFE)

(d) s6 aberrator (EFE)

Figure 7.2: Beam profiles in the focal plane for the w6 and s6 aberrators. Zero on the horizontal axis represents the centre axis of the array. All profiles are normalised to their maximum value. The reference profile represents the situation with no aberration, and the profile denoted ps shows correction using the point source reference. The numbers in the legend refer to the iteration number of the correction procedure, where the 0-iteration profile is the uncorrected transmitted profile.

reference b_{kp} is used for each element p. The EFE, on the other hand, uses the same reference, β_k, for all elements.

The MBFO estimate utilises the signal model to create signals of equal strength at

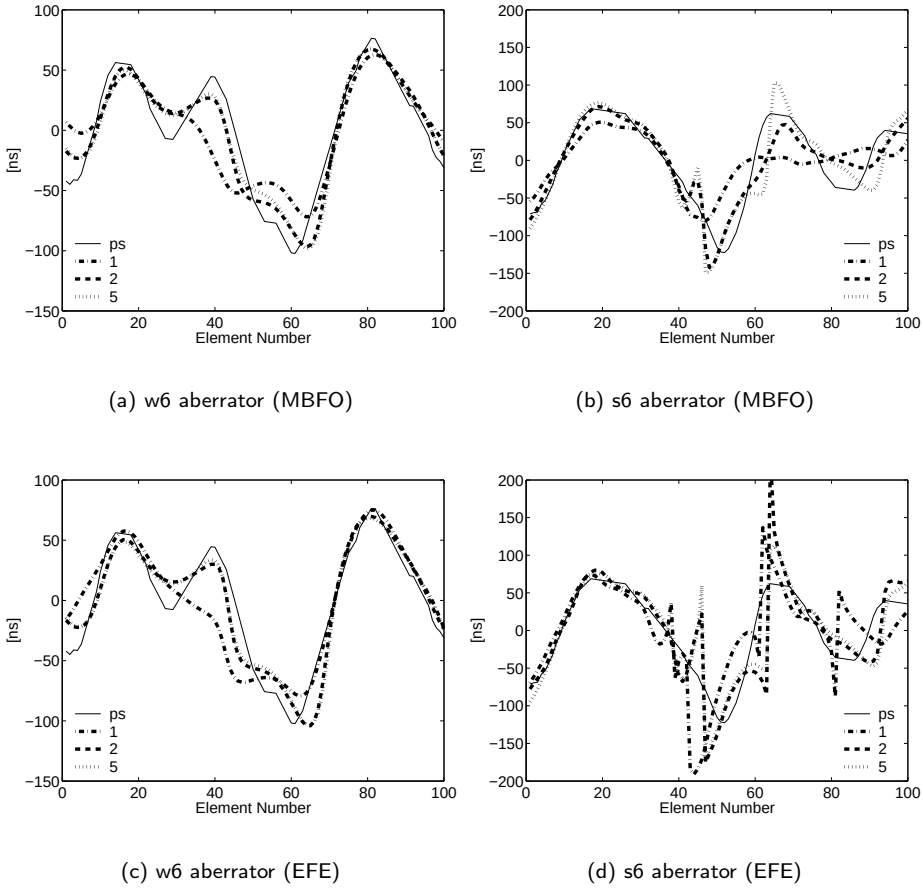

(a) w6 aberrator (MBFO)

(b) s6 aberrator (MBFO)

(c) w6 aberrator (EFE)

(d) s6 aberrator (EFE)

Figure 7.3: Arrival-time fluctuations for the w6 and s6 aberrators. The horizontal axis is given in array elements. The curves denoted ps are the references obtained from the point source simulations. The numbering of the arrival-time curves in the legend corresponds to the iteration number of the corrected transmitted beam in Fig. 7.2. Arrival-time curve number 1 was thus used to obtain beam profile number 1 in Fig. 7.2.

each element by factoring out the effect of the aberration amplitude. It then forms a reference which is coherent with the signal at element p by explicitly applying the coherence function as weights in a weighted average.

The weight function works as a sliding window which efficiently implements a sub-aperture processing, automatically selecting an appropriate sub-aperture for the

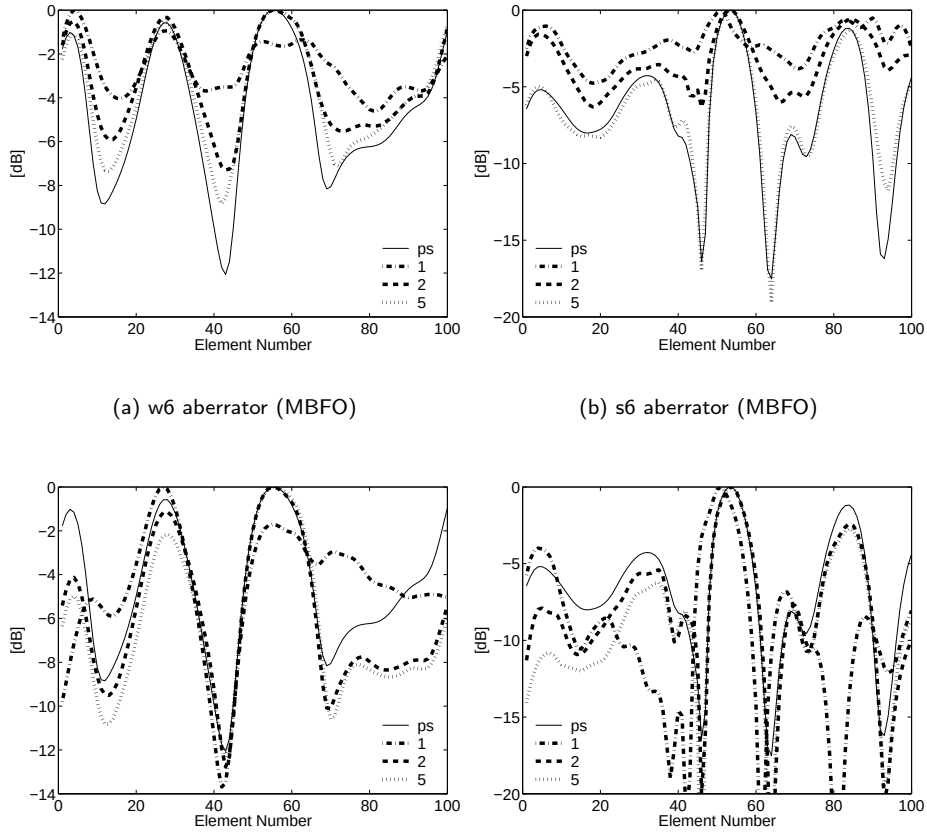

(a) w6 aberrator (MBFO)

(b) s6 aberrator (MBFO)

(c) w6 aberrator (EFE)

(d) s6 aberrator (EFE)

Figure 7.4: Amplitude fluctuations for the w6 and s6 aberrators. The horizontal axis is given in array elements. The curves denoted ps are the references obtained from the point source simulations. All amplitude fluctuation curves are normalised to their maximum value. The numbering in the legend is the same as in Fig. 7.3.

beamformer output from a variance perspective [confer Eq. (7.14)]. The weighting also ensures that the beamformer output is highly correlated with the element signal where the estimation occurs. Since the sub-aperture slides across the array, it is desirable to employ an inverse amplitude filtering in order for the reference signal to attain the same average energy level for each sub-aperture.

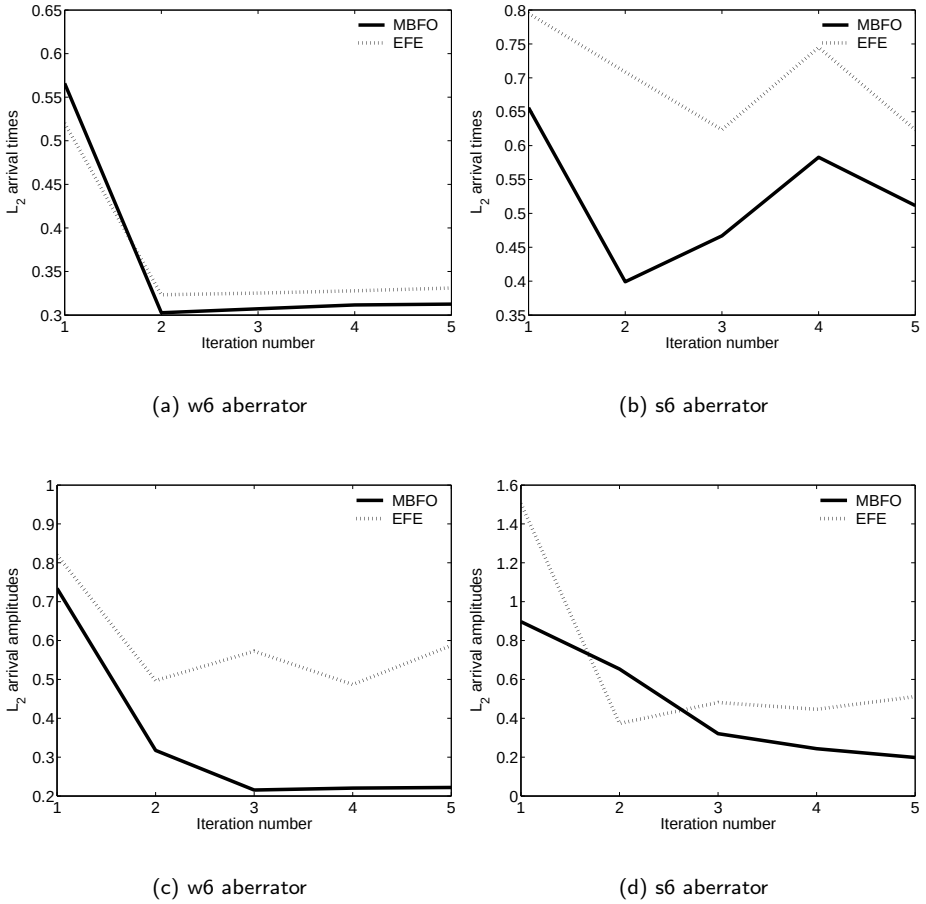

Figure 7.5: Relative L^2 distance between point source reference and estimate for w6 and s6 aberrators. The top row shows the L^2 distance for arrival-time fluctuations, and the bottom row for amplitude fluctuations. The horizontal axis indicates the iteration number according to Figs. 7.3 and 7.4.

The EFE constructs one signal which is utilised as a common correlation reference for all element signals across the aperture. To this end, no signal model is employed directly. Instead, the reference signal is formed as a weighted coherent sum of the element signals. Assuming no amplitude damping due to absorption, a backscatter signal of large amplitude is the result of constructive interference. A low-amplitude

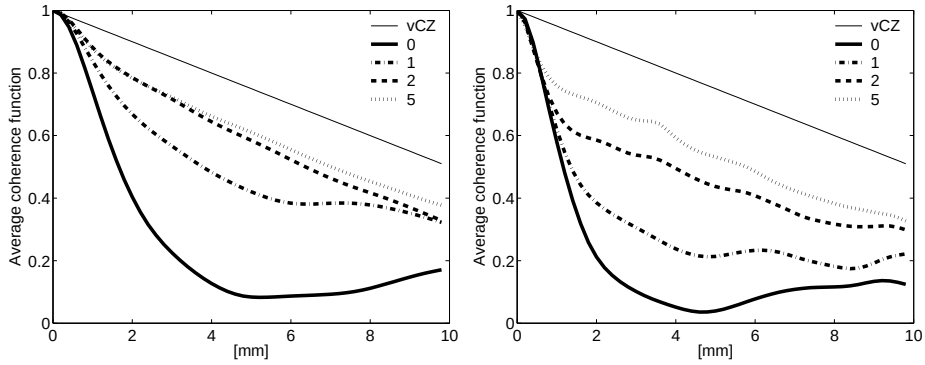

(a) w6 aberrator (MBFO)

(b) s6 aberrator (MBFO)

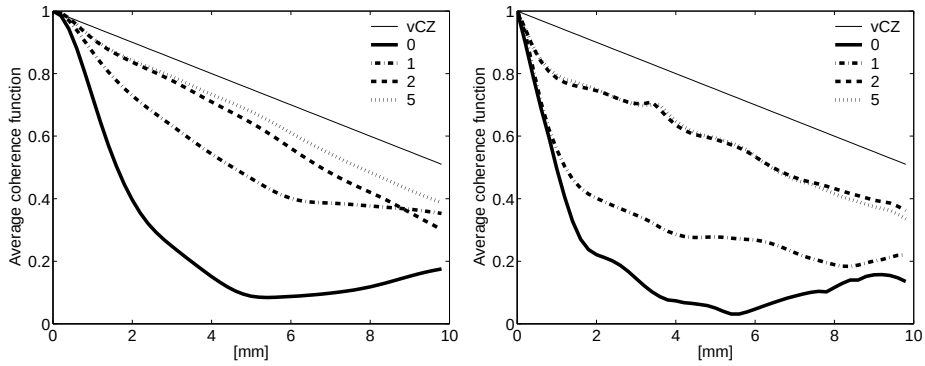

(c) w6 aberrator (EFE)

(d) s6 aberrator (EFE)

Figure 7.6: Absolute value of the average coherence function for the w6 and s6 aberrators. The numbering of the curves corresponds to the iteration number, *i.e.* coherence functions for the received signals obtained using a transmit-beam with the same number in Fig 7.2. The curve denoted vCZ indicates the theoretical upper bound for the coherence based on the van Cittert-Zernike theorem for a homogeneous medium. All received signals were corrected using the estimated arrival-time fluctuations prior to calculating the coherence function.

backscatter signal, on the other hand, is the result of destructive interference. As a result, high-amplitude signals will resemble each other more closely than low-amplitude signals. The accuracy with which the aberration correction filter may be

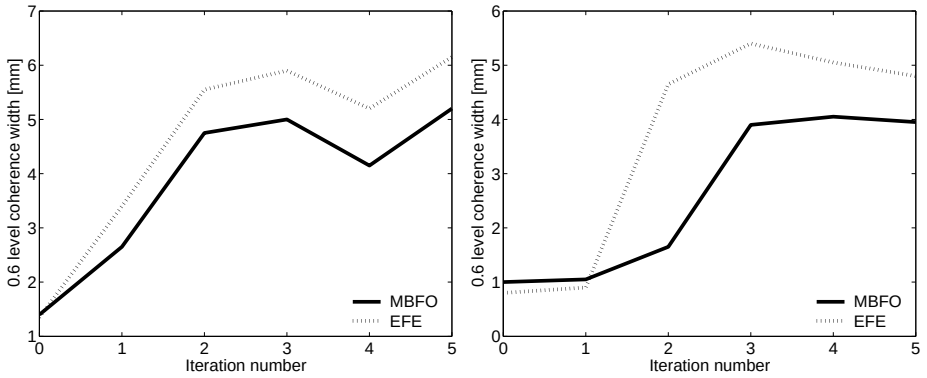

(a) w6 aberrator

(b) s6 aberrator

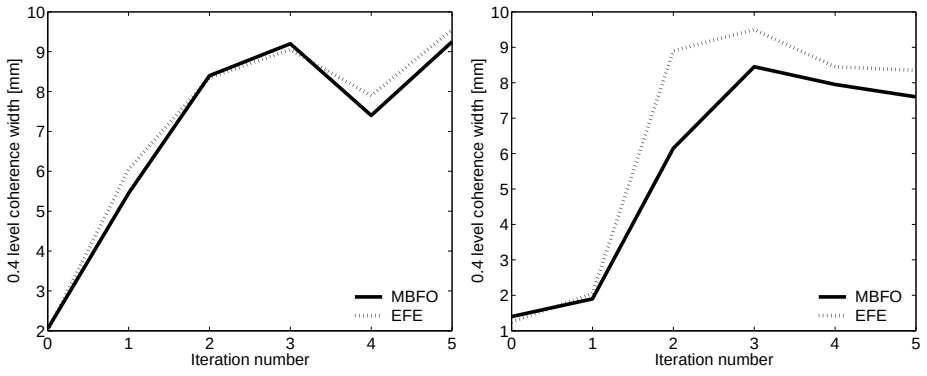

(c) w6 aberrator

(d) s6 aberrator

Figure 7.7: Coherence widths for the w6 and s6 aberrators at levels 0.6 and 0.4. The horizontal axis shows the iteration number as explained in Fig. 7.6.

estimated, is directly connected to the degree of coherence between an element signal and the reference. In order to form a good estimate, it is therefore of importance to form a reference signal which is highly correlated with the element signals. Furthermore, because signals of high amplitude contribute more to the overall focus quality than low-amplitude signals, it is most important to obtain an accurate estimate for the correction of high-amplitude signals. The weighted coherent sum

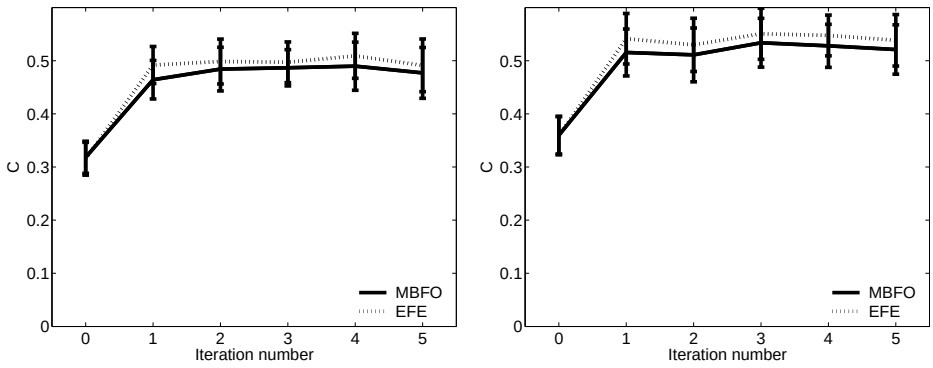

(a) w2 aberrator

(b) w4 aberrator

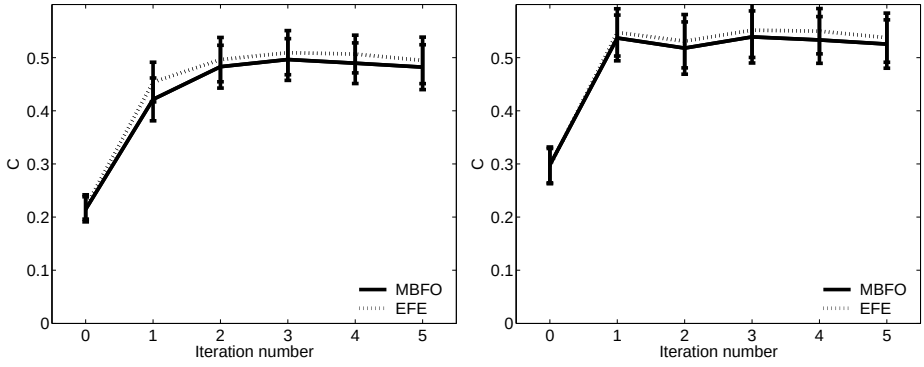

(c) w6 aberrator

(d) w8 aberrator

Figure 7.8: Mean value and standard deviation of the focus quality parameter C computed for all wall models w2, w4, w6 and w8. The horizontal axis shows the iteration number as explained in Fig. 7.6. The error bars display the standard deviation. All received signals were corrected using estimated arrival-time fluctuations prior to calculation of the focusing criterion.

of element signals should emphasise element signals of large amplitude in order to achieve this. To what degree high amplitudes should be emphasised over low amplitudes is determined by the L^2 norm used when maximising the expected energy of $\mathscr{L}_h\mathbf{y}$ in Eq. (7.12).

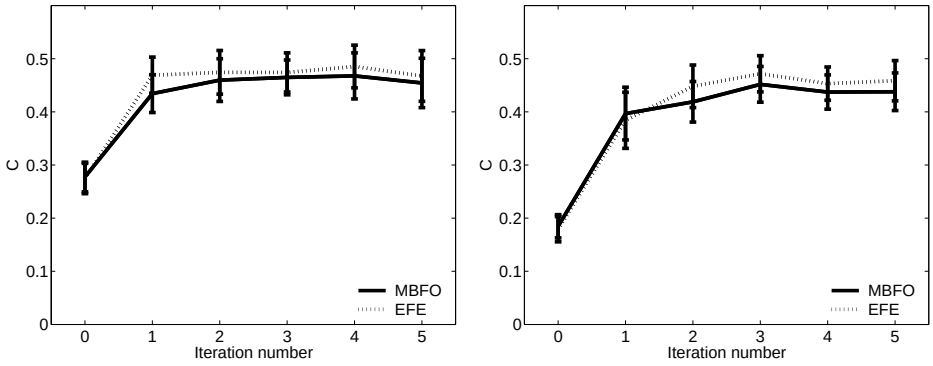

(a) s2 aberrator (b) s4 aberrator

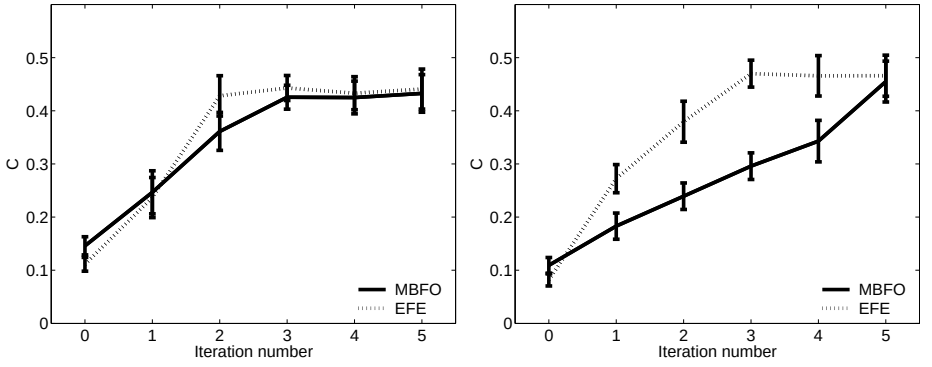

(c) s6 aberrator (d) s8 aberrator

Figure 7.9: Mean value and standard deviation of the focus quality parameter C computed for all wall models s2, s4, s6 and s8. The horizontal axis shows the iteration number as explained in Fig. 7.6. The error bars display the standard deviation. All received signals were corrected using estimated arrival-time fluctuations prior to calculation of the focusing criterion.

As described in Sec. IV.A, for each transmit-beam iteration, scattering from twenty new realisations of the scattering region was simulated. The objective of this article was to study iteration of transmit-beam aberration correction. For this purpose, a proper estimate of the cross-spectrum [Eq. (7.6)] was desired. For practical purposes,

using twenty transmit-beams for each estimate is unfeasible in a real-time scanning environment. However, if only a time-delay and amplitude aberration correction filter is sought, appropriate model-based averaging of the cross-spectrum over a wider frequency band will yield a similar effect to acquiring independent realisations. In this situation the number of independent realisations may, therefore, be greatly reduced. An important issue for implementation will be to determine the number of receive-signals necessary to obtain an adequate estimate.

The transmit-focus of an ultrasound beam may be quantified by measuring the width of the transmit-beam profile. The beam profiles shown in Fig. 7.2 display a significant improvement in focus quality as a result of the iterative transmit-beam correction process. Furthermore, the convergence towards an almost-ideal beam profile width is rapid. There is, however, a slight offset of the peak for the beam profiles.

This shift, particularly noticeable for the s6 aberrator, is produced by a refraction of the transmitted beam. In this two-way imaging system, where reciprocity implies that the back-scattered beam will experience the same refraction as the transmitted beam, the associated shift of the beam profile is not observed from the transducer array. How to deal with refraction of the beam due to aberration through the body wall remains an issue for further research.

For the w6 aberrator, both estimation methods yield transmit-beams with the same degree of focus after two transmit-beam iterations as those obtained using the point source reference for aberration correction. Beyond two iterations, no significant improvement of the beam profiles is achieved. In the case of the s6 aberrator, three iterations are required for the MBFO estimate to achieve as good a correction as the point source reference. Beyond this point, no significant improvement can be found in the transmit-beam profiles. The EFE estimate does not improve the beam profile significantly after the second iteration.

Convergence for the beam profiles is accompanied by an apparent convergence also for the time-delays and amplitudes shown in Figs. 7.3 and 7.4. After approximately two iterations, no essential change occurs in the phase estimates for either method. Amplitude estimates are improved with further iteration for the MBFO algorithm, but for the EFE estimate more than two iterations are not required.

In the weakly aberrated case, the time-delays obtained using both estimation methods are very close to the point source reference. For the s6 aberrator, the estimated arrival times exhibit discontinuities, while the point source reference does not. The discontinuities are linked to waveform deformation in the received signals for the s6 aberrator. [15]

Waveform deformation results in low signal amplitudes, and causes discontinuities in the arrival times between adjacent element signals. [4,5]

The MBFO algorithm produces amplitude estimates which are close to the point source reference both for the w6 and s6 aberrators. For the s6 aberrator the corrected

beam profile is improved significantly for the third iteration using MBFO, even if the time-delay estimate does not change much from the second to the third. This improvement must therefore be the result of the improved amplitude estimate.

This observation is in accordance with the predicted amplitude error as a result of omitting the phase of F_{pn} in Eq. (7.11). Transmitting with a correct phase filter will, according to Eq. (7.4), produce an F_{pn} which is real. The amplitude error will, therefore, not be introduced in the MBFO estimate based on the corrected backscatter, resulting in a good amplitude estimate.

Due to the discontinuities of the arrival time estimates, and the apodisation of the EFE amplitude relative to the screen, the L^2 distance remains large also after iteration (see Fig. 7.5). Therefore, the L^2 distance does not adequately reflect the aberration correction capabilities of the associated correction filter.

Rigby *et al.*[9] obtained convergence after three or four iterations, but the convergence quality of the estimates is not certain as no reference could be provided for the subjects used in the study.

The number of independent signals used for estimating covariance or cross-spectra will influence the accuracy with which arrival times and amplitudes are estimated. This will affect the convergence rate. In Ref. 5 it was shown that introducing amplitude correction in addition to time-delay correction was of vital importance for the side-lobe level of the beam profiles. Proper amplitude correction will thus increase the spatial coherence in the received signal, and reduce the number of iterations required for the aberration correction algorithm to converge. Both of the aforementioned issues could be the catalyst for the overall improved convergence rates in this work compared to the results obtained in Ref. 9.

Based on the van Cittert-Zernike theorem, the width of the coherence function for the receive signal may be used to determine the width of the associated focus. Figure 7.6 clearly shows an increasing overall width of the coherence functions as a result of iteration for both aberrators and both estimation methods. The visual impression is that performing two iterations is sufficient to obtain almost maximum coherence widths. Beyond this, only minor improvements occur. Thus the coherence functions do give the correct impression of the converging beam profiles for the iteration process. However, the difficulty herein is determining at which level the width of the coherence function should be measured. As seen in Fig. 7.7, the choice impacts on the width curves dramatically. This renders the coherence width less attractive for determining the point of convergence.

The parameter C was originally introduced as a measure to quantify the degree of focusing for a given transmit-beam based on the backscatter signal. When applied to the iterative transmit-beam correction procedure, the value for C is observed to increase initially, and then level off at the point beyond which no practical improvement of the beam profile is achieved. (See Figs. 7.2, 7.8 and 7.9.) The point of convergence can therefore be found by identifying the point where this curve levels

off. Furthermore, the theoretical upper bound for this parameter may be used as an indication of how close the corrected beam profile is to an ideal transmit-beam profile. The iteration may therefore be set to terminate when a given threshold for C has been reached.

Based on the beam profiles presented for the w6 and s6 aberrator, it is clear, from the focus quality parameter, that the beam profiles for the rest of the aberrators were very well corrected. This was confirmed by visual inspection of the profiles. Furthermore, the results indicate that for $C > 0.4$, aberration correction of the transmit beam is close to the correction obtained with the point source reference for these aberrators.

An added advantage of using the parameter C to determine convergence, is the relatively low computational complexity involved. This, combined with the fact that it is computed from information readily available in the backscatter signal, without requiring knowledge of a point source/scatterer, may therefore enable the parameter C to be implemented in an aberration correction procedure without much additional effort.

For the s8 wall, the MBFO algorithm requires five iterations for proper convergence. For this aberrator, the uncorrected beam profile had very high side-lobe levels, where one side lobe was higher than the main lobe. This caused the MBFO algorithm, initially, to focus on this side lobe. Through transmit-beam iteration, the beam profile was improved and a linear slope was detected at iteration 3. Removing the linear component of the arrival time estimate then focused the beam correctly (observed from the point source simulations). For the EFE, this effect is avoided by choosing the eigenvector associated with the second largest eigenvalue because this had a smaller linear component in the phase. [16]

In the presented results the acoustic scatterers are δ-correlated. This ensures that the acoustic backscatter is a Gaussian stochastic process, at least asymptotically, and is a natural assumption in many imaging situations. Furthermore, the scattering intensity was the same everywhere. This is a good approximation when imaging homogeneous organs such as liver and spleen. The derivation of the MBFO shows that a spatially-variable scattering intensity will affect the estimate in the form of a different cross-spectrum for the unaberrated backscatter, F_{pn}. In this situation an estimate for F_{pn} may not be obtained using the van Cittert-Zernike theorem unless the scattering intensity is known. An alternative approach would be to utilise the fact that, according to the signal model, the magnitude of the coherence is proportional to $|F_{pn}|$. The EFE will focus the corrected beam also in the situation with spatially-variable scattering intensity. However, the focus will be determined by a product of the scattering intensity and the intensity of the transmit-beam, and not the transmit-beam alone. A combination of selecting the eigenvector with lowest linear component and removing the remaining linear slope will focus the aberration-corrected transmit-beam at the right location. An aberration correction filter may

therefore be obtained by either estimation method, also in the case of variable scattering intensity. As a consequence of iterative transmit-beam correction the focal zone will narrow. The assumption of a constant scattering intensity will thus become increasingly well-founded.

In this article, theory and simulations have been presented for ultrasound propagation in a non-absorbing medium. If the medium exhibits absorption which is homogeneous, *i.e.*, the absorption is the same everywhere in the medium, it can still be shown that a match filter is ideal for aberration correction.[17] (Ch. 11). In the presence of heterogeneous absorption, however, the aberration contributed by the absorption should be corrected using an inverse filter.[25,26] In a practical situation, where both heterogeneous absorption and heterogeneous speed of sound are contributing factors, a combination of an inverse filter and a match filter, *e.g.* a Wiener filter, would probably result in best overall performance.

The results presented here were obtained by simulating sound propagation in 2D. This represents a simplification in that out-of-plane aberration/scattering effects are not included. However, combined experimental and simulation studies of wavefront aberration through the abdominal wall have concluded that important aspects of wavefront aberration are also observed in 2D models.[27] Although details may vary, the qualitative aspects of the results are expected to hold, also in a real-world situation.

Although 2D simulations are assumed to give an accurate picture of the aberration correction process, in order to perform aberration correction in a real-world setting certain issues such as element size and directivity must be taken into account.

The array elements must be smaller than the correlation length of the aberration. In the azimuth direction this requirement will generally be much weaker than standard beam-forming requirements. However, the same requirement must also hold in the elevation direction. In practise, this means that either 1.75D or 2D arrays are needed.

For large apertures, element directivity could reduce the signal-to-(electronic)-noise ratio (SNR) along the edges of the array.[14] This will, in turn, lead to a reduced spatial coherence in the measured signal, and thus a less accurate estimate of the correction filter. Since the correlation length of the aberration generally is much larger than the standard beam-forming requirement, element signals may be combined in sub-apertures prior to aberration correction, thereby increasing the SNR. It is also noted that standard apodisation will reduce the contribution from the elements along the edges of the array. The reduced accuracy of the filter estimate will therefore only have a limited impact.

Noise was not introduced to the signals used in this study. Both algorithms used here average an aberration corrected signal over a sub-aperture, or the entire aperture, to create a stable reference for the correlation process. Since electronic noise is uncorrelated between elements, averaging over a sub-aperture will reduce

the noise level in the reference signal.[12] Furthermore, the SNR in standard ultrasound imaging is generally high. Walker and Trahey[28,29] showed that an SNR greater than 15 dB had little effect on the error of correlation-based phase estimates.

The effect of acoustic reverberation noise also represents a challenge, mainly because it is highly correlated both in the temporal and spatial directions. It is beyond the scope of this article to study reverberation noise.

VII Conclusion

Iteration of transmit-beam aberration correction with a time-delay and amplitude filter has been investigated. Two correlation-based algorithms for estimating arrival-time and amplitude fluctuations from random scatterers were employed. The resulting estimates were used to construct a time-delay and amplitude filter for aberration correction.

Results from simulations using eight aberrators, emulating the human abdominal wall, indicate overall convergence for both estimation methods after 1-3 iterations. Corrected beam profiles obtained after convergence were close to the unaberrated profiles. Transmit-beam iteration thus produced substantial improvements for all investigated aberrators.

In order to quantify the convergence, the focusing criterion C developed by Mallart and Fink,[11] and the width of the average coherence function[14] were calculated for the acoustic backscatter at each iteration.

Both the focusing criterion C and the coherence functions gave the correct impression of convergence for the transmit-beam profiles. However, there is an inherent problem of selecting an appropriate level at which to measure the width of the coherence function.

The focusing criterion C, on the other hand, is not associated with such difficulties. It is shown to determine accurately when convergence of the aberration correction procedure is achieved. The theoretical upper bound for C may be used as a criterion for termination of the transmit-beam iteration process. It is, therefore, the most attractive criterion for studying transmit-beam iteration. Furthermore, as it is inexpensive to compute, C may readily be implemented in an aberration correction scheme without much additional overhead.

Acknowledgments

This work was, in part, supported by the Medicine and Health program of the Research Council of Norway, and partly by the Norwegian University of Science and Technology (NTNU). Professor Harald Krogstad and Dr. Tonni Johansen at NTNU are thanked for useful discussions and comments. The reviewers are thanked for constructive comments that improved this article.

References

[1] S. W. Flax and M. O'Donnell, "Phase-aberration correction using signals from point reflectors and diffuce scatterers: Basic prinsiples," *IEEE Trans. Ultrason. Ferroelectr. Freq. Control*, vol. 35, no. 6, pp. 758–767, 1988.

[2] M. O'Donnell and S. W. Flax, "Phase-aberration correction using signals from point reflectors and diffuce scatterers: Measurements," *IEEE Trans. Ultrason. Ferroelectr. Freq. Control*, vol. 35, no. 6, pp. 768–774, 1988.

[3] L. Hinkelman, T. D. Mast, L. Metlay, and R. C. Waag, "The effect of abdominal wall morphology on ultrasonic pulse distortion. part I. measurements," *J. Acoust. Soc. Am.*, vol. 104, no. 6, pp. 3635–3649, December 1998.

[4] T. D. Mast, L. Hinkelman, M. Orr, and R. C. Waag, "The effect of abdominal wall morphology on ultrasonic pulse distortion. part II. simulations," *J. Acoust. Soc. Am.*, vol. 104, no. 6, pp. 3651–3664, December 1998.

[5] S. E. Måsøy, T. F. Johansen, and B. Angelsen, "Correction of ultrasonic wave aberration with a time delay and amplitude filter," *J. Acoust. Soc. Am.*, vol. 113, no. 4, pp. 2009–2020, April 2003.

[6] M. Karaman, A. Atalar, H. Köymen, and M. O'Donnell, "A phase aberration correction method for ultrasound imaging," *IEEE Trans. Ultrason. Ferroelectr. Freq. Control*, vol. 40, no. 4, pp. 275–282, 1993.

[7] S. Krishnan, K. W. Rigby, and M. O'Donnell, "Improved estimation of phase aberration profiles," *IEEE Trans. Ultrason. Ferroelectr. Freq. Control*, vol. 44, no. 3, pp. 701–713, 1997.

[8] ——, "Efficient parallel adaptive aberration correction," *IEEE Trans. Ultrason. Ferroelectr. Freq. Control*, vol. 45, no. 3, pp. 691–703, 1998.

[9] K. W. Rigby, C. L. Chalek, B. H. Haider, R. S. Lewandowski, M. O'Donnell, L. S. Smith, and D. G. Wildes, "Improved in vivo abdominal image quality using real-time estimation and correction of wavefront arrival time errors," in *Proc. 2000 IEEE-UFFC Ultrasonics Symposium*, vol. II, NY, 2000, pp. 1645–1653, IEEE Cat. No. 00CH37121.

[10] D.-L. Liu and R. C. Waag, "Correction of ultrasound wavefront distortion using backpropagation and a reference waveform method for time-shift compensation," *J. Acoust. Soc. Am.*, vol. 96, no. 2, pp. 649–660, August 1994.

[11] R. Mallart and M. Fink, "Adaptive focusing in scattering media through sound-speed inhomogeneities: The van Cittert Zernike approach and focusing criterion," *J. Acoust. Soc. Am.*, vol. 96, no. 6, pp. 3721–3732, 1994.

[12] G. C. Ng, S. S. Worrell, P. D. Freiburger, and G. E. Trahey, "A comparative evaluation of several algorithms for phase aberration correction," *IEEE Trans. Ultrason. Ferroelectr. Freq. Control*, vol. 41, no. 5, pp. 631–643, 1994.

[13] A. P. Berkhoff and J. M. Thijssen, "Correction of concentrated and distributed aberrations in medical ultrasound imaging," in *Proc. 1996 IEEE-UFFC Ultrasonics Symposium*, 1996, pp. 1405–1410.

[14] J. C. Lacefield and R. C. Waag, "Spatial coherence analysis applied to aberration correction using a two-dimensional array system," *J. Acoust. Soc. Am.*, vol. 112, no. 6, pp. 2558–2566, December 2002.

[15] S.-E. Måsøy, T. Varslot, and B. Angelsen, "Estimation of ultrasonic wave aberration with signals from random scatterers," *J. Acoust. Soc. Am.*, vol. 115, no. 6, pp. 2998–3009, June 2004.

[16] T. Varslot, E. Mo, H. Krogstad, and B. Angelsen, "Eigenfunction analysis of stochastic backscatter for characterization of acoustic aberration in medical ultrasound imaging," *J. Acoust. Soc. Am.*, vol. 115, no. 6, pp. 3068–3076, June 2004.

[17] B. A. Angelsen, *Ultrasound imaging. Waves, signals and signal processing*. Trondheim, Norway: Emantec, 2000, vol. 2, http://www.ultrasoundbook.com.

[18] R. Mallart and M. Fink, "The van Cittert-Zernike theorem in pulse echo measurements," *J. Acoust. Soc. Am.*, vol. 90, no. 5, pp. 2718–2727, November 1991.

[19] T. Varslot, B. A. Angelsen, and R. C. Waag, "Spectral estimation for characterization of acoustic aberration," *J. Acoust. Soc. Am.*, vol. 116, no. 1, pp. 97–108, July 2004.

[20] M. B. Priestley, *Spectral Analysis and Time Series*. London: Academic Press, 1981.

[21] T. K. Moon and W. C. Stirling, *Mathematical Methods and Algorithms for Signal Processing*. Englewood Cliffs, New Jersey: Prentice Hall, 2000.

[22] L. F. Nock, G. E. Trahey, and S. W. Smith, "Phase aberration correction in medical ultrasound using speckle brightness as an image quality factor," *J. Acoust. Soc. Am.*, vol. 85, no. 5, pp. 1819–1833, May 1989.

[23] L. Hinkelman, D.-L. Liu, L. A. Metlay, and R. C. Waag, "Measurements of ultrasonic pulse arrival time and energy level variations produced by propagation through abdominal wall," *J. Acoust. Soc. Am.*, vol. 95, no. 1, pp. 530–541, January 1994.

[24] S. D. Silverstein and D. P. Ceperley, "Autofocusing in medical ultrasound: The scaled covariance matrix algorithm," *IEEE Trans. Ultrason. Ferroelectr. Freq. Control*, vol. 50, no. 7, pp. 795–804, July 2003.

[25] Q. Zhu and B. D. Steinberg, "Deaberration of incoherent wavefront distortion: An approach toward inverse filtering," *IEEE Trans. Ultrason. Ferroelectr. Freq. Control*, vol. 44, no. 3, pp. 575–589, May 1997.

[26] M. Tanter, J.-L. Thomas, and M. Fink, "Time reversal and the inverse filter," *J. Acoust. Soc. Am.*, vol. 108, no. 1, pp. 223–234, July 2000.

[27] T. D. Mast, L. Hinkelman, M. O, V. Sparrow, and R. C. Waag, "Simulation of ultrasonic pulse propagation through the abdominal wall," *J. Acoust. Soc. Am.*, vol. 102, no. 2, pp. 1177–1190, August 1997.

[28] W. F. Walker and G. E. Trahey, "A fundamental limit on the performance of correlation based phase correction and flow estimation techniques," *IEEE Trans. Ultrason. Ferroelectr. Freq. Control*, vol. 41, no. 5, pp. 644–654, September 1994.

[29] ——, "A fundamental limit on delay estimation using partially correlated speckle signals," *IEEE Trans. Ultrason. Ferroelectr. Freq. Control*, vol. 42, no. 2, pp. 301–308, March 1995.

Appendix A

Global maximum of a likelihood function

T. Varslot
Dept. Mathematical Sciences, NTNU

Let A be a positive semi-definite matrix. Define the function $g : \mathbb{C}^N \to \mathbb{R}$ as

$$g(z) = \sum_{k=1}^{N} \ln |z_k|^2 - z^{\mathrm{H}} A z. \tag{A.1}$$

This function is well-defined on the open subset of $\mathbb{C}^N$ consisting of vectors $z = (z_1 \dots z_N)^{\mathrm{T}}$ such that $z_k \neq 0$ for all k.

The aim is to locate a global maximum of the nonlinear function g.

Lemma 1 *The matrix A must be positive definite for a global maximum of g to exist.*

The existence of a maximum of g is evident if A is positive definite because

$$\lim_{\|z\|^2 \to \infty} g(z) = -\infty,$$
$$\lim_{|z_k| \to 0} g(z) = -\infty.$$

If A is only semi-definite, an arbitrarily large value for g may be obtained by selecting z from the non-trivial null-space of A. In this case a global maximum does not exist.

Remark 1 *It is easy to see that for a fixed z and for any real number θ*

$$g(z) = g(z e^{i\theta}).$$

The maximum solution is therefore not unique.

Lemma 2 *A necessary condition for z to be a global maximum of g is that*

$$\begin{pmatrix} 1/\overline{z}_1 \\ \vdots \\ 1/\overline{z}_N \end{pmatrix} = A \begin{pmatrix} z_1 \\ \vdots \\ z_N \end{pmatrix}. \tag{A.2}$$

Assume that A is positive definite such that the global maximum exists. Because g is continuous and differentiable inside its domain of definition, all critical points of g are characterised by the fact that the the derivative of g equals zero. This is achieved when

$$g(z+\delta) - g(z) = O(\delta_k^2)$$

for all complex vectors δ with δ_k small enough. Straightforward calculations to first order in δ_k show that

$$\begin{aligned} g(z+\delta) - g(z) &= \sum_{k=1}^{N} \ln|z_k+\delta_k|^2 - (z+\delta)^H A(z+\delta) \\ &\quad - \sum_{k=1}^{N} \ln|z_k|^2 + z^H A z \\ &= 2\mathrm{Re}\left[\sum_{k=1}^{N} \frac{\delta_k}{z_k}\right] - 2\mathrm{Re}\left[z^H A\delta\right] + O(\delta_k^2). \end{aligned}$$

Therefore, a necessary condition for maximum is that

$$\frac{1}{z_k} = \left(z^{\mathrm{H}} A\right)_k,$$

or equivalently

$$\frac{1}{\overline{z}_k} = \sum_{n=1}^{N} A_{kn} z_n.$$

The critical points of g are thus found as solutions to

$$\begin{pmatrix} 1/\overline{z}_1 \\ \vdots \\ 1/\overline{z}_N \end{pmatrix} = A \begin{pmatrix} z_1 \\ \vdots \\ z_N \end{pmatrix}.$$

For $N = 2$ the problem is now easily solved. Letting $z_k = r_k \exp(i\theta_k)$, Eq. (A.2) may be rewritten

$$\begin{aligned} a_{11} r_1^2 + a_{12} r_1 r_2 e^{i(\theta_2-\theta_1)} &= 1 \\ \overline{a_{12}} r_1 r_2 e^{-i(\theta_2-\theta_1)} + a_{22} r_2^2 &= 1. \end{aligned}$$

Therefore

$$r_1 = \sqrt{\frac{a_{22}}{a_{11}}}\sqrt{\frac{\sqrt{a}_{11}}{a_{22}\sqrt{a}_{11}+|a_{12}|\sqrt{a}_{22}}}$$
$$r_2 = \sqrt{\frac{\sqrt{a}_{11}}{a_{22}\sqrt{a}_{11}+|a_{12}|\sqrt{a}_{22}}}$$
$$\theta_2 = \theta_1 - \arg\left[a_{12}\right],$$

where $\arg[a_{12}]$ is the phase of a_{12}. This solution characterises all critical points of g using θ_1 as a free variable. Since the value of g is the same at all of these points, a global maximum of g has been found.

Remark 2 *If $a_{12} = 0$ then $\arg[a_{12}]$ is not well-defined. In this situation there is no connection between θ_1 and θ_2. This may readily be verified by the fact that neither θ_1 nor θ_2 enters the equation.*

Lemma 3 *The critical points of g lie on the quadratic form*

$$z^{\mathrm{H}}Az = N. \tag{A.3}$$

For a general N, multiplying Eq. (A.2) from the right by z^{H} yields

$$\left(\overline{z}_1 \dots \overline{z}_N\right)\begin{pmatrix} 1/\overline{z}_1 \\ \vdots \\ 1/\overline{z}_N \end{pmatrix} = \left(\overline{z}_1 \dots \overline{z}_N\right) A \begin{pmatrix} z_1 \\ \vdots \\ z_N \end{pmatrix}.$$

Furthermore, for any vector z where $z_k \neq 0$

$$\left(\overline{z}_1 \dots \overline{z}_N\right)\begin{pmatrix} 1/\overline{z}_1 \\ \vdots \\ 1/\overline{z}_N \end{pmatrix} = N.$$

Thus Eq. (A.2) implies Eq. (A.3).

Lemma 4 *Let $\lambda_1 \dots \lambda_N$ be the eigenvalues of A, ordered according to decreasing magnitude. A necessary requirement for z to be a global maximum of g is that*

$$\sqrt{\frac{N}{\lambda_1}} \leq \|z\|_2 \leq \sqrt{\frac{N}{\lambda_N}}. \tag{A.4}$$

Let z be a solution of Eq. (A.3) and define λ as $\lambda = N/\|z\|_2^2$. Inserting this into Eq. (A.3) results in

$$z^{\mathrm{H}} A z = \lambda z^{\mathrm{H}} z,$$

or equivalently

$$z^{\mathrm{H}} (A - \lambda I)\, z = 0.$$

Let $\lambda_1 \ldots \lambda_N$ be eigenvalues of A, ordered according to decreasing magnitude, with associated orthonormal eigenvectors $u_{(1)} \ldots u_{(N)}$. Since A is Hermitian, any vector z may be expressed as

$$z = \sum_k c_k u_{(k)},$$

where $c_1 \ldots c_N$ are coefficients. Therefore

$$\begin{aligned} 0 &= \left(\sum_k \overline{c}_k u_k^{\mathrm{H}} \right) (A - \lambda I) \left(\sum_k c_k u_k \right) \\ &= \sum_k |c_k|^2 (\lambda_k - \lambda)\,. \end{aligned}$$

Since all eigenvalues are assumed to be positive, this is only possible if $\lambda_N \le \lambda \le \lambda_1$. Thus

$$\sqrt{\frac{N}{\lambda_1}} \le \|z\|_2 \le \sqrt{\frac{N}{\lambda_N}}.$$

Lemma 5 *Maximising g is equivalent to maximising*

$$f(z) = \sum_{k=1}^{N} \ln |z_k|^2 \tag{A.5}$$

subject to the constraint

$$z^{\mathrm{H}} A z = N.$$

This is just a rephrasing of Lemma 3.

Lemma 6 *The surface $z^{\mathrm{H}} A z = N$ is an ellipsoid in $\mathbb{R}^{2N}$.*

Any Hermitian matrix A may be decomposed in a real symmetric matrix A_r and a real skew-symmetric matrix B such that $A = A_r + iB$. Furthermore, let $z = x + iy$, where x

and y are real vectors. Then

$$\begin{aligned} N &= z^{\mathrm{T}} A z \\ &= x^{\mathrm{T}} A_r x + y^{\mathrm{T}} A_r y - x^{\mathrm{T}} B y + y^{\mathrm{T}} B x \\ &= (x^{\mathrm{T}} y^{\mathrm{T}}) \begin{pmatrix} A_r & -B \\ B & A_r \end{pmatrix} \begin{pmatrix} x \\ y \end{pmatrix}. \end{aligned}$$

Since the original matrix A was Hermitian and positive definite, the new matrix

$$\begin{pmatrix} A_r & -B \\ B & A_r \end{pmatrix}$$

is real, symmetric and positive definite. It is therefore a proper ellipsoid in $\mathbb{R}^{2N}$.

The contours for $f(x, y)$ as a function in $\mathbb{R}^{2N}$ are found as

$$f(x, y) = \sum_{k=1}^{N} \ln\left(x_k^2 + y_k^2\right) = C_0,$$

or equivalently

$$\prod_{k=1}^{N} \left(x_k^2 + y_k^2\right) = C.$$

In the $x_k y_k$-plane this corresponds to circles, when all other variables are held constant. In the $x_k x_n$-plane these are hyperbolas when $y_k = 0$ and $y_n = 0$, and something resembling a four-armed starfish otherwise. Figures A.1 and A.2 show the contours for the two situations, and Fig. A.3 shows a contour surface.

The value of $f(x, y)$ increases outwards with increasing $(x_k^2 + y_k^2)$. Figure A.4 depicts the situation for $N = 2$. It is seen that the maximum value of f on the four-dimensional ellipsoid is obtained at some point $(\sqrt{x_1^2 + y_1^2}, \sqrt{x_2^2 + y_2^2})$. The intersection of two 3D surfaces in a 4D space is potentially a 2D manifold. However, as long as the principal axes of the ellipsoid are not aligned with the coordinate axes, the ellipsoid does not possess the same rotational symmetries as the level curves. The intersection manifold, therefore, collapses to 1D; the global maximum of $f(z)$ is obtained along the path $(z_1, z_2)e^{i\theta}$ for any θ. This path is always a common symmetry of the level curves of f and the ellipsoid.

Although no proof has been found, this intuition seems to hold also for higher dimensions.

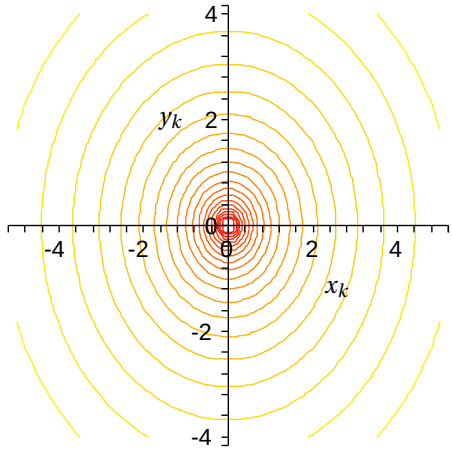

Figure A.1: Level curves of $f(x, y)$ in the $x_k y_k$-plane.

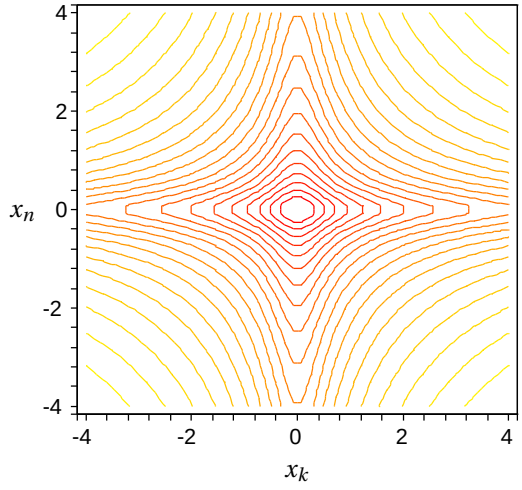

Figure A.2: Level curves of $f(x, y)$ in the $x_k x_n$-plane ($k \neq n$).

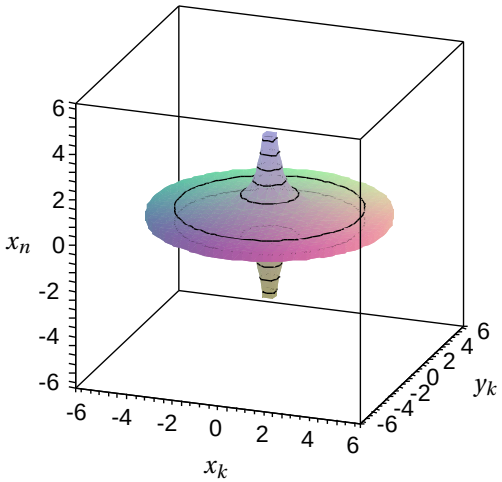

Figure A.3: Level curves of $f(x,y)$ in the subspace $x_k y_k x_n$ $(k \neq n)$.

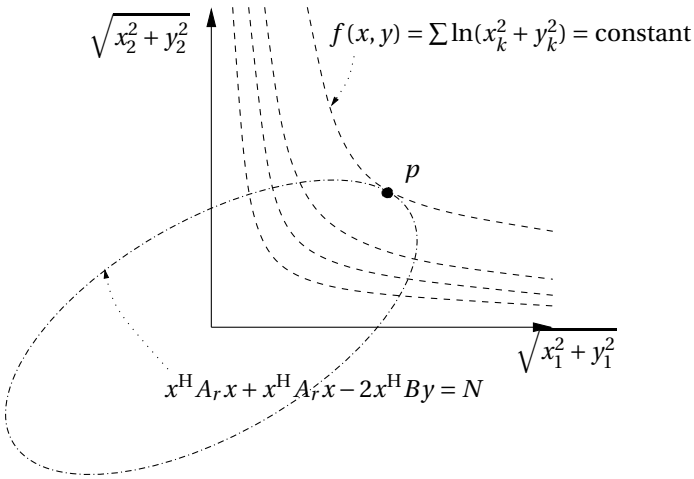

Figure A.4: A 2D cross-section of the level curves of $f(x,y)$ and the ellipsoid $(x+iy)^H A(x+iy) = N$ for $N = 2$. The point of intersection, indicated by p, may potentially be a 2D surface, but degenerates to a 1D path when the coordinate axes are not parallel to the principal axes of the ellipsoid.

Bibliography

This is a list of all previous works cited in the thesis

M. E. Anderson, "A 2D nonlinear wave propagation solver written in open-source matlab code," in *Proc. 2000 IEEE-UFFC Ultrasonics Symposium*, 2000. [Online]. Available: http://www.seas.rochester.edu/~maanders/sps2d.html

B. A. Angelsen, *Ultrasound imaging. Waves, signals and signal processing.* Trondheim, Norway: Emantec, 2000, vol. 1, http://www.ultrasoundbook.com.

——, *Ultrasound imaging. Waves, signals and signal processing.* Trondheim, Norway: Emantec, 2000, vol. 2, http://www.ultrasoundbook.com.

A. Bamberg, B. Engqvist, L. Halpern, and P. Joly, "Higher order paraxial wave equation a approximations in heterogeneous media," *SIAM J. Appl. Math.*, vol. 48, no. 1, pp. 99–128, 1988.

——, "Parabolic wave equation approximations in heterogeneous media," *SIAM J. Appl. Math.*, vol. 48, no. 1, pp. 99–128, 1988.

E. Bécache, F. Collino, and P. Joly, "Higher-order numerical schemes and operator splitting for solving 3D paraxial wave equations in heterogeneous media," INRIA, Rapport de recherche 3497, 1998.

J.-P. Berenger, "A perfectly matched layer for the absorption of electromagnetic waves," *J. Comp. Phys.*, vol. 114, no. 2, pp. 185–200, 1994.

A. P. Berkhoff and J. M. Thijssen, "Correction of concentrated and distributed aberrations in medical ultrasound imaging," in *Proc. 1996 IEEE-UFFC Ultrasonics Symposium*, 1996, pp. 1405–1410.

A. Bouakaz, C. Lancée, and N. de Jong, "Harmonic ultrasonic field of medical phased arrays: Simulations and measurements," *IEEE Trans. Ultrason. Ferroelectr. Freq. Control*, vol. 50, no. 6, pp. 730–735, June 2003.

L. Brekhovskikh and O. Godin, *Acoustics of Layered Media I-II*, 2nd ed. Springer, 1999.

J. P. Burg, D. Luenberger, and D. L. Wenger, "Estimation of structured covarianve matrices," *IEEE Proc.*, vol. 70, no. 9, pp. 963–974, 1982.

G. Casella and R. Berger, *Statistical Inference*, 1st ed. California: Duxbury, 1990.

P. T. Christopher, "Finite amplitude distortion-based inhomogeneous pulse echo ultrasound imaging," *IEEE Trans. Ultrason. Ferroelectr. Freq. Control*, vol. 44, no. 1, pp. 125–139, January 1997.

P. T. Christopher and K. J. Parker, "New approaches to nonlinear diffractive fields propagation," *J. Acoust. Soc. Am.*, vol. 90, no. 1, pp. 488–499, July 1991.

J. F. Claerbout, *Fundamentals of Geophysical Data Processing*. New York: McGraw-Hill, 1976.

F. Collino, "Perfectly matched absorbing layers for the paraxial equations," *J. Comp. Phys.*, vol. 131, no. 1, pp. 164–180, 1997.

J. Dollard and C. Friedman, *Product Integration with Applications to Differential Equations*, ser. Encyclopædia of mathematics and its applications, G.-C. Rota, Ed. Reading, Massachusetts: Addison-Wesley, 1979.

D. Donskoy, A. Ekimov, N. Sedunov, and M. Tsionskiy, "Nonlinear seismo-acoustic land mine detection and discrimination," *J. Acoust. Soc. Am.*, vol. 111, no. 6, pp. 2705–2714, 2002.

R. E. Dorsey and W. J. Mayer, "Genetic algorithms for estimation problems with multiple optima, nondifferentiability, and irregular features," *J. Bus. Econ. Stat.*, vol. 13, pp. 53–66, 1995.

F. A. Duck, *Physical properties of tissue*. London: Academic Press, 1990.

J. Engelbrecht, *Nonlinear Wave Dynamics*. Dordrecht, The Netherlands: Kluwer Academic Press, 1997.

H. Engl, M. Hanke, and A. Neubauer, *Regularization of inverse problems*. Netherlands: Kluwer Academic Publishers, 2000.

M. Fink, "Time reversal of ultrasonic fields - part I: Basic prinsiples," *IEEE Trans. Ultrason. Ferroelectr. Freq. Control*, vol. 39, pp. 555–567, 1992.

S. W. Flax and M. O'Donnell, "Phase-aberration correction using signals from point reflectors and diffuce scatterers: Basic prinsiples," *IEEE Trans. Ultrason. Ferroelectr. Freq. Control*, vol. 35, no. 6, pp. 758–767, 1988.

J. M. Fortes, "A closed loop ml algorithm for phase aberrration correction in phased array imaging systems - part I: Algorithm synthesis and experimental results," *IEEE Trans. Ultrason. Ferroelectr. Freq. Control*, vol. 44, no. 2, pp. 259–270, 1997.

——, "A closed loop ml algorithm for phase aberrration correction in phased array imaging systems - part II: Performancs analysis," *IEEE Trans. Ultrason. Ferroelectr. Freq. Control*, vol. 44, no. 2, pp. 259–270, 1997.

P. D. Freiburger, D. Sullivan, B. H. LeBlanc, and G. E. Trahey, "Two-dimensional ultrasonic beam distortion in the breast: in-vivo measurements and effects," *Ultrason. Imaging*, vol. 14, pp. 398–414, 1992.

U. Haberkorn, G. Layer, V. Rudat, I. Zuna, A. Lorenz, and G. van Kaick, "Ultrasound image properties influenced by abdominal wall thickness and composition," *J. Clin. Ultrasound*, vol. 21, pp. 423–429, 1993.

S. L. Hagen-Ansert, *Textbook of Diagnostic Ultrasonography*, 5th ed. St. Louis: C. V. Mosby, 2000.

M. F. Hamilton and D. T. Blackstock, *Nonlinear Acoustics*. San Diego: Academic Press, 1997.

L. Hinkelman, D.-L. Liu, L. A. Metlay, and R. C. Waag, "Measurements of ultrasonic pulse arrival time and energy level variations produced by propagation through abdominal wall," *J. Acoust. Soc. Am.*, vol. 95, no. 1, pp. 530–541, January 1994.

L. Hinkelman, T. D. Mast, L. Metlay, and R. C. Waag, "The effect of abdominal wall morphology on ultrasonic pulse distortion. part I. measurements," *J. Acoust. Soc. Am.*, vol. 104, no. 6, pp. 3635–3649, December 1998.

C. W. Horton, "Dispersion relationships in sediments and sea water," *J. Acoust. Soc. Am.*, vol. 55, pp. 547–549, 1974.

D. H. Howry and W. R. Bliss, "Ultrasonic visualisation of soft tissue structures of the body," *J. Lab. Clin. Med.*, vol. 40, p. 579, 1952.

G. M. Jenkins and D. G. Watts, *Spectral Analysis and its applications*. San Francisco: Holden-Day, 1968.

I. Kappel, *Evolution equations and Approximations*. San Diego: Academic Press, 1997.

M. Karaman, A. Atalar, H. Köymen, and M. O'Donnell, "A phase aberration correction method for ultrasound imaging," *IEEE Trans. Ultrason. Ferroelectr. Freq. Control*, vol. 40, no. 4, pp. 275–282, 1993.

S. Kay and S. Marple, "Spectrum analysis - a modern perspective," *Proc. IEEE*, vol. 69, no. 11, pp. 1380–1419, January 1981.

E. Kreyszig, *Introductory Functional Analysis*. Wiley, 1989.

S. Krishnan, K. W. Rigby, and M. O'Donnell, "Improved estimation of phase aberration profiles," *IEEE Trans. Ultrason. Ferroelectr. Freq. Control*, vol. 44, no. 3, pp. 701–713, 1997.

——, "Efficient parallel adaptive aberration correction," *IEEE Trans. Ultrason. Ferroelectr. Freq. Control*, vol. 45, no. 3, pp. 691–703, 1998.

R. D. L. Krönig, "On the theory of dispersion of x-rays," *J. Opt. Soc. Am.*, vol. 12, pp. 547–557, 1926.

V. P. Kuznetsov, "Equations of nonlinear acoustics," *Sov. Phys. Acoust.*, vol. 16, pp. 467–470, 1971.

J. C. Lacefield, W. C. Pilkington, and R. C. Waag, "Distributed aberrators for emulation of ultrasonic pulse distortion by abdominal wall," *Acoust. Res. Lett. Online*, vol. 3, no. 2, pp. 47–52, 2002.

J. C. Lacefield and R. C. Waag, "Spatial coherence analysis applied to aberration correction using a two-dimensional array system," *J. Acoust. Soc. Am.*, vol. 112, no. 6, pp. 2558–2566, December 2002.

H. P. Le, "Progress and trends in ink-jet printing technology," *J. Imaging Sci. Tech.*, vol. 42, no. 1, 1998.

F. Lin and R. C. Waag, "Estimation and compensation of ultrasonic wavefront distortion using a blind system identification method," *IEEE Trans. Ultrason. Ferroelectr. Freq. Control*, vol. 49, no. 6, pp. 739–755, 2002.

D.-L. Liu and R. C. Waag, "Estimation and correction of ultrasonic wavefront distortion using pulse-echo data received in a two-dimensional aperture," *IEEE Trans. Ultrason. Ferroelectr. Freq. Control*, vol. 45, no. 2, pp. 473–489, 1988.

——, "Correction of ultrasound wavefront distortion using backpropagation and a reference waveform method for time-shift compensation," *J. Acoust. Soc. Am.*, vol. 96, no. 2, pp. 649–660, August 1994.

——, "Time-shift compensation of ultrasonic pulse focus degradation using least-mean-square-error estimates of arrival time," *J. Acoust. Soc. Am.*, vol. 95, no. 1, pp. 542–555, January 1994.

——, "Estimation and correction of ultrasonic wavefront distortion using pulse-echo data received in a two-dimensional aperture," *IEEE Trans. Ultrason. Ferroelectr. Freq. Control*, vol. 45, no. 2, pp. 473–490, 1998.

R. Mallart and M. Fink, "The van Cittert-Zernike theorem in pulse echo measurements," *J. Acoust. Soc. Am.*, vol. 90, no. 5, pp. 2718–2727, November 1991.

——, "Adaptive focusing in scattering media through sound-speed inhomogeneities: The van Cittert Zernike approach and focusing criterion," *J. Acoust. Soc. Am.*, vol. 96, no. 6, pp. 3721–3732, 1994.

S. E. Måsøy, T. F. Johansen, and B. Angelsen, "Correction of ultrasonic wave aberration with a time delay and amplitude filter," *J. Acoust. Soc. Am.*, vol. 113, no. 4, pp. 2009–2020, April 2003.

S.-E. Måsøy, T. Varslot, and B. Angelsen, "Estimation of ultrasonic wave aberration with signals from random scatterers," *J. Acoust. Soc. Am.*, vol. 115, no. 6, pp. 2998–3009, June 2004.

T. D. Mast, L. Hinkelman, M. O, V. Sparrow, and R. C. Waag, "Simulation of ultrasonic pulse propagation through the abdominal wall," *J. Acoust. Soc. Am.*, vol. 102, no. 2, pp. 1177–1190, August 1997.

T. D. Mast, L. Hinkelman, M. Orr, and R. C. Waag, "The effect of abdominal wall morphology on ultrasonic pulse distortion. part II. simulations," *J. Acoust. Soc. Am.*, vol. 104, no. 6, pp. 3651–3664, December 1998.

T. D. Mast, A. I. Nachman, and R. C. Waag, "Focusing and imaging using eigenfunctions of the scattering operator," *J. Acoust. Soc. Am.*, vol. 102, no. 2, pp. 715–725, August 1997.

T. D. Mast, L. Sourian, D.-L. Liu, M. Tabei, A. Nachman, and R. C. Waag, "A k-space method for large-scale models of wave propagation in tissue," *IEEE Trans. Ultrason. Ferroelectr. Freq. Control*, vol. 48, no. 2, pp. 341–354, March 2001.

R. McOwen, *Partial Differential Equations*. Englewood Cliffs, New Jersey: Prentice Hall, 1996.

M. Mitchell, *An Introduction to Genetic Algorithms*. Cambridge, Mass.: MIT Press, 1996.

T. K. Moon and W. C. Stirling, *Mathematical Methods and Algorithms for Signal Processing*. Englewood Cliffs, New Jersey: Prentice Hall, 2000.

A. I. Nachman, J. F. Smith, and R. C. Waag, "An equation for acoustic propagation in inhomogeneous media with relaxation losses," *J. Acoust. Soc. Am.*, vol. 88, pp. 1584–1595, 1990.

K. Naugolnykh and L. Ostorovsky, *Nonlinear Wave Processes in Acoustics*. New York: Cambridge University Press, 1998.

G. C. Ng, S. S. Worrell, P. D. Freiburger, and G. E. Trahey, "A comparative evaluation of several algorithms for phase aberration correction," *IEEE Trans. Ultrason. Ferroelectr. Freq. Control*, vol. 41, no. 5, pp. 631–643, 1994.

L. F. Nock, G. E. Trahey, and S. W. Smith, "Phase aberration correction in medical ultrasound using speckle brightness as an image quality factor," *J. Acoust. Soc. Am.*, vol. 85, no. 5, pp. 1819–1833, May 1989.

G. V. Norton and J. C. Norini, "Including dispersion and attenuation directly in the time domain for wave propagation in isotropic media," *J. Acoust. Soc. Am.*, vol. 113, no. 6, pp. 3024–3031, 2003.

M. O'Donnell and S. W. Flax, "Phase-aberration correction using signals from point reflectors and diffuce scatterers: Measurements," *IEEE Trans. Ultrason. Ferroelectr. Freq. Control*, vol. 35, no. 6, pp. 768–774, 1988.

C. Prada, J. L. Thomas, and M. Fink, "The iterative time reversal process: analysis of convergence," *J. Acoust. Soc. Am.*, vol. 97, no. 1, pp. 62–71, January 1995.

V. V. Prasolov, *Problems and Theorems in Linear Algebra*. USA: AMS, 1994.

M. B. Priestley, *Spectral Analysis and Time Series*. London: Academic Press, 1981.

K. W. Rigby, C. L. Chalek, B. H. Haider, R. S. Lewandowski, M. O'Donnell, L. S. Smith, and D. G. Wildes, "Improved in vivo abdominal image quality using real-time estimation and correction of wavefront arrival time errors," in *Proc. 2000 IEEE-UFFC Ultrasonics Symposium*, vol. II, NY, 2000, pp. 1645–1653, IEEE Cat. No. 00CH37121.

J. K. Schneider and S. M. Gojevic, "Ultrasonic imaging systems for personal identification," in *Proc. 2001 IEEE-UFFC Ultrasonics Symposium*, 2001, pp. 595–601.

L. A. Segel, *Mathematics Applied to Continuum Mechanics*. New York: Dover, 1987.

S. D. Silverstein and D. P. Ceperley, "Autofocusing in medical ultrasound: The scaled covariance matrix algorithm," *IEEE Trans. Ultrason. Ferroelectr. Freq. Control*, vol. 50, no. 7, pp. 795–804, July 2003.

J. S. Simonoff, *Smoothing Methods in Statistics*. New York: Springer, 1996.

D. L. Snyder, *Random Point Processes*. New York: Wiley, 1975.

P. Stoica and R. Moses, *Introduction to Spectral Analysis*. Englewood Cliffs, New Jersey: Prentice Hall, 1997.

G. Strang, "On the construction and comparison of difference schemes," *Numer. Anal.*, vol. 5, pp. 506–517, 1968.

——, *Linear Algebra and its Applications*, 3rd ed. USA: Saunders, 1988.

T. L. Szabo, "Time domain wave equations for lossy media obeying a frequency power law," *J. Acoust. Soc. Am.*, vol. 96, pp. 491–500, 1994.

M. Tabei, T. D. Mast, and R. C. Waag, "Simulation of ultrasonic focus aberration and correction through human tissue," *J. Acoust. Soc. Am.*, vol. 113, no. 2, pp. 1166–1176, February 2003.

M. Tanter, J.-L. Thomas, and M. Fink, "Time reversal and the inverse filter," *J. Acoust. Soc. Am.*, vol. 108, no. 1, pp. 223–234, July 2000.

F. Tappert, "The parabolic approximation method in wave propagation and underwater acoustics," in *Lectures in Physics*, J. B. Keller and J. S. Papadakis, Eds. New York: Springer, 1977, pp. 224–287.

G. Taraldsen, "Derivation of a generalized Westervelt equation for nonlinear medical ultrasound," *J. Acoust. Soc. Am.*, vol. 109, no. 4, pp. 1329–1333, April 2001.

G. E. Trahey, P. D. Freiburger, L. F. Nock, and D. C. Sullivan, "In-vivo measurements of ultrasonic beam distortion in the breast," *Ultrason. Imaging*, vol. 13, no. 1, pp. 71–90, 1991.

G. E. Trahey and S. W. Smith, "Properties of acoustical speckle patterns in the presence of phase aberration. part i: First order statistics," *Ultrason. Imaging*, vol. 6, pp. 12–28, 1988.

P. J. M. van Laarhoven and E. H. L. Aarts, *Simulated Annealing: Theory and Applications*. Dordrecht, The Netherlands: Kluwer Academic Publishers, 1987.

F. Viola and W. F. Walker, "A comparison of the performance of time-delay estimators in medical ultrasound," *IEEE Trans. Ultrason. Ferroelectr. Freq. Control*, vol. 50, no. 4, pp. 392–401, April 2003.

W. F. Walker and G. E. Trahey, "A fundamental limit on the performance of correlation based phase correction and flow estimation techniques," *IEEE Trans. Ultrason. Ferroelectr. Freq. Control*, vol. 41, no. 5, pp. 644–654, September 1994.

——, "A fundamental limit on delay estimation using partially correlated speckle signals," *IEEE Trans. Ultrason. Ferroelectr. Freq. Control*, vol. 42, no. 2, pp. 301–308, March 1995.

G. B. Whitham, *Linear and Nonlinear Waves*. Wiley, 1974.

G. Wojcik, J. Mould, F. Ayter, and L. Carcione, "A study of second harmonic generation by focused medical transducer pulses," in *Proc. 1998 IEEE-UFFC Ultrasonics Symposium*, 1998, pp. 1583–1588.

G. L. Wojcik, B. Fornberg, R. C. Waag, L. Carcione, J. Mould, L. Nikodym, and T. Driscoll, "Pseudospectral methods for large-scale bioacoustic models," in *Proc. 1997 IEEE-UFFC Ultrasonics Symposium*, 1997, pp. 1501–1506.

E. A. Zabotskaya and R. V. Khoklov, "Quasi-plane waves in the non-linear acoustics of confined beams," *Sov. Phys. Acoust.*, vol. 15, pp. 35–40, 1969.

D. Zhao and G. E. Trahey, "A statistical analysis of phase aberration correction using image quality factors in coherent imaging systems," *IEEE Trans. Med. Imaging*, vol. 11, no. 3, pp. 446–452, 1992.

Q. Zhu and B. D. Steinberg, "Wavefront amplitude distribution in the female breast," *J. Acoust. Soc. Am.*, vol. 96, no. 1, pp. 1–9, April 1994.

——, "Deaberration of incoherent wavefront distortion: An approach toward inverse filtering," *IEEE Trans. Ultrason. Ferroelectr. Freq. Control*, vol. 44, no. 3, pp. 575–589, May 1997.